TRIBO-ELECTROCHEMICAL CHARACTERIZATION OF TANTALUM DURING ELECTROCHEMICAL-MECHANICAL POLISHING (ECMP)

A Dissertation

by

FENG GAO

Submitted to the Office of Graduate Studies of
Texas A&M University
in partial fulfillment of the requirements for the degree of

DOCTOR OF PHILOSOPHY

December 2010

Major Subject: Mechanical Engineering

TRIBO-ELECTROCHEMICAL CHARACTERIZATION OF TANTALUM DURING ELECTROCHEMICAL-MECHANICAL POLISHING (ECMP)

A Dissertation

by

FENG GAO

Submitted to the Office of Graduate Studies of
Texas A&M University
in partial fulfillment of the requirements for the degree of

DOCTOR OF PHILOSOPHY

Approved by:

Chair of Committee,	Hong Liang
Committee Members,	Karl Hartwig
	Cris Schwartz
	Jun Zou
Head of Department,	Dennis O'Neal

December 2010

Major Subject: Mechanical Engineering

ABSTRACT

Tribo-electrochemical Characterization of Tantalum during Electrochemical-Mechanical Polishing (ECMP).

(December 2010)

Feng Gao, B.A.; M.S., Tsinghua University, China

Chair of Advisory Committee: Dr. Hong Liang

Electrochemical Mechanical Polishing (ECMP) has become increasingly important due to the continuous decrease of the device size in integrated circuit (IC) fabrication. Tantalum (Ta) is a promising material as a substitute for copper in ICs. This dissertation studies the tribology and electrochemistry of Ta ECMP.

The present research uses experimental combined analysis approaches. A specially designed experimental setup assembling a tribometer and a potentiostat was used to carry out Ta ECMP. The friction force and electrochemical reactions were measured simultaneously. Using this setup, we found the factors which affected the frictional behaviors of Ta during ECMP. The technique of single frequency electrochemical impedance spectroscopy (EIS) was employed to investigate the material removal mechanisms in Ta ECMP. The results presented the competing mechanisms of removal and formation of a surface oxide layer of Ta.

In order to further the investigation in a nanoscale, the atomic force microscope (AFM) was used to measure the material removal rate. The Preston equation for the Ta

ECMP was established. A new methodology was developed to study the oxidation state and process of Ta during ECMP. Through comparing the material removal rate measured by using the AFM and the calculated one via the Faraday's law, the distribution of the Ta suboxides and pentoxide, as well as the oxidation process, was revealed. The oxidation process was strongly dependent of the applied anodic potential, thickness of the oxide layer, mechanical forces, and surface orientation. A polymer environmental cell was designed and produced. Using this cell and AFM, it was found that the material removal in the nanometer scale was a function of the surface orientations. This research is beneficial for optimization of the Ta ECMP process.

This dissertation includes six chapters. After Introduction and Motivation and Objectives, the material, setup, and testing conditions are discussed in Chapter III. Chapter IV discusses the tribology and material removal mechanisms in Ta ECMP, while Chapter V the oxidation of Ta during ECMP, followed by Conclusions and Future Work.

DEDICATION

This dissertation is dedicated to Dr. Hong Liang and my family.

ACKNOWLEDGEMENTS

I would like to thank my committee chair, Dr. Hong Liang, for her constant support all along my academic career in Texas A&M University. This dissertation would not have been possible without her help and guidance. I would also like to thank my committee members, Dr. Karl Hartwig, Dr. Cris Schwartz, and Dr. Jun Zou, for their guidance and support throughout the course of this research.

Thanks also go to my friends and colleagues and the department faculty and staff for making my time at Texas A&M University a great experience. I specially thank Rodrigo Cooper for his assistance in machining parts for the experimental setups, David Huitink in processing AFM images, and Dr. Xinghang Zhang in micro indentation. I also want to extend my gratitude to the National Science Foundation, which provided the grants (0535578) for my research and to Texas Engineering Experiment Station for paying my tuition and stipend.

Finally, thanks to my mother and father for their encouragement and to my wife for her patience and love.

NOMENCLATURE

CMP	Chemical Mechanical Polishing/Planarization
ECMP	Electrochemical Mechanical Polishing/Planarization
Ta	Tantalum
IC	Integrated Circuit
AFM	Atomic Force Microscope
EIS	Electrochemical Impedance Spectroscopy
XRD	X-ray Diffraction
XPS	X-ray Photoelectron Spectroscopy
PVD	Physical Vapor Deposition
ILD	Interlayer Dielectric

TABLE OF CONTENTS

Page

ABSTRACT iii

DEDICATION v

ACKNOWLEDGEMENTS vi

NOMENCLATURE vii

LIST OF FIGURES xi

LIST OF TABLES xv

CHAPTER

I INTRODUCTION 1

1.1. Barrier Layer Material—Tantalum 1
1.2. Chemical Mechanical Polishing/Planarization (CMP) 4
1.3. Electrochemical Mechanical Polishing/Planarization (ECMP) 13

II MOTIVATION AND OBJECTIVES 21

2.1. Developing In Situ Observation Setups 21
2.2. Revealing Material Removal Mechanisms 22
2.3. Establishing the Preston Equation for Tantalum ECMP 22
2.4. Obtaining Knowledge of the Oxidation Process in Tantalum ECMP 22

III EXPERIMENTAL 23

3.1. Materials 23
3.1.1. Tantalum 23
3.1.2. Chemicals 27
3.2. Tantalum Sample Preparation 27
3.3. Experimental 29
3.3.1. ECMP Testing Apparatus 29
3.3.2. Nanoscale Experimental Configuration 31
3.4. Fundamentals of Electrochemistry 33

CHAPTER Page

3.5. Measurement Techniques ... 34
3.5.1. Potentiodynamic Scan ... 34
3.5.2. Potentiostatic Test ... 36
3.5.3. Potentiostatic Electrochemical Impedance Spectroscopy (EIS) ... 36
3.5.4. Single Frequency Electrochemical Impedance Spectroscopy (EIS) ... 38
3.5.5. Material Removal Rate Measurement ... 39
3.6. Testing Parameters and Procedures ... 44
3.6.1. Tribological Characterization of Tantalum ECMP ... 44
3.6.2. Material Removal Mechanisms in Tantalum ECMP ... 45
3.6.3. Preston Equation in Tantalum ECMP ... 47
3.6.4. Oxidation Kinetics of Single Crystalline Tantalum ... 48
3.6.5. Material Removal in Nano Scale ... 49

IV TRIBOLOGICAL CHARACTERIZATION AND MATERIAL REMOVAL MECHANISMS IN ECMP PROCESSES ... 51

4.1. Tribological Characterization of Tantalum ECMP ... 51
4.1.1. Effects of Mechanical Forces on Tantalum Corrosion Behaviors during ECMP ... 52
4.1.2. Effects of Mechanical Forces on Tantalum Oxidation ... 56
4.1.3. Frictional Behaviors during ECMP ... 61
4.2. Material Removal Mechanisms in Tantalum ECMP ... 67
4.2.1. Material Removal Mechanism ... 68
4.2.2. Quantification of Material Removal ... 70
4.2.3. Factors Affecting the Material Removal ... 74
4.3. Kinetics of the Material Removal ... 83
4.4. Summary ... 85

V IN SITU OXIDATION PROCESSES AND MECHANISMS ... 88

5.1. Preston Equation in Tantalum ECMP ... 89
5.2. Oxidation Kinetics of Polycrystalline Tantalum during ECMP ... 94
5.3. Oxidation Kinetics of Single Crystalline Tantalum during ECMP ... 111
5.4. Material Removal Mechanisms in Nano Meter Length Scale ... 117
5.5. Summary ... 132

VI CONCLUSIONS AND FUTURE WORK ... 135

6.1. Conclusions ... 135

Page

6.2. Future Work 137

REFERENCES 138

VITA 146

LIST OF FIGURES

Page

Figure 1. 1. The schematic of the IC fabrication processes 2

Figure 1. 2. The structure of a trench in ICs with copper layer, tantalum (barrier layer), and dielectric. 3

Figure 1. 3. The schematic of CMP process. 5

Figure 1. 4. The material removal mechanisms in CMP. 8

Figure 1. 5. The dishing and erosion after CMP. 13

Figure 1. 6. The model of removing dishing in copper ECMP. 15

Figure 3. 1. BCC structure of Ta 23

Figure 3. 2. The XRD spectra of single and poly crystalline Ta samples 24

Figure 3. 3. The Ta sample for ECMP experiments. 28

Figure 3. 4. The schematic of the experimental setup. 30

Figure 3. 5. The environmental cell on AFM. 32

Figure 3. 6. A typical potentiodynamic curve (Tafel curve). 35

Figure 3. 7. The Nyquist curve and its equivalent circuit. 37

Figure 3. 8. Micro indents on the sample surface. 40

Figure 3. 9. 2-D and 3-D images of an indent (55.35×55.35 μm). 41

Figure 3. 10. The calculation of the actual material removal in each polishing test. 43

Figure 4. 1. Tafel curves obtained under different conditions. 52

Figure 4. 2. Current and corrosion potential during potentiodynamic tests. 54

Page

Figure 4. 3. Nyquist curves for non-potential polishing and 2 N polishing at different speeds....57

Figure 4. 4. Results of impedance measurements. 58

Figure 4. 5. Equivalent circuit for Randles model and Warburg impedance....59

Figure 4. 6. Friction coefficients for different loads and rotating speeds 62

Figure 4. 7. Friction coefficients obtained with sweeping potential and without potential, 2 N, 30 rpm. 63

Figure 4. 8. Friction coefficient and corrosion current, 4 N, 30 rpm 63

Figure 4. 9. Impedance curve obtained at 60 rpm, 4 N, and 1 V. 68

Figure 4. 10. A typical friction coefficient curve obtained under the polishing conditions of 60 rpm, 4 N, 1 V....71

Figure 4. 11. The enlarged impedance curves and sinusoidal simulation curves with different loads at 60 rpm and 1 V. 75

Figure 4. 12. The enlarged impedance curves and sinusoidal simulation curves with different rotating speed under 4 N and 1 V. 76

Figure 4. 13. The enlarged impedance curves and sinusoidal simulation curves with different potentials when 4 N and 60 rpm were applied. 78

Figure 4. 14. The enlarged impedance curves and sinusoidal simulation curves with different concentrations of abrasive when 4 N, 60 rpm and 1 V were applied. 79

Figure 4. 15. The enlarged impedance curves and sinusoidal simulation curves of CMP and ECMP when 4 N and 60 rpm were applied. 80

Figure 4. 16. The relationship between the mechanical power and the impedance....82

Figure 4. 17. The kinetics of the material removal in Ta ECMP 85

Page

Figure 5. 1. The MRR measured by using AFM vs. PV numbers. The potential applied on the sample was 1 V vs. SCE. 90

Figure 5. 2. The MRR vs. potential. The load and speed are 2 N and 0.08 m/min respectively. 92

Figure 5. 3. The MRR under different potential and PV numbers. 94

Figure 5. 4. The anodic current vs. PV and potential at a constant potential (1 V) and a constant PV=0.16 Nm/s. 97

Figure 5. 5. The calculated MRRs by inserting the anodic current and different valences into the Faraday's law. 98

Figure 5. 6. The comparison of the calculated MRR and the measured MRR by using AFM 101

Figure 5. 7. The average valences at the constant potential and constant PV 104

Figure 5. 8. The oxidation and removal processes at the constant potential during Ta ECMP. 107

Figure 5. 9. The oxidation and removal processes at the constant PV during Ta ECMP. 109

Figure 5. 10. The actual MRRs measured by using AFM vs. orientations. The load and speed are 1 N and 0.06 m/s respectively. 112

Figure 5. 11. The average valences of the removed oxides on different samples. 113

Figure 5. 12. The model of the oxidation process of the single crystalline Ta at 0.6 V. 114

Figure 5. 13. AFM height images obtained in the dynamic experiments on different oriented Ta surfaces. 119

Figure 5. 14. The surface roughness of different oriented samples obtained in the dynamic experiments. 122

Figure 5. 15. The anodic current vs. time of the (111) oriented sample. 124

Page

Figure 5. 16. The surface roughness change of the samples with different orientations during the anodic oxidation. 125

Figure 5. 17. The AFM scan on the (110) sample after the oxidation 126

Figure 5. 18. The AFM scan on the (100) sample after the oxidation. 127

Figure 5. 19. The AFM scan on the (111) sample after the oxidation. 128

Figure 5. 20. The models of the material removal in nanometer scale. 130

LIST OF TABLES

Page

Table 1. 1. The Preston equations in different CMP processes. 11

Table 3. 1. Testing conditions 45

Table 3. 2. Polishing parameters for ECMP tests. 46

Table 3. 3. Testing parameters 48

Table 3. 4. Polishing conditions for single crystalline Ta samples. 49

Table 4. 1. Factors affecting the friction coefficient. 65

Table 4. 2. The mechanical power and work introduced by the friction force. 73

CHAPTER I

INTRODUCTION

In order to understand this research, this chapter introduces the background in semiconductor fabrication, barrier layer materials, chemical mechanical polishing/planarization (CMP), and electrochemical mechanical polishing/planarization (ECMP). In addition, the tribology, like friction and wear, and electrochemistry, such as reactions and oxidation of metals in CMP and ECMP will be reviewed.

1.1. Barrier Layer Material—Tantalum

Semiconductor devices built on silicon wafers become increasingly important in our daily life, from flash memory to aerospace. There are hundreds of fabrication processes to produce integrated circuits (ICs) on bare silicon wafers. Fig. 1.1 illustrates the major steps in IC frabrication. The process starts with cutting silicon wafers into slices from a single crystal ingot. Devices then are manufactured on polished silicon wafers. Then, the trenches are made following the steps, such as photoresist coating, photolithography, and etching. After stripping the photoresist, a metal like copper is deposited on the wafer to fill all trenches as the interconnection to devices, such as diodes, resistors, transistors and so on. Finally, the over deposited copper is removed by CMP, leaving interconnected circuits on the surface.

This dissertation follows the style of *Journal of the Electrochemical Society*.

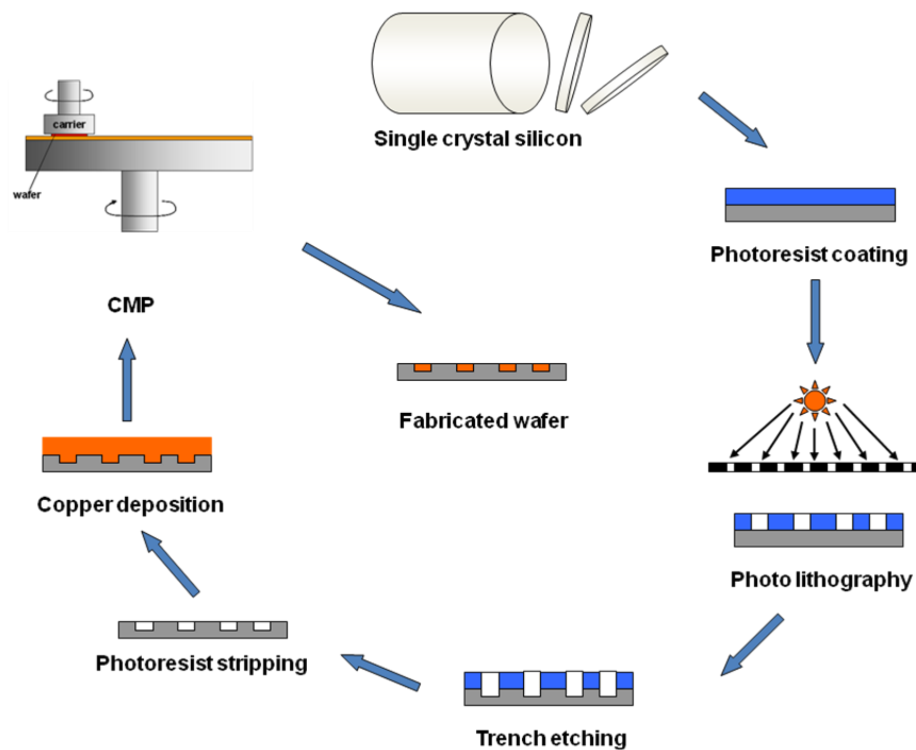

Figure 1. 1. The schematic of the IC fabrication processes.

In ICs, *RC* delay has been used to evaluate the performance of the circuits. Eq. 1.1 shows the definition of *RC* delay.

$$t = RC \tag{1.1}$$

where t is the time, representing the speed of the circuit; R is the total resistance of the interconnection; C is the capacitance of the circuit which is caused by the dielectric between devices. In order to improve the performance of ICs, i.e., shorten the *RC* delay, one way is to reduce the resistance of the interconnection. Hence, copper was used to replace aluminum as the interconnection some years ago due to its higher conductivity.[1] Copper was later found to diffuse readily into the surrounding dielectric and silicon.[2]

Copper did not adhere to the dielectric and other insulating materials well.[3] A barrier layer was introduced between copper and the dielectric to retard or prevent the copper diffusion and increase the adhesion of copper to the dielectric simultaneously. Fig. 1.2 shows the structure of a trench in ICs.

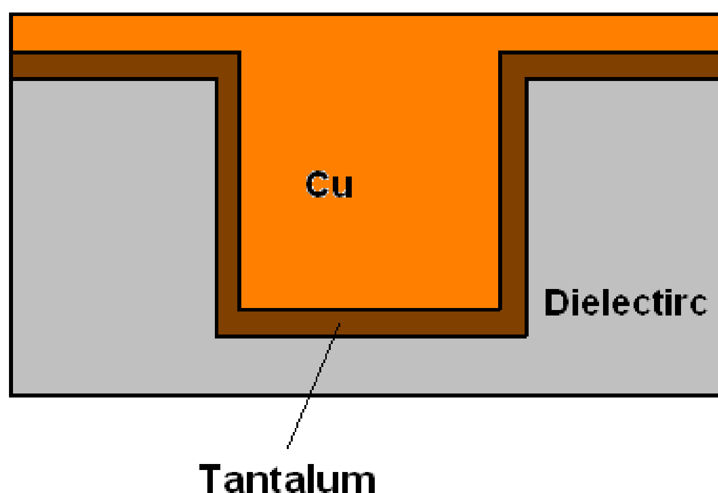

Figure 1. 2. The structure of a trench in ICs with copper layer, tantalum (barrier layer), and dielectric.

As a diffusion barrier material between copper and the dielectric, a low diffusivity is necessary. In addition, other requirements must be met, such as good adhesion to both copper and the dielectric, thermaldynamical and chemical stability, high electrical and thermal conductivity, and so on.[4] No material can meet all these requirements at once and a compromise is needed. It was found that tantalum (Ta) was one of the promising candidates as a barrier material.[5-6] Ta and copper did not form a solid solution according to the binary phase diagram.[7] Ta could prevent the copper

diffusion into silicon substrate at 450 ℃ for 5 hours.[8] Better performance of diffusion prevention could be achieved by using Ta rather than niobium, titanium, chromium and molybdenum.[9] Although Ta was not as good as tungsten in the diffusion retard[9], the adhesion of tungsten to the dielectric was poor.[3] Another function of the barrier layer is to improve the adhesion copper to silicon and dielectric. Through a tape peeling test, it was found that the adhesion of Ta to silicon could be enhanced by annealing at 600 ℃.[9] This was due to the formation of Ta-silicon compound through annealing.[6] It is known that Ta is inert to most commonly used chemicals. Ta can be and has been used as a barrier material between copper and the dielectric. However, with the dramatic decrease of the line width in ICs, the introduction of Ta barrier reduces the space originally belonging to copper, making the latter thinner and therefore resulting in some problems. It has been considered to use Ta as the interconnection instead of copper in the future to improve the quality and simplify the manufacturing processes.

1.2. Chemical Mechanical Polishing/Planarization (CMP)

The density of devices in ICs increases exponentially, agreeing with Moore's Law.[10] In order to increase the device density, one way is to decrease the device size, and another way is to use the multilevel interconnection.

The multilevel structure was made possible using the process step chemical mechanical planarization (CMP). A nine-level interconnect will appear in 2012 according to the prediction.[11] The CMP enabled the surface ultra smooth in order to

eliminate defects with densely packed layers and benefits other processes, photolithography for instance.[12] The schematic of CMP process is shown in Fig. 1.3. The wafer fixed on the carrier is pressed face down on the polishing pad with a certain down force. Both carrier and platen can rotate independently. The CMP slurry mainly containing nano particles, oxidizer and surfactants is added to the wafer-pad interface to remove the materials on the wafer. The oxidizers such as hydrogen peroxide (H_2O_2) in the slurry oxidize the surface material, forming passivation film. Then the nano particles, like silica, alumina, and ceria, remove the passivation film mechanically. Subsequently, the passivation layer reforms on the fresh surface. It was believed that the surface planarization was achieved by the formation, removal and reformation of the passivation film.[13]

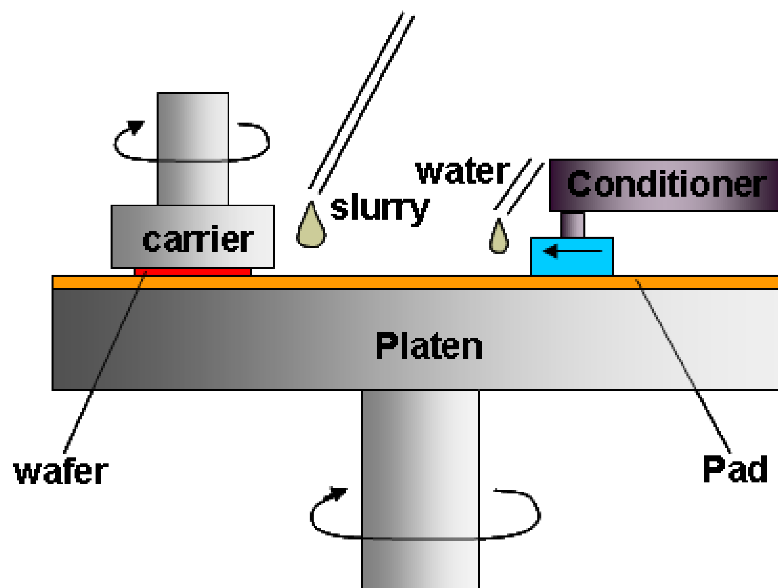

Figure 1. 3. The schematic of CMP process.

Since it was invented in early 1980s, the CMP has been performed for oxides (silicon dioxide), metal deposits (copper, tungsten, Ta), and low-*k* (low dielectric constant) materials. We focus on the metal CMP. As shown in Fig. 1.2, the over deposited copper is removed using copper CMP slurry, followed by the removal of the Ta layer with Ta CMP slurry. Only copper and Ta in trenches survive.

In CMP process, both chemicals and nano particles in the slurry contribute to the material removal, making the polishing surface ultra smooth. They are equally important. The material removal mechanisms in CMP for different materials are yet to be understood, although some were proposed. In glass polishing, Cook[14] proposed the chemical "tooth" mechanism that the substrate material was pulled off by the abrasive particles due to the chemical interactions between the glass surface and abrasives. In tungsten polishing, Kaufman and coworkers[13] proposed an alternative mechanism of oxidation that the metal tungsten was firstly oxidized by chemical reagents in the slurry and subsequently its oxide was removed by particles mechanically. Larsen-Basse and Liang[15] proposed that the removal mechanism in tungsten CMP was due to the synergy of the removal and reformation of a passivating film. The removal and formation of an oxide layer were quantified using electrochemical calculations. Steigenwald et al.[16] investigated the material removal mechanism in copper CMP in different chemicals. They found that once the chemical and mechanical reactions reached a kinetically equilibrium state, the material removal was dominated by the mechanical component followed by the dissolution of the abraded copper. Stein et al.[17] used different types of metal oxide particles as abrasives to polish tungsten surface. They claimed that the

interaction between the particles and the tungsten substrate was more complex in the tungsten removal mechanisms than the simple mechanical plowing. Similarly, Bielmann et al.[18] reported that tungsten CMP process was not dominated by the indentation and scratching mechanism. The contact area between the alumina particles and tungsten substrate enabled the interfacial chemical reactions and promoted the transfer of substrate materials. Chang[19] suggested that the material removal in a CMP process occurred at the molecular scale. The molecular bonds on the substrate surface were weakened by chemicals and then broken by abrasive particles with high thermal and mechanical energy, resulting in the material removal. A model was established by Luo and Dornfeld[20] to interpret the CMP process. They proposed that there were three material removal regions: (a) a chemically dominant and rapidly increasing region, which was determined by the generation rate and hardness of the surface passivation layer; (b) a mechanically dominant linear region, where the material removal was proportional to the weight concentration; and (c) a mechanical dominant saturation region, where the material removal saturated in that the total contact area is fully occupied by the abrasives. Generally, it is believed that the synergy of chemical reactions and mechanical reactions fulfills the material removal in CMP.

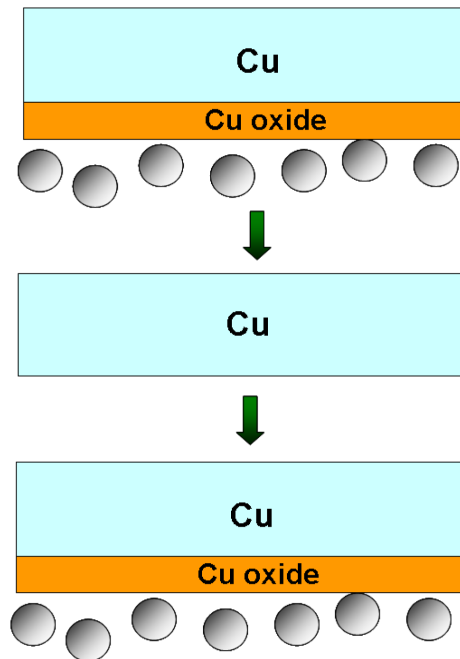

(a) The macroscopic material removal mechanism in CMP. The balls represent abrasive particles.

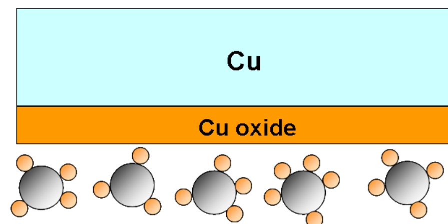

(b) The nano scale material removal mechanism in CMP. The small spheres represent copper oxide transferred to the abrasive particles.

Figure 1. 4. The material removal mechanisms in CMP.

In summary, there are two major proposed removal mechanisms in CMP. Let us take copper CMP as an example. Fig. 1.4 shows those mechanisms. In Fig. 1.4(a), the copper film is oxidized by the oxidizers in the slurry, forming copper oxide on the

surface. Subsequently, the copper oxide is removed by the nano abrasive particles in the slurry mechanically. The copper is oxidized again due to the exposure of the fresh surface to the slurry. These processes take place alternatively, accomplishing the material removal. The second mechanism is shown in Fig. 1.4(b). First, chemical reactions occur between the abrasive particles and the copper oxide. Then, the oxide is torn off by the moving particles from the oxide surface, finishing the material removal. Chang claimed that the first mechanism was wrong.[19] Actually, they are not contradictory, if we consider these two mechanisms in different dimensions. The first one stands in a large scale, while the second focuses on the nanometer scale. In order to understand the material removal mechanisms, both scales need to be considered. Although some mechanisms on the material removal in polishing were proposed, no technique for the in-situ observation on the removal processes has not been developed yet.

Since the material removal occurs at the interface between the wafer and the polishing pad, tribology, which concerns friction, wear and lubrication at the interface has been investigated in CMP. It was found that the friction during silicon dioxide polishing was affected by the abrasive particle concentration.[21] Moreover, the material removal rate was not correlated with the friction. The surfactants could reduce the friction coefficient in copper CMP due to the lubrication from the fatty components.[22] In addition, the correlation between the variation of the friction force and the removal rate suggested the copper removal mechanisms. For different material in ICs, such as silicon oxide, silicon carbide, low-*k* materials, Ta, and copper, their friction coefficients were

different under the same down pressure and rotating speed.[23] Through the surface analysis, Liang et al.[24] found that the frictional behavior in copper CMP was related to the nature of the copper oxide film and the friction energy could trigger nucleation, phase transformation and growth of the oxide layer. Due to the friction, the material transfer between the polishing pad and copper wafer was found.[25] Wear of polishing pads exists in CMP processes.[26] Abrasive wear occurred in the conditioning period, while fatigue and rolling phenomena during the polishing. The wear mechanisms in copper CMP were strongly correlated to the properties of the copper oxides.[24] The lubrication in copper CMP was investigated by Liang and Xu.[27] It was pointed out that the boundary and mixed lubrication regimes existed in copper CMP rather than hydrodynamic lubrication regime. However, the boundary lubrication regime appeared in interlayer dielectric (ILD) CMP.[28] The chemical boundary lubrication was proposed in CMP process due to the chemical interaction between the chemicals in the slurry and the polished surfaces.[29] The material removal in CMP is tightly related to the tribology.

In CMP process, the chemical etching and mechanical removal cooperate to finish the surface planarization. The mechanical factors play a significant role in CMP. Preston equation[30] (Eq. 1.2) and its modification have been accepted to describe the material removal in various CMP processes.

$$MRR = kPV \qquad [1.2]$$

where MRR is the material removal rate; P is the load or pressure applied on the wafer; V is the rotating speed of the platen; k is the Preston constant which is correlated to the polishing system. PV represents the mechanical reaction which is responsible for

removing the oxidized material from the polishing surface. The Preston equation was modified in copper CMP.[31] Besides the mechanical removal, a constant was introduced into the equation to demonstrate the effects of the chemicals in the slurry. Instead of the original Preston equation, Stein et al. used a multiterm regression function to describe the tungsten CMP process, including the effects of down force, speed, polishing temperature, abrasive particles and chemical reastions.[17] In aluminum CMP, the material removal rate was a power function of the down force and rotating speed.[32] The Preston equation could be used to predict the material removal rate in silicon dioxide CMP.[33-34] Table 1.1 summarizes Preston equations in different CMP processes. It can be seen that the Preston equations strongly rely on the polishing materials, chemicals in the slurries, and polishing systems. There is no universal equation in all CMP processes. In other words, the Preston equation needs to be established for a specific polishing process.

Table 1. 1. The Preston equations in different CMP processes.

Polishing material	Preston equation	Reference
Copper	$MRR = (kP + B)V + R_c$	31
Tungsten	$MRR = \frac{k_1 PV}{1 + k_2 PV}$	17
Aluminum	$MRR = kP^{\alpha} V^{\beta}$	33
Silicon dioxide	$MRR = kPV$	34

Note: *MRR* is the material removal rate; *P* is the down pressure; *V* is the rotating speed of the platen; other variables are constants.

According to the Preston equation or its modification, a high down force is usually used to obtain a high polishing efficiency. However, in 65 nm node and beyond technology, some fatal defects, such as damages of fragile low-*k* materials, dishing, and erosion, were resulted from the high down load.[35-37]

As discussed earlier, one approach to reduce *RC* delay is to use copper instead of aluminum due to the lower resistivity. Another way is to reduce the capacitance of ICs through lowering the dielectric constant of the interlayer dielectric materials. Low-*k* materials have been used in IC fabrication. The traditional dielectric is silicon oxide, holding the dielectric constant of 3.9. The dielectric constants of some low-*k* materials are 3.0 (carbon doped silicon oxide), 2.7 (porous carbon doped silicon dioxide), and 2.2 (porous organic polymeric dielectric). The reduction of the dielectric constant is resulted from the introduction of air in the dielectric, forming a porous structure. Nevertheless, the mechanical strength of low-k materials was lower than the traditional dielectric (silicon dioxide).[36] The generation of defects on low-*k* materials was dependent on the pressure applied in CMP process.[37] The delamination of low-*k* materials was a function of the down force during CMP.[38] In order to protect the low-k dielectric from the damages, a low down pressure is preferred in CMP process.

The high down force applied in CMP process not only leads to the failure of the low-*k* materials, but also causes dishing and erosion on IC wafers. Fig. 1.5 illustrates the dishing and erosion occurring after CMP process. Dishing is formed by losing more copper in lines in low line density areas, while erosion is the dielectric loss at high line density areas because of the overpolishing process. Dishing and erosion led to the

unevenness on the wafer surface, resulting in depth of focus problems in photolithography.[39] The smaller the dishing and erosion, the better the devices. Dishing and erosion were affected by some factors, like line width[40], pattern density[41], slurry flow rate[42], and chemistry of the slurry[43]. One reason was the local deformation of the polishing pad induced by the high down pressure in the CMP process.[44] Low down force in CMP process is needed to minimize dishing and erosion.

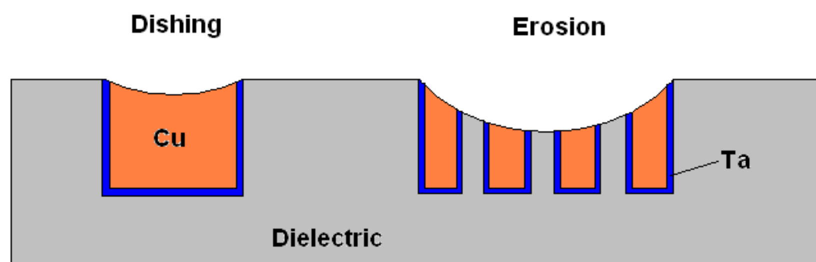

Figure 1. 5. The dishing and erosion after CMP.

Although a high down pressure used in CMP process can increase the material removal rate and therefore enhance the throughput, it induces damages to the low-*k* materials and propagates dishing and erosion. It is necessary to develop a new polishing technique to solve the current problems.

1.3. Electrochemical Mechanical Polishing/Planarization (ECMP)

As discussed in the previous section, a low down force in CMP is preferred due to the application of low-*k* materials and the minimization of dishing and erosion. Low

down force results in low throughput. ECMP has been developed and considered to replace CMP in metal polishing. In the near future, ECMP will be significantly important for the metal planarization in IC fabrication, which can polish the metal surface with ultra low down force.[35]

Briefly, in ECMP process, an anodic potential or current is applied on the polishing metal to trigger electrochemical reactions during polishing. In ECMP, the metal removal relied on the dissolution of metal atoms into the electrolyte rather than mechanical abrasion.[35] No abrasive particle or very few particles were needed in the electrolyte.[45] Defects can be minimized. Eq. 1.3 shows the typical electrochemical reaction in metal oxidation.

$$M \rightarrow M^{n+} + ne^{-} \qquad [1.3]$$

where M is the metal; n is the number of the loss of electrons during the oxidation; e represents electron. In ECMP, the metal is oxidized by the applied potential instead of chemical oxidizers in CMP. The oxidization is faster due to the existence of the extra driving force (potential). The metal oxide could be removed by the soft polishing pad with a very low down pressure and dissolved by the electrolyte.[35]

The greatest advantage of ECMP over the conventional CMP is the application of low down force which can minimize dishing and erosion and prevent low-*k* from damages. It was found that the copper removal rate in copper ECMP was independent of the down pressure from 2.07 to 6.90 kPa, enabling ultra low down force feasible.[45-46] In addition, the removal rate was a linear function of charge (defined by ampere×minutes) applied on the wafer. Through optimizing the system, all copper atoms on the surface

could be ionized, indicating that the copper ECMP process could be predictable.[35] Liu and coworkers[47] investigated the copper removal mechanism in ECMP. Copper atoms were oxidized by the applied anodic potential in the electrolyte into copper ions, followed by the diffusion of copper ions. These two processes resulted in the copper removal. The removal rate was proportional to the applied potential. They established a model to interpret the minimization of dishing and erosion. Fig. 1.6 shows the model. The field area is polished by the pad, resulting in high removal rate. A much lower removal rate is obtained in the trench due to the protection from the passivation film. Finally, the dishing will be minimized. Jia et al. also found in their copper ECMP tests that the dishing was independent of feature size and no erosion is detected.[48] Other advantages of ECMP over the conventional CMP were higher throughput and low cost[45], lower line resistance[45], higher planarization efficiency[46], easier endpoint control[48].

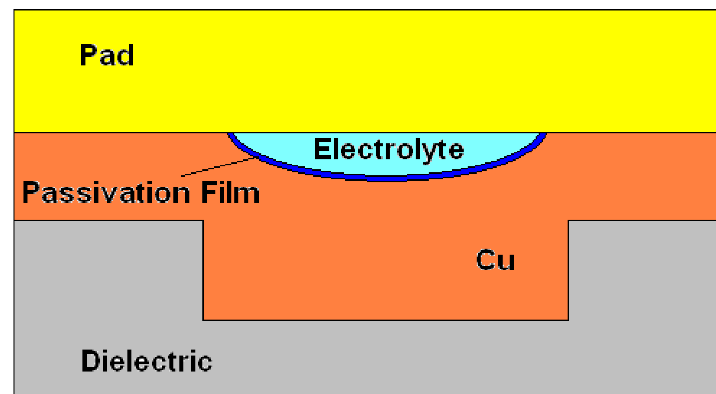

Figure 1. 6. The model of removing dishing in copper ECMP.

The copper removal is not only determined by the polishing system, like load control, polishing pad, but also affected by the voltage pattern applied on the wafer and the chemical reagents in the electrolyte. Goonetilleke et al.[49] conducted copper ECMP with the applied rectangular-voltage pulses in the electrolyte containing KNO_3, glycine and H_2O_2 at pH=4. They found that the material removal could be controlled by the voltage in the electrolyte with those three components, while the copper dissolution was retarded in the solution only containing of KNO_3 and H_2O_2. Ammonium dodecyl sulfate (ADS) which was an environmentally friendly surfactant was used as a corrosion inhibitor for copper ECMP in H_2O_2/glycine solution.[50] Compared with the conventional inhibitor—benzotriazole (BTA), the potentiodynamic polarization results showed that the corrosion inhibition efficiency of ADS was better than that of BTA. Differently from using acidic electrolyte, Oh et al.[51] used a basic electrolyte containing KOH, H_2O_2, and BTA to polishing patterned wafers. The increase of H_2O_2 concentration resulted in higher removal rate by increasingly oxidizing Cu to $Cu(OH)_2$. High uniformity within the wafer was obtained by optimizing the concentrations of chemical components. Goonetilleke and Roy[52] investigated the effect of citric acid in KNO_3 and H_2O_2 solution using potentiodynamic polarization and rectangular-voltage pluses. They found that high removal rate might be achieved by adding citric acid as a complexing agent and applying pulsed voltage instead of applying high voltage. It can be seen that the copper removal is highly dependent on the chemicals in the electrolyte. In other words, the copper ECMP can be a electrochemical-reaction-dominated process through adjusting the composition of the electrolyte.

Similarly to CMP, triobology is also important in ECMP. Our previous studies focused on the tribology and electrochemistry in copper ECMP. A setup was developed to simulate the ECMP process.[53] Using this setup, it was found that the electrochemistry of copper was strongly dependent on the pH of the electrolyte and applied potentials. The surface roughness was a function of the applied potentials. The frictional behaviors and wear mechanisms were dependent of the surface charge on the polishing pad and the surface chemical state of copper respectively.[54] The copper Pourbaix diagram was modified in ECMP under different polishing conditions.[55] In different regions of the Pourbaix diagram, the copper removal mechanisms, surface morphology, and frictional behaviors were different due to the electrochemical reactions. The electrochemistry in copper ECMP is tightly related to the friction at the wafer-pad interface.

The Ta barrier will be removed after the copper layer is removed. Ta ECMP is as important as copper ECMP. It is believed that the major reaction forming Ta oxide follows Eq. 1.4.

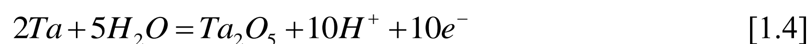

$$2Ta + 5H_2O = Ta_2O_5 + 10H^+ + 10e^- \quad [1.4]$$

Ta pentoxide cannot be dissolved by commonly used chemicals. Ta ECMP is different from copper ECMP due to the electrochemical properties. The research on the properties of Ta and its CMP and ECMP usually focused on this Ta oxide film. Robin revealed the corrosion behavior of Ta in NaOH solutions at various temperatures and found Ta passivation.[56] Ta generated a passive layer in some inorganic acid and in sodium salt solutions under an open-circuit potential (OCP).[57] The removal rate of Ta during CMP decreased with the increasing concentration of oxidizers, mainly due to the reinforced

passivation.[58] Zhang et al. investigated the removal mechanism of Ta CMP in acidic and basic solutions and found that the Ta oxide films were removed more easily at pH 2 than pH 10.[59] Different Ta complexes were found during CMP in oxalic-acid-based H_2O_2 solution at various pH, and the abrasive particles also might be involved in the surface chemical reactions of Ta removal.[60] In a recent study by Pettit et al. in Ta ECMP, it was reported that the role of $IO3^-$ in basic KIO_3 solution was to increase the local pH at the Ta sample surface and consequently promoted the formation of soluble and insoluble Ta oxides.[61] A higher Ta removal rate could be obtained when the concentrations of H_2O_2 and abrasive particles were higher.[62] It can be seen that concerns in Ta CMP and ECMP focus on the formation and removal of the Ta oxide layer on the surface.

The formation of the Ta oxide layer is a key to understand the Ta CMP and ECMP. The Ta oxide growth and oxidation process have been studied. The Ta oxide film forms in both dry and wet conditions. In dry condition, Ta reacts with oxygen, forming oxides. The growth rate of the Ta oxide film was logarithmically proportional to the exposure time in the ambient condition.[63] At 150-300 ℃, the thickness of the Ta oxide film was an inverse logarithmical function of the time.[64] The oxide growth rate was dependent of the oxygen pressure and temperature.[65] Kofstad[66] suggested the Ta oxidation sequence below 500 ℃ which might be expressed as

$$\text{Ta+O (chemisorbed)} \rightarrow \text{Ta-O (solid solution)} \rightarrow TaO_y \rightarrow TaO_z \rightarrow Ta_2O_5$$

At high temperature (> 1200 ℃), the oxide growth rate was linear to the oxidation time at a low pressure.[67] α-Ta_2O_5 and β-Ta_2O_5 which had crystal structures formed on the surface.[67] At low temperature, the thin Ta oxide film was amorphous.[68] The kinetics of

the Ta oxidation was studied by Wang et al. using X-ray photoelectron spectroscopy (XPS) in a vacuum chamber.[69] It was found that the ratio of Ta pentoxide (Ta_2O_5) increased with the increase of the exposure time in oxygen. Polycrystalline and single crystalline Ta had different activation energy in the oxidation process. The oxidation is a function of surface orientations. The oxidation rate on (110) oriented surface was higher than that on (100).[70] In addition, the oxide structures on different oriented surfaces were dissimilar. At 500 ℃ and 1 atm, the planelets preferred to grow on {320} planes.[71] It can be seen that the growth rate and structures of the Ta oxide film are a function of the temperature, oxygen pressure, and surface orientations.

Ta oxide layer can grow thicker using an anodic potential in an aqueous solution. The anodic oxide film on Ta usually appeared structureless and flat.[72-73] Under a constant anodic potential, the Ta oxide growth rate was a logarithmic function of the exposure time in nitric acid solution.[74] When applying a potential on the Ta sample in diluted sulfuric acid solution, the thickness of the oxide layer increased dramatically in the first 10 seconds and then slows down.[75] At a constant anodic potential, the reaction current decreased exponentially with the increase of the thickness of the oxide film.[73] The studies on the Ta oxidation in oxygen and solutions reviewed previously were at the steady state. ECMP is a kinetic process. Except the electrical potential, the mechanical force is another energy source. It may affect the oxidation.

The previous students in our group worked on the Ta oxidation process in ECMP. It was found that there were suboxides existing on the surface oxide layer after ECMP.[76-78] The mechanical force assisted the formation and stabilization of Ta suboxides.

However, in those studies, the Ta samples were examined using XPS after polishing. It was not an in-situ investigation. The in-situ observation on the oxide formation has not been found. The distribution of the suboxides and pentoxide during ECMP, not after ECMP, is still unknown. Furthermore, it needs to be confirmed whether the distribution of different types of oxides in Ta ECMP affects the material removal mechanisms or not.

Through reviewing the previous work in CMP and ECMP, it was found that some aspects need to be further studied to understand the polishing process. First, the material removal mechanisms in CMP and ECMP have not been confirmed, although some mechanisms have been proposed. Second, although the tribology in CMP and copper ECMP has been investigated, it has not been done for Ta ECMP. Finally, the kinetics of the Ta oxidation during ECMP has not been found.

The research studies the tribology and electrochemistry in Ta ECMP. The frictional behaviors of Ta during ECMP is investigated. The material removal mechanisms are revealed. The oxidation kinetics is discussed.

CHAPTER II

MOTIVATION AND OBJECTIVES

ECMP is accomplished by the electrochemical reactions and mechanical abrasion at the meta-pad interface. Both of them play important roles in the polishing process. As reviewed in Chapter I, the tribology in Ta ECMP has not been fully studied, which is tightly related to the mechanical abrasion. During ECMP, Ta is oxidized by the applied anodic potential. The oxidation of Ta in the dry and wet environments has been intensively investigated. However, those studies were at the static state. ECMP is a kinetic process. The oxidation of Ta in the kinetic circumstance has not been researched. The oxidation of Ta during polishing is significant to understand the material removal process. The synergy of the mechanical abrasion and oxidation process needs to be understood to optimize the Ta ECMP process.

There are four major objectives to be achieved in this research.

2.1. Developing In Situ Observation Setups

In ECMP, the tribological and electrochemical phenomena occurs at the interface simultaneously. An experimental setup will be developed to measure the friction and electrochemical reactions in situ.

2.2. Revealing Material Removal Mechanisms

The mechanisms of the material removal are the key to understand and optimize the polishing process. Unfortunately, till now no technique can observe the removal process directly. It is necessary to develop a technique to reveal the material removal mechanisms in ECMP. The material removal mechanisms will be revealed.

2.3. Establishing the Preston Equation for Tantalum ECMP

The Preston equation expresses the relationship between the material removal rate and the mechanical forces. Using the Preston equation, the polishing process can be predicted. The Preston equation in Ta ECMP will be established.

2.4. Obtaining Knowledge of the Oxidation Process in Tantalum ECMP

The oxidation is important in Ta ECMP. A new methodology will be established to investigate the oxidation state and process of Ta in ECMP.

In the next chapter, the details of the materials, experimental setups, and testing conditions will be introduced.

CHAPTER III

EXPERIMENTAL

This chapter describes materials and experimental procedures used for the present research. Their properties and selection of those materials are discussed. Characterization techniques and parameters materials are provided. Experimental setup and operating procedures are introduced in detail.

3.1. Materials

3.1.1. Tantalum

Tantalum (Ta) is a transition metal with an atomic number of 73. The density and atomic weight are 16.69×10^3 kg/m^3 and 180.95 g/mol respectively. Its melting temperature is 3017 ℃. Ta has a body centered cubic (BCC) structure (shown in Fig 3.1). The lattice constant is 0.331 nm. At room temperature, Ta is immune to most chemicals, except hydrogen fluoride, acidic solutions containing fluorine ions, and potassium hydroxide solution.

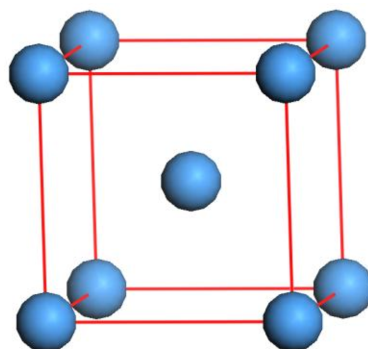

Figure 3. 1. BCC structure of Ta.

Two types of Ta samples were used in this research, annealed poly crystalline Ta disc (Sigma-Aldrich) with a diameter of 6.35 mm and single crystalline Ta (Goodfellow) with a diameter of 10 mm respectively. Both had a purity of 99.99 wt %. The single crystalline samples had different plane orientations on the surfaces, (110), (100), and (111) respectively. X-Ray diffraction (XRD) was used to examine the orientations of each sample. Fig. 3.2 shows the XRD spectra of each sample. It can be seen from Fig. 3.2 (a), (b), and (c) that these Ta samples are single crystalline. The spectrum of the poly crystalline sample is similar to that of the single crystalline sample with (110) orientation except some small peaks. This shows that the (110) orientation is dominant on the surface of the poly crystalline sample.

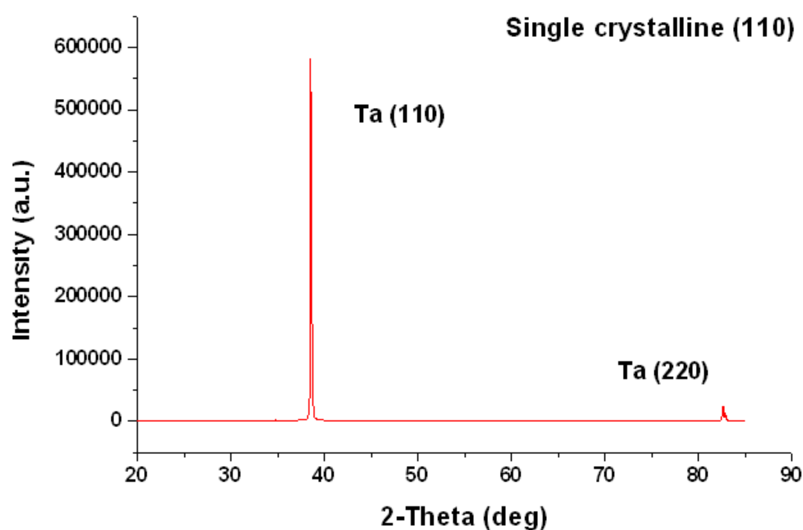

(a) Single crystalline Ta (110).

Figure 3. 2. The XRD spectra of single and poly crystalline Ta samples.

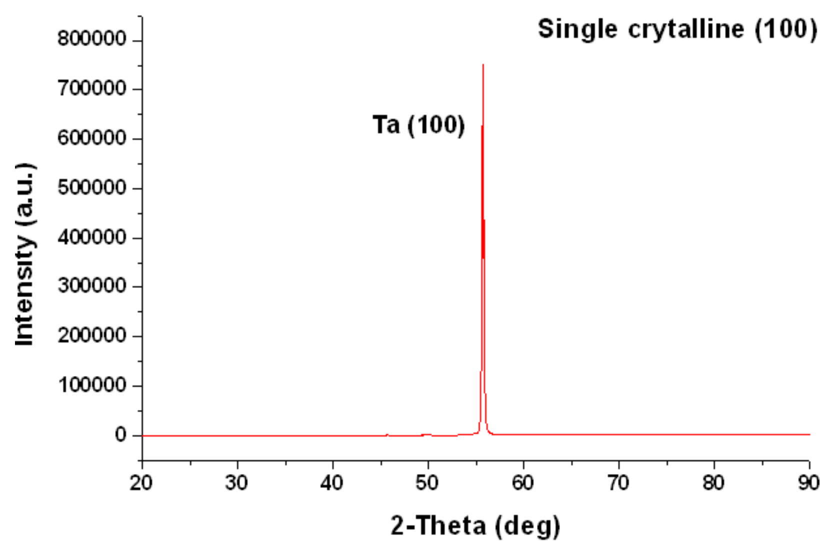

(b) Single crystalline Ta (100).

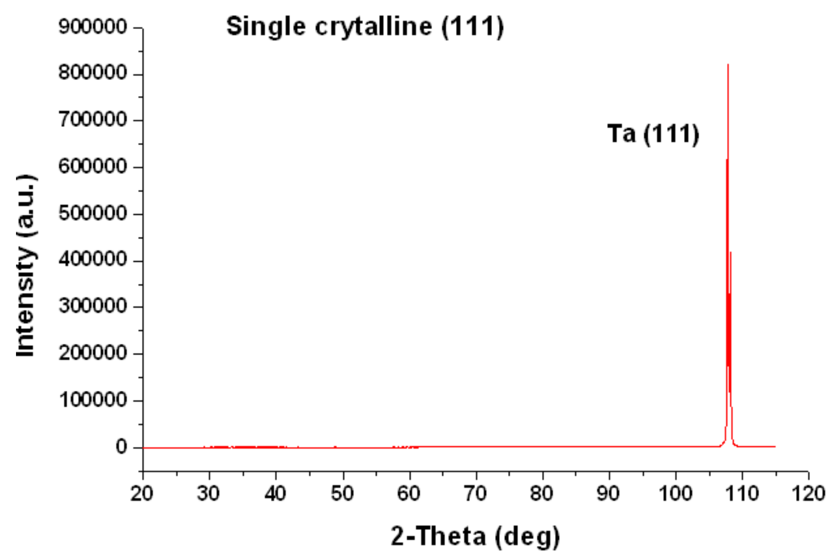

(c) Single crystalline Ta (111).

Figure 3. 2. Continued.

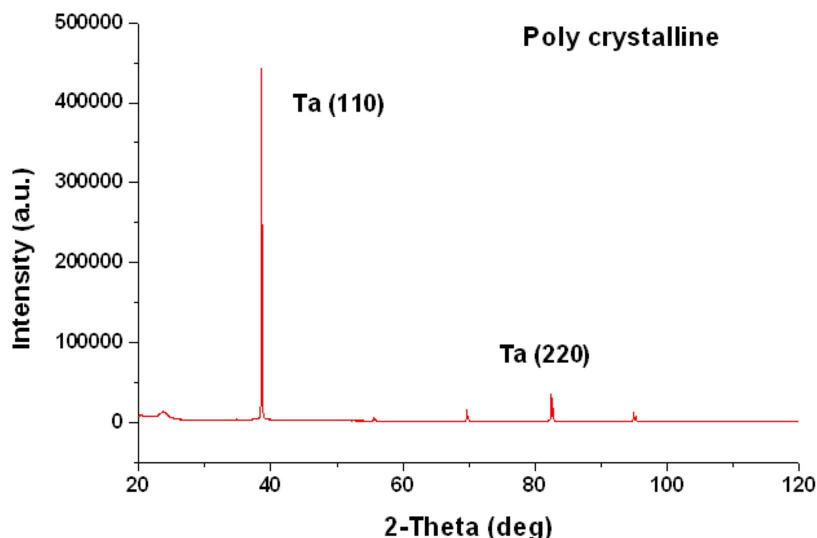

(d) Poly crystalline Ta.

Figure 3. 2. Continued.

The planar densities (atoms/cm^2) were calculated for the single crystalline Ta samples through Eq. 3.1. They were 1.29×10^{15} atoms/cm^2 for (110), 9.13×10^{14} atoms/cm^2 for (100), and 5.27×10^{14} atoms/cm^2 for (111).

$$\textit{Planar density} = \textit{atoms per face} / \textit{area of face (atoms/cm}^2\textit{)} \qquad [3.1]$$

In order to compare the planar density more conveniently, the packing fractions, calculated via Eq. 3.2, were 83.3 % for (110), 58.9 % for (100), and 34.0 % for (111).

$$\textit{Packing fraction} = \textit{area of atoms per face} / \textit{area per face (\%)} \qquad [3.2]$$

From the results, it is known that (110) is the most closed packed plane, while (111) the least. The (110) is 1.41 times denser than that of (100) and 2.45 times denser than (111).

3.1.2. Chemicals

All polishing experiments were conducted in an aqueous slurry mixed with different chemicals and abrasive particles in dioinized water (DI water). Potassium chloride (KCl, Riedel-de Haën) and sodium nitrate (Na_2NO_3, EMD Chemicals) increased the ionic concentration of the solution. Hydrogen peroxide (H_2O_2, 35 wt %, VWR International) and alumina particles (LECO Corporation) with the average diameter of 50 nm were added in order to assist increasing the material removal rate.[62] Acetic acid was used to adjust the pH value of the slurry.

In each experiment, a fresh slurry was used. To make the slurry, a certain amount of alumina particles was dispersed in DI water with agitation. Then salts and H_2O_2 were added in the solution. Finally acetic acid was added to adjust the pH.

3.2. Tantalum Sample Preparation

A series of electrochemical measurements was carried out in the slurry during polishing. A potential was applied on the sample and the electrochemical signals were measured through the same. In order to conduct electrochemical experiments, the sample must be connected to the measurement instrument. In addition, only one surface of the sample was polished. In order to satisfy these two requirements, the Ta samples were specially prepared. Fig. 3.3 shows the structure of a Ta sample. An insulated copper wire was connected to the Ta specimen with conductive epoxy. Then the whole Ta sample was sealed in nylon using epoxy. A slope was made surrounding the Ta specimen so that the load was only applied on the Ta during polishing. All Ta samples were prepared via

this method. This approach guaranteed that the electrochemical reactions only occurred on the polished Ta surface and their signals could be collected through the copper wire to the measurement instrument.

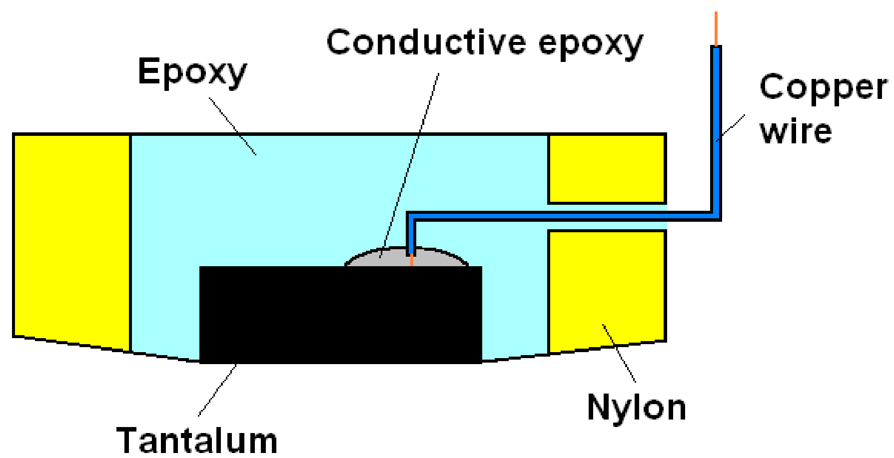

(a) The sketch of the sample.

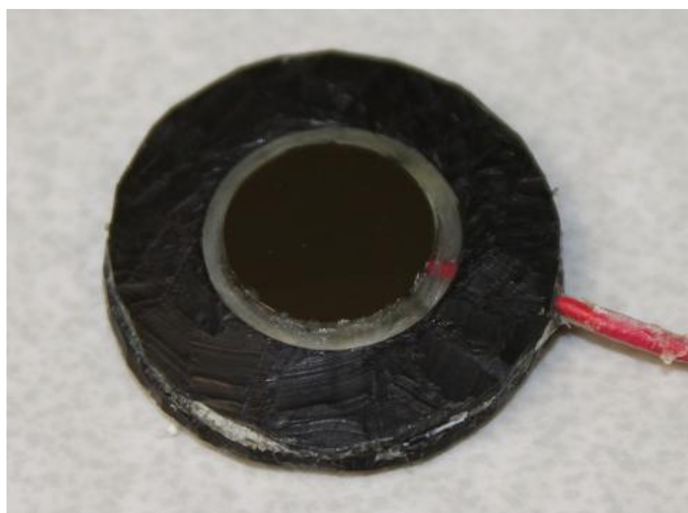

(b) The real sample.

Figure 3. 3. The Ta sample for ECMP experiments.

After sealing the Ta into the polymer, the metal surface was lapped using sandpapers on an auto polisher (Buehler) to make the bottom and top surfaces of the sample parallel. Then sandpapers with different grades were used to polish the metal surface. The finest was 1200 grid. Finally, the surface was polished by applying the silica slurry (Sturbridge Metallurgical Services) to remove all the abrasives embedded on the Ta surface.

3.3. Experimental

Electrochemical mechanical polishing (ECMP) is a tribological and electrochemical process. There is a synergy between tribological behaviors and electrochemical reactions. A new experimental setup for polishing was designed for this research. In order to examine the in-situ variation of the single crystalline Ta surfaces by using atomic force microscope (AFM), a special designed environmental cell was conducted.

3.3.1. ECMP Testing Apparatus

The polishing tests were conducted on a tribometer (CMS Instruments) which can measure the friction coefficient with adjustable rotating speeds and loads. However, this tribometer could not carry out ECMP. A specially designed container was made of non-reactive poly(vinyl-chloride) (PVC) that allows a polishing plate and pad to be submerged in a solution while rotating on the tribometer. The polishing pad, Politex (Rohm & Haas), which is usually used in final polishing in industry, was composed of

urethane and polyester. Fig 3.4 illustrates the schematic of the experiment setup. The Ta sample was pressed onto the polishing pad with a fixed load. During polishing, the friction coefficient could be measured using the tribometer. The electrochemical measurements were processed with a potentiostat (Reference600, Gamry Instruments) through a three-electrode system. This testing system consisted of three electrodes, namely reference, counter, and working electrode. The Ta sample was the working electrode, while a saturated calomel electrode (SCE) the reference and a platinum wire the counter. In tests, all electrodes were submerged in the slurry. Through this experimental setup, the tribological and electrochemical measurements were combined together.

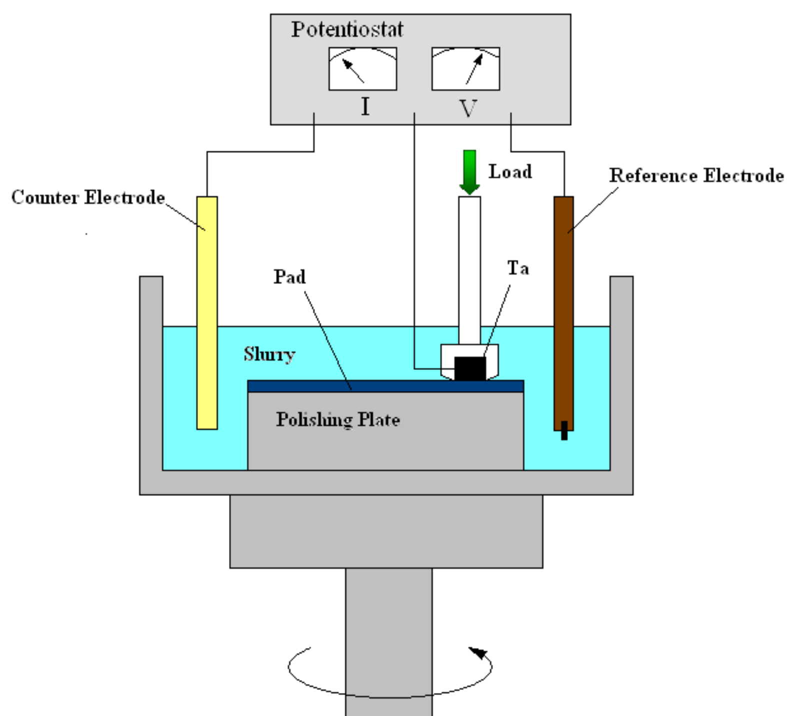

Figure 3. 4. The schematic of the experimental setup.

3.3.2. Nanoscale Experimental Configuration

The AFM (Nano-R2, Pacific Nanotechnology) is a commonly used surface characterization instrument. A sharp tip made of silicon or silicon nitride, with a radius of 10 to 30 nm at the end, slides on the sample surface. The tip is built on a cantilever. A laser is reflected by the cantilever to the detector. The detector can trace the movement of the tip. The surface topography can be measured.

AFM is usually used in a dry condition. In the present research, the AFM was used to measure the surface variation on the single crystalline Ta samples in wet conditions. An environmental cell which was combined with the AFM was necessary for these tests. Furthermore, a potential was applied on the samples to trigger the electrochemical reactions. The original environmental cell made of stainless steel did not meet this requirement due to the conductivity. A polymer environmental cell was designed and produce. Fig. 3.5 (a) illustrates the sketch of this environmental cell, while Fig. 3.5 (b) shows its photo with a single crystalline Ta sample loaded and on AFM. The cell was filled with sodium nitrate solution by using three syringes. The laser went into the cell through a glass window on the top and was reflected by the cantilever to the detector. A Ta sample as the working electrode was connected to the potentiostat with an insulating copper wire through a hole on the stage. The other two electrodes, the reference and counter respectively, were put into the syringes, forming a complete circuit. This specially designed environmental cell enables the in-situ observation on the Ta sample with conducting electrochemical tests.

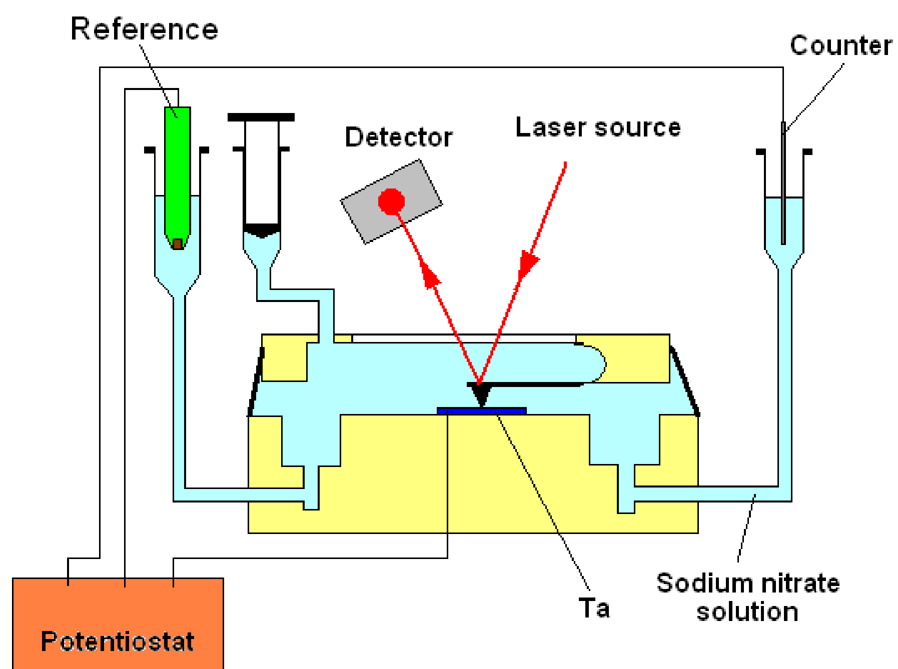

(a) The sketch of the polymer environmental cell.

(b) The photo of the polymer environmental cell.

Figure 3. 5. The environmental cell on AFM.

3.4. Fundamentals of Electrochemistry

Since the electrochemistry of metals is important in ECMP process, it is necessary to discuss its basic principles.

The value of a current may mean different things if its direction is not defined. In this research, the anodic current is denoted positive, which results in oxidation of the metal, while the cathodic current is defined negative, which leads to reduction of the metal. Defining potentials is also important. The open circuit potential (OCP) is the potential at which the metal is at an equilibrium state with the absence of any electrical perturbation, i.e. a natural state. The corrosion potential is the potential at which there is no current flow on the metal. Ideally, the corrosion potential is equal to the OCP, while they may differ due to the changes of the surface properties during electrochemical tests.

In electrochemical experiments, a controlled potential is applied on the working electrode (the specimen) via the reference electrode. The corresponding current resulted from the electrochemical reactions is measured using the counter electrode. According to the analysis of the input and output, the electrochemical behaviors can be modeled. The potential applied on the metal can be either vs. the reference or vs. OCP. Their relation is shown in Eq. 3.3.

$$E_{vsOCP} = E_{vsref} - E_{OCP} \qquad [3.3]$$

where E_{vsOCP} is the potential applied on the metal vs. OCP; E_{vsref} is the potential employed on the metal vs. the saturated calomel reference electrode (vs. SCE); E_{OCP} is the open circuit potential. When the applied potential on the metal is higher than its OCP, the anodic reaction (the oxidation of the metal) occurs, releasing electrons from the

metal atoms into the metal. On the contrary, the cathodic reaction happens as the potential is lower than the OCP, in which some species like O_2 and H^+, are reduced, taking electrons from the metal. The higher the applied potential, the more the anodic reaction, accelerating the oxidation of the metal. In this research, the conventions of the potential and current discussed above were used.

3.5. Measurement Techniques

Some electrochemical measurement techniques were employed to investigate the electrochemical performance of Ta during polishing by using the potentiostat. The AFM was used to measure the material removal rate after ECMP through imaging processes.

3.5.1. Potentiodynamic Scan

The potentiodynamic scan is a commonly used electrochemical technique to predict the corrosion rate of a metal and observe electrochemical reactions on metal surfaces.

The potential applied on the metal specimen scans from a cathodic potential to an anodic one at a certain scan rate. The current due to the electrochemical reactions is measured during the scan. Fig. 3.6 shows a typical potentiodynamic curve (Tafel curve). The Y-axis is the scanning potential, while the X-axis is the corresponding current in a logarithmic scale. The curve shows the sum of the anodic and cathodic currents. At the corrosion potential E_{corr}, which is close to the OCP, the current is the minimum, demonstrating that the anodic and cathodic reactions are balanced. In the region when the potential on the specimen is lower than the corrosion potential, the cathodic reaction

is dominant. The cathodic current should be negative according to the basics, however it is positive due to the logarithmic axis. The anodic reaction is dominant when the sweeping potential is higher than the corrosion potential. In this region, at the same potential, the higher the anodic current, the more the anodic reaction. In order to obtain the corrosion current I_{corr}, the anodic and cathodic currents are extrapolated from the linear region of each. The intersect of the extrapolated anodic and cathodic lines at the corrosion potential is the corrosion current I_{corr}. The corrosion rate then can be predicted according to the corrosion current. The corrosion current can be measured directly. In this research, the software named Echem Analyst (Gamry Instruments) was used to calculated the corrosion current and corrosion potential.

The potentiodynamic scan can examine the electrochemical behaviors of metals. It has been an accepted technique to observe the electrochemical reactions at the interface during CMP and ECMP.

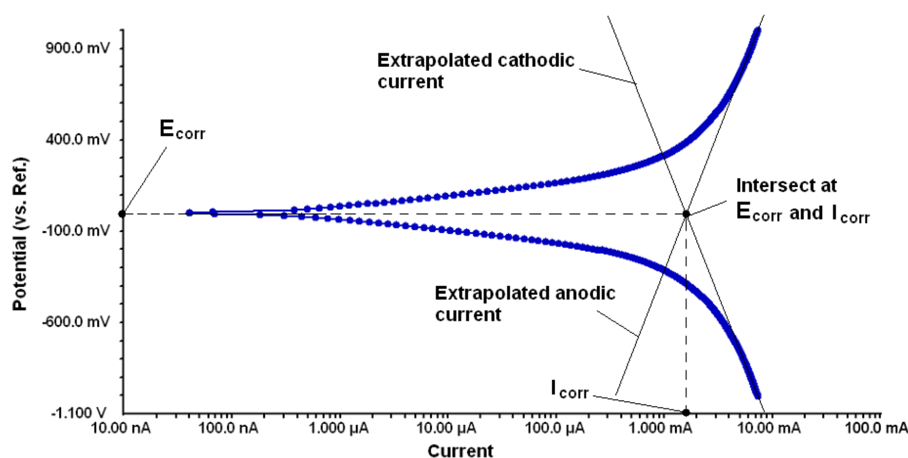

Figure 3. 6. A typical potentiodynamic curve (Tafel curve). E_{corr} is the corrosion potential. I_{corr} is the corrosion current.

3.5.2. Potentiostatic Test

In potentiostatic test, a constant potential is applied on the metal, and the current response is measured. This technique enables the observation on the electrochemical reactions with the existence of a constant potential. In an anodic reaction, the current variation demonstrates the surface change due to the passivation.

3.5.3. Potentiostatic Electrochemical Impedance Spectroscopy (EIS)

The potentiostatic EIS can be used to reveal the properties of a metal surface. The EIS has been accepted for studying reactions at interfaces and surfaces.

In this technique, a small sinusoidal excitation signal with different frequencies is applied on the metal sample and the corresponding current is measured simultaneously. The sweeping frequency of the sinusoidal signal is from high to low, 100 kHz to 0.01 Hz for example. Then the impedance of this circuit is obtained. The impedance is expressed by a complex number which contains a real part and an imaginary part. Subsequently the two parts are imposed and plotted in one figure, forming Nyquist curve (Fig. 3.7(a)). The X-axis is the real part of the impedance in ohm, while the Y-axis shows the negative values of the imaginary part in ohm. In the Nyquist plot, each point corresponds to the impedance at a certain frequency. The Nyquist curve can be expressed by an equivalent circuit, in which each component represents a property in an electrochemical cell. The equivalent circuit shown in Fig. 3.7(b) results in the Nyquist plot shown in Fig. 3.7(a) when the EIS test is conducted. R_s represents the resistance of the electrolyte, while R_p

the resistance of the oxide film on the metal and C_{dl} the capacitance of the double layer and the oxide layer.

Using potentiostatic EIS, the properties of the oxide film, such as resistance and capacitance, can be investigated.

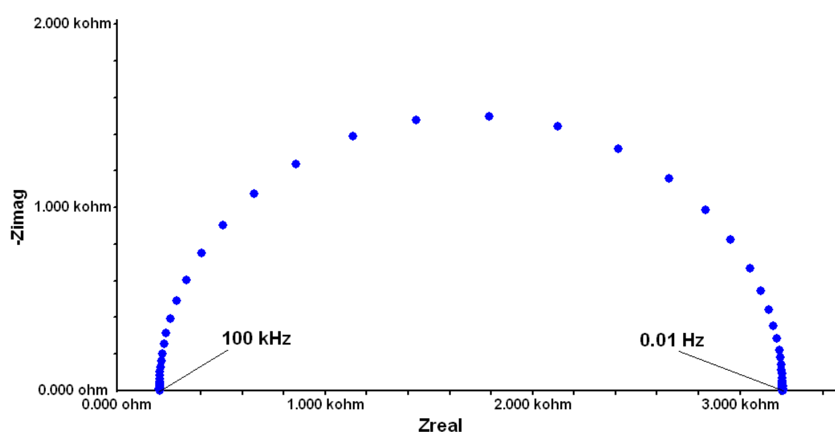

(a) The Nyquist curve. The sweeping frequency is from 100 kHz to 0.01 Hz.

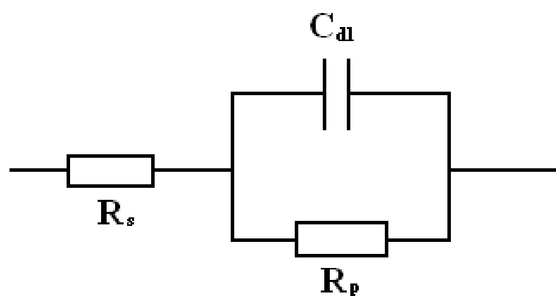

(b) The equivalent circuit of the Nyquist curve in (a). R_s represents the resistance of the electrolyte. R_p show the resistance of the oxide film on the metal. C_{dl} demonstrates the capacitance of the double layer and oxide film.

Figure 3. 7. The Nyquist curve and its equivalent circuit.

3.5.4. Single Frequency Electrochemical Impedance Spectroscopy (EIS)

As discussed in the last section, the potentiostatic EIS is a widely used tool to study surface properties of oxides and coatings on a metal surface. However, it has drawbacks. One is its test time. Since the frequency of the sinusoidal potential signal ranges from high to low values, it generally takes at least several minutes. The potentiostatic EIS is suitable for a static measurement, i.e., the surface conditions are relatively stable. The ECMP is a kinetic process due to the fact that the surface undergoes rapid oxidization and abrasion. It is not feasible to use the potentiostatic EIS to observe the surface during ECMP. A technique called single frequency EIS is more suitable for real-time measurement. Compared with potentiostatic EIS, the single frequeny EIS is simple in regard to instrumentation, experimentation, and data analysis with real-time monitoring.[79]

The principle of single frequency EIS is similar to that of potentiostatic EIS. In the former, a low value sinusoidal potential is applied to the sample with a fixed frequency instead of multiple frequencies in the latter. The sinusoidal potential is applied at an identical time interval to record the impedance change as a function of time. In the single frequency EIS, the impedance is expressed by using a complex number as shown in Eq. 3.4:

$$Z = a + jb = a + j\frac{1}{2\pi fc} \qquad [3.4]$$

where Z is the impedance, a is the real part, b is the imaginary part. We can denote $b=1/2\pi fc$, where c is the nominal capacitance, f is the frequency. Then, a and c can be

loosely referred to the resistance and capacitance of a coating or a metal oxide layer.[79] Eq. 3.5 shows the magnitude of the impedance Z:

$$|Z| = \sqrt{a^2 + b^2} \qquad [3.5]$$

The magnitude of the impedance depends on the a and b. As such the magnitude of the impedance obtained through single frequency EIS can represent, in situ, the surface state.

The single frequency EIS has been used in coatings. It can estimate the diffusion coefficient and water-volume fraction of coatings. Foyet et al. used the single frequency EIS to study the water absorption by epoxy/amine coating on Al-2024 alloy through measuring its capacitance change.[80] During Ta CMP and ECMP, a applied potential passivates the Ta surface, forming an oxide layer that can be deemed as a coating. It is possible to monitor the variation of the oxide layer in situ during CMP and ECMP processes through the impedance measurement using single frequency EIS. Although the potentiostatic EIS has been used for ECMP studies[59-61], the single frequency EIS has not been reported to be used for the same.

3.5.5. Material Removal Rate Measurement

AFM was used not only to measure the surface morphological variation in a wet condition in situ, but also the material removal rate in Ta ECMP.

Five pyramid-liked micro indents were made on the sample surface using a micro hardness tester (HM2000, Fischer Technology), shown in Fig. 3.8. Each indent was 1.5 μm deep initially. AFM was used to scan each indent with the area of 55.35×55.35 μm before and after polishing. Fig. 3.9 shows the 2-D and 3D images of an indent after

polishing. The polishing direction is also shown in the image. The ripples at the center of the image resulted from the stress due to the introduction of the indent. New indents were made every four polishing tests to ensure the accuracy.

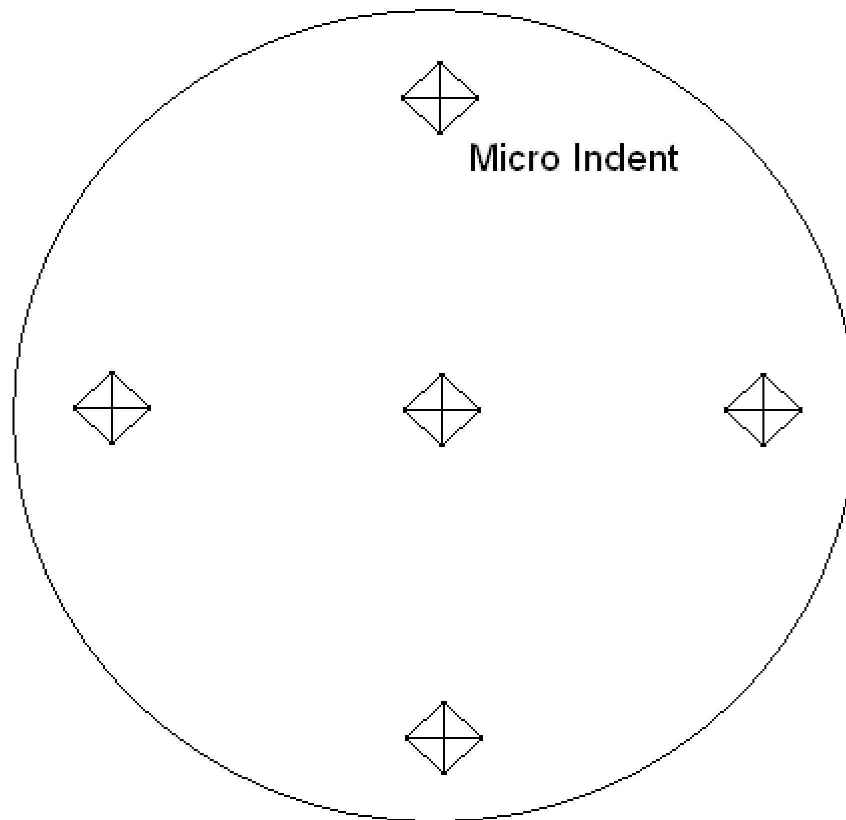

Figure 3. 8. Micro indents on the sample surface.

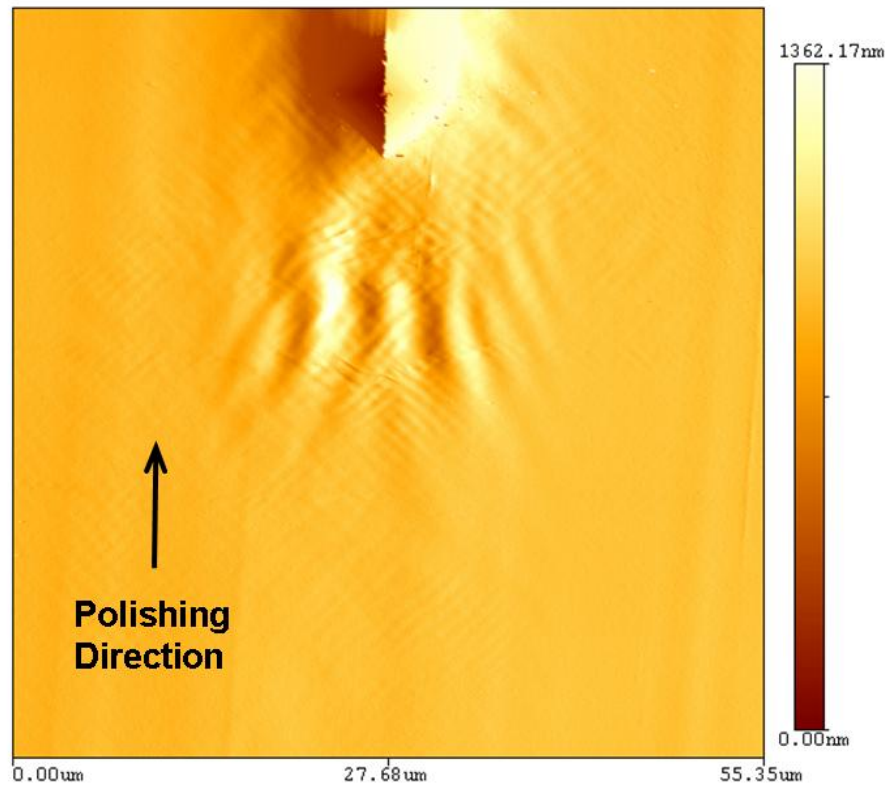

(a) 2-D image.

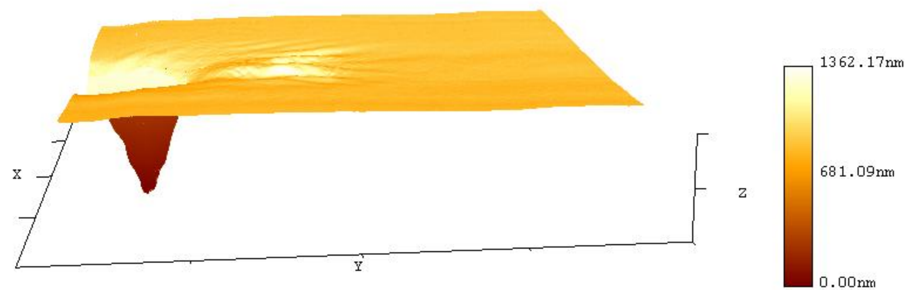

Scan Distance (55.35um)
Z Distance (1362.17nm)

(b) 3-D image.

Figure 3. 9. 2-D and 3-D images of an indent (55.35×55.35 μm).

The MRR was calculated by comparing the geometries of the indents before and after polishing through several image processing procedures. The first step is to find the reference for comparison. Since the samples were polished in one direction only, the two edges across the center of the pyramid indent paralleling to the polishing direction were unchanged. Additionally, the center of the indent did not change. The center and the former two edges were used as the reference. The next step is to find the areas for comparison (Fig. 3.10(a)). The two unchanged edged were extended to the bottom of the image. Then two rectangles were drawn 28 μm and 38μm away from the indent center respectively, being perpendicular and symmetric to the extended line. The position, length and width of the rectangles were fixed in each imaging process. The value of each data point in the rectangles represented its height to the center of the indent. For each rectangle, a line parallel to the length direction was obtained by averaging the values of the data points along width direction, which represented the average height of this rectangle (Fig. 3.10(b)). The material removal was calculated by averaging the distance between the height lines for the same rectangle obtained before and after polishing. The material removal at the indent was the average of the data obtained from rectangles 1 and 2. Finally, the global material removal was calculated by averaging the material removals achieved at the five indents. The actual material removal rate was calculated by dividing the global material removal with the polishing time. Since the polished surface is not ideally smooth, the advantage of this averaging method can minimize the effects of unpredicted surface defects, like scratches and pits. Thus the actual material removal rate can be measured by using this method.

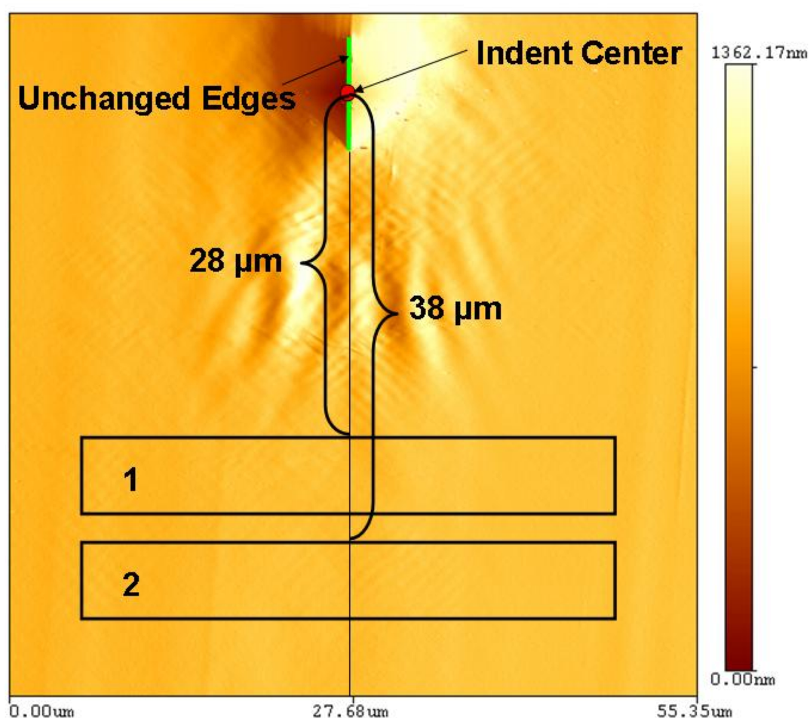

(a) Image processing for obtaining the comparing areas.

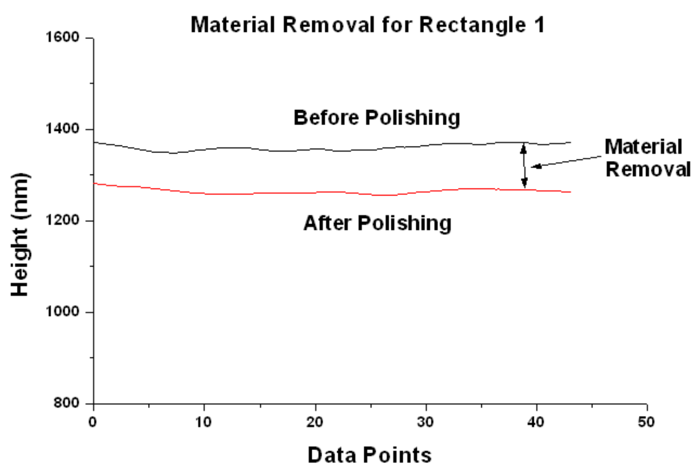

(b) The calculation of the material removal for the first rectangle.

Figure 3. 10. The calculation of the actual material removal in each polishing test. The same process for the second rectangle.

3.6. Testing Parameters and Procedures

All the ECMP experiments were conducted using the experimental setup which was introduced in section 3.3.1. In different experiments, the testing parameters, such as loads, speeds, potentials, and compositions of the slurry, are independent variables. On the polishing setup, the sample was placed 20 mm away from the axis of the container. This section introduces the testing parameters and procedures for all experiments.

3.6.1. Tribological Characterization of Tantalum ECMP

The poly crystalline Ta sample was ECMPed under different loads and rotating speeds. Table 3.1 lists the test conditions. Two different loads were applied on the sample at three different rotating speeds, 15, 30, and 40 rpm respectively under two loads of 2 N and 4 N. The slurry was made by mixing H_2O_2 (1 wt %), alumina abrasive (0.3 wt %), KCl (8 wt %), and acetic acid into DI water. The acetic acid was used to adjust the pH value of the solution to 2.05. Before each polishing test, each Ta sample was polished with alumina paste for twenty minutes to remove the native oxide layer. After polishing, a thin film of TaO_x remains on the surface, which is called "initial oxide" differing from the native one.[81] The potentiodynamic scan was used during polishing and the friction coefficient was recorded by the tribometer. In potentiodynamic, a potential between the reference electrode and Ta sample swept the sample from -0.7 V to 2.5 V at a rate of 1 mV/sec during polishing. Test samples were rinsed in DI water after each test. The impedance of the sample was measured using the potentiostatic EIS in a saturated KCl solution after each potentiodynamic-polishing process. Each sample

was scanned by a sinusoidal signal at the OCP, of which the amplitude was 10mV and the frequency was ranged from 100 kHz to 0.01 Hz. The impedance was calculated with the data from the corresponding Nyquist curve. Finally, a static electrochemical test was also carried out under a sweeping potential without abrasion. Each experiment was repeated twice.

Table 3. 1. Testing conditions.

Load (N)	Rotating speed (rpm)	H_2O_2 wt %	Abrasive wt %	KCl wt %	pH
			No abrasion		
2	15	1	0.3	8	2.5
	30				
	40				
4	15				
	30				
	40				

3.6.2. Material Removal Mechanisms in Tantalum ECMP

All polishing tests on the polycrystalline Ta followed the same procedure. Before experiments, in order to eliminate the residue on the sample surface, each sample was polished by an alumina (50 nm) paste for five minutes. In the following step, the sample was polished in the slurry for 15 minutes without applying a potential under the corresponding load and rotating speed. Now the OCP of the sample became relatively stable, showing the equilibrium state of the surface condition. Subsequently, a 20-minute ECMP was conducted with an applied potential. Meanwhile, the impedance was

measured using the single frequency EIS during polishing and the friction coefficient was recorded. Table 3.2 lists the text conditions in detail.

Table 3. 2. Polishing parameters for ECMP tests.

Group	Fixed parameters	Variables
1	60rpm / 1V	2N 4N 6N
2	4N / 1V	20rpm 50rpm 60rpm
3	60rpm / 4N	2V 1V 0V
4	60rpm / 4N / 1V	0.3 wt % abrasive 1 wt % abrasive
5	60rpm / 4N	OCP*

Note: The OCP* means that the potential applied on the sample is 0 V vs. OCP.

In Table 3.2, the variables were loads, rotating speeds, applied potentials, and abrasive. The slurry used in polishing tests was a mixer of H_2O_2, alumina abrasive, KCl, and deionized water. Its pH value was adjusted by adding acetic acid to 2.20. The concentration of both H_2O_2 and KCL was fixe at 1 wt % in all tests and that of the abrasive was 0.3 wt % that was not a variable. In each test group, there was only one variable designated. In Groups 1, 2, and 3, we aimed to study effects of load, rotating speed, and applied potential on the removal process during ECMP. In Group 4, the role

of the abrasive during ECMP was studied. The applied potentials in Groups 1 to 4 were absolute potential between the Ta sample and the reference electrode, while the potential in Group 5 was set at 0 V vs. OCP. Basically, no applied potential existed in the condition of 0 V vs. OCP. The potential was measured after 20-minute polishing as the OCP. Due to the kinetic nature of CMP, the OCP fluctuates rather than being constant. In the present research, such fluctuation was less than 1 mV which was sufficiently low, compared with the applied potential in ECMP. We therefore ignored this fluctuation. We compared CMP and ECMP in Group 5. Each test was repeated for at least twice.

In impedance measurements, the sinusoidal signal was generated and measured at the frequency of 5 Hz with the amplitude of 10 mV per second. If the frequency is too low, the impedance measurement cannot be finished in one second; if the frequency is too high, the variation of the impedance is not pronounced. The shorter the repeated time, the consistent the results because of the large amount of data. The minimum sampling time for the potentiostat was set for 1 second at the frequency of 5 Hz.

3.6.3. Preston Equation in Tantalum ECMP

The polycrystalline Ta sample was ECMPed under different polishing conditions. The slurry contained 1.5 wt % of hydrogen peroxide, 0.2 wt % alumina particles, and 2 wt % sodium nitrate. Sodium nitrate was added to increase the conductivity of the electrolyte. The pH value of the electrolyte was adjusted to 3.00 by using acetic acid. Table 3.3 shows the testing parameters. The polishing speed was the relative linear surface speed of the sample against the pad. In the first series of experiments, different

loads were employed on the sample in different polishing tests, while the speed kept constant. Subsequently, the speed varied, as the load was constant. Finally, various potentials vs. SCE were applied when the load and speed were constant. Each experiment was repeated twice. The method discussed in section 3.5.5 by using the AFM was employed to measure the actual material removal rate. The anodic reaction current was measured during the polishing.

Table 3. 3. Testing parameters.

Load (N)	Speed (m/s)	Potential (V vs. SCE)
1 2 3 4	0.08	1
3	0.04 0.06 0.08	1
2	0.08	0 0.5 1 1.5 2

3.6.4. Oxidation Kinetics of Single Crystalline Tantalum

The single crystalline Ta samples with different orientations on the surface were polished under different conditions. The composition and pH of the slurry were the same as those introduced in section 3.6.3. Table 3.4 shows the testing conditions. The polishing speed was the relative linear surface speed of the sample against the pad. The load and speed were fixed, while the only variable was the potential applied on the

samples. The potentiostatic was conducted to apply the potential on the samples and measured the current during polishing. The AFM was used to measure the actual material removal rate. Each test was conducted twice.

Table 3. 4. Polishing conditions for single crystalline Ta samples.

Load (N)	Speed (m/s)	Potential (V vs. SCE)
1	0.06	0.1 0.6

3.6.5. Material Removal in Nano Scale

The environmental cell introduced in section 3.3.2 was used to investigate the material removal in nano scale. All samples were polishing using silica slurry before experiments. The single crystalline Ta samples were fixed in the environmental cell and the AFM was used to scan the sample surface. During the tests, the cell was filled with 2 wt % $NaNO_3$ solution. The scanning probe with the radius of 10 to 30 nm at the tip was made of silicon. The contact mode was selected to scan the sample surface. The electrochemical technique of potentiostatic was used to apply a potential on samples and measure the anodic current simultaneously.

Two series of experiments were conducted. One was the dynamic test. First, the samples with different orientations were scanned using AFM. The scan area was 5×5 μm. The scanning frequency was 0.7 Hz and the resolution was 512 lines. Second, a potential of 2 V was applied on the sample for 2 min. After the anodic process stopped, the

surface was scanned again with the same parameters. Then, the same oxidation process and surface scan were repeated one more time.

The other one was the kinetic test. The surface was scanned initially with the scan area of 15×15 μm, the scan frequency of 1 Hz, and the resolution of 256 lines. Then, 2 V was applied on the sample. At the same time, the surface scan with the same parameters started. The scan was conducted 6 times continuously with the potential applied on the sample. After this potentiostatic process, a larger scan area of 30×30 μm was used to cover the small scan area with the scan frequency of 0.7 Hz, and the resolution of 512 lines.

An image processing software (Gwyddion) was used to analyze the images. The processing parameters were consistent for every image.

CHAPTER IV

TRIBOLOGICAL CHARACTERIZATION AND MATERIAL REMOVAL MECHANISMS IN ECMP PROCESSES

As reviewed in Chapter I, the synergy of the formation and the removal of the metal oxide together accomplishes the material removal in CMP. The formation of the metal oxide layer is resulted from the oxidizers in the CMP slurry. The oxide is removed mechanically due to the contribution of abrasive particle and polishing pad. The material removal is strongly related to the tribological phenomena at the wafer-pad interface. During CMP, different materials have different friction coefficient.[23] The frictional behaviors during polishing influence the material removal greatly. In ECMP, the metal oxidation is triggered by the anodic potential. The understanding on the oxide growth is essential in ECMP process.

The frictional behaviors of Ta during ECMP has not been understood thoroughly. The mechanisms of the material removal in Ta ECMP have not been understood and directly observed. In order to investigate the tribology and electrochemistry of Ta in ECMP, the experiment setup introduced in section 3.3.1 was designed and produced. This chapter discusses the tribological performance and the material removal mechanisms in Ta ECMP based on the experimental results done on this setup.

4.1. Tribological Characterization of Tantalum ECMP*

In this section, the frictional behaviors during ECMP and the properties of the Ta

*Reproduced with permission from "In Situ Observation of Friction-Induced Electrochemical Reactions and Impedance in Tantalum ECMP", by F.Gao and H.Liang, 2009. *Journal of the Electrochemical Society*, 156, H80-H86, Copyright [2009] by ECS—The Electrochemical Society.

oxide layer after ECMP are discussed based on the experimental results. The friction coefficients were obtained under different polishing conditions. The potentiodynamic scan and potentiostatic EIS were used. The testing conditions and procedures were introduced in section 3.6.1.

4.1.1. Effects of Mechanical Forces on Tantalum Corrosion Behaviors during ECMP

Tafel curves (potentiodynamic curves) can demonstrate the corrosion behaviors of a metal. This technique has been explained in section 3.5.1.

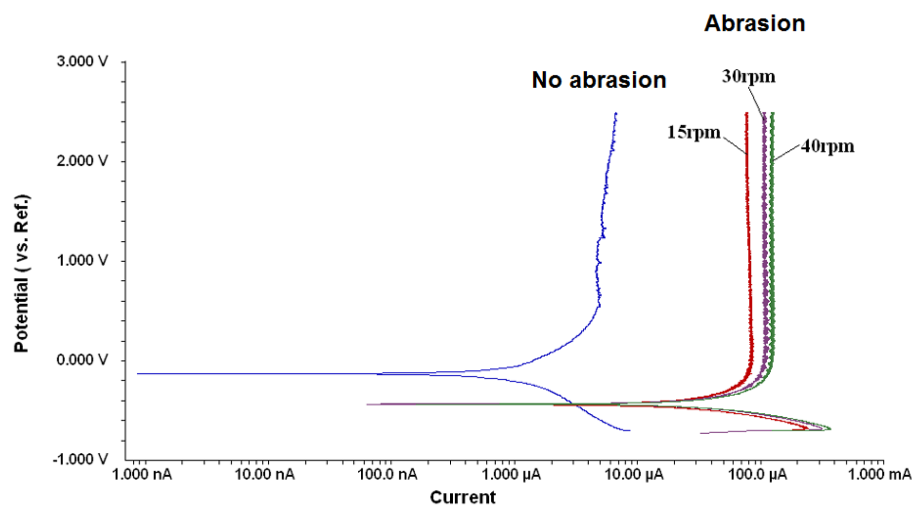

(a) No abrasion and 2 N polishing at different rotating speeds.

Figure 4. 1. Tafel curves obtained under different conditions.

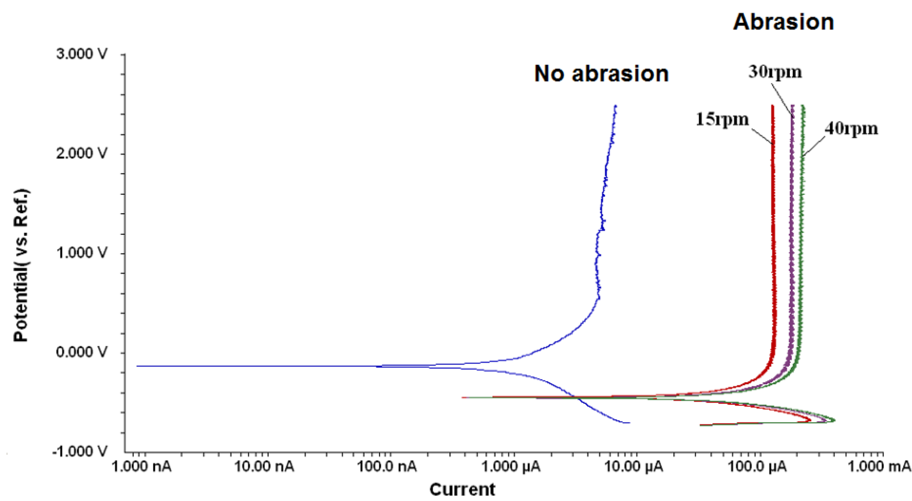

(b) No abrasion and 4 N polishing at different rotating speeds.

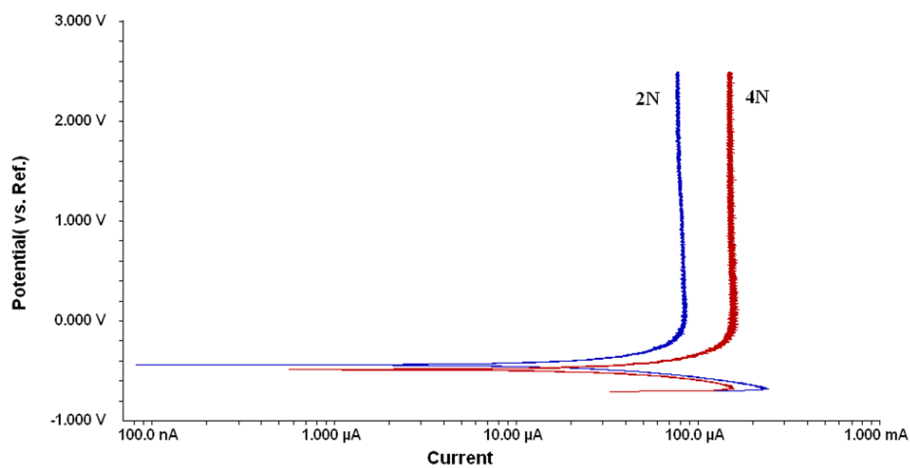

(c) 2 N and 4 N polishing at 30 rpm.

Figure 4. 1. Continued.

Fig. 4.1 shows the Tafel curves of the Ta samples measured during polishing in the slurry under different conditions. These curves are composed of sweeping potential on the Y-axis and absolute current on the X-axis in a logarithmic scale. Both cathodic and anodic corrosion current with abrasion is greater than that without abrasion and

similarly the corrosion potential of the former is less than the later. It can be observed that the current increases with the increase in rotating speeds under the same applied load, 2 N and 4 N respectively. However, the corrosion potentials do not change significantly. In addition, the current increases with an increased load at the same speed. The relationship of the corrosion potential, corrosion current, loads and rotating speeds are shown in Fig. 4.2. In this tribo–process where abrasion was generated through friction, no matter what loads and speeds were applied, those Tafel curves follow the same trend. The current changes visibly in either anodic or cathodic domain near the corrosion potential point. Nevertheless, when the applied potential is higher than ~0 V, the corrosion current is maintained to be constant.

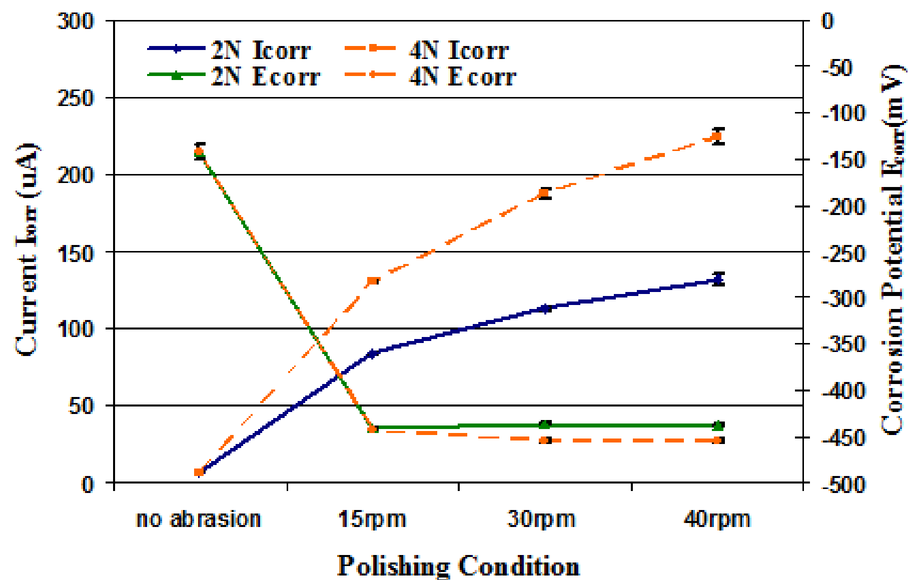

Figure 4. 2. Current and corrosion potential during potentiodynamic tests. Icorr is corrosion current, and Ecorr is corrosion potential.

In Fig. 4.1(a) and (b), the curves obtained by applying either 2 N or 4 N down force have lower corrosion potentials than that without abrasion. This is consistent with the result reported by Hariharaputhiran.[58] In the present work as shown in Fig. 4.1, the curve labeled "no abrasion" is without polishing while other conditions remained the same. The reduction of the Tafal curves indicates the effect of polishing. This means that the Ta sample being polished is prone to be attacked by the anodic reactions due to less protective oxide layer. Hence the sample surface appears to be more active (with low corrosion potential and high corrosion current in Fig. 4.1). In Fig. 4.2, it shows that the corrosion potential does not change significantly with increased rotating speeds except under a high load. These results show that the surface with extensive material removal is more active than that with mild polishing. The higher the mechanical energy, the more the oxide layer was removed.

In Fig. 4.1(a) to (c), Tafel curves shift to the right (toward high corrosion current) in both cathodic and anodic regions when the speed and/or the load are/is increased. This indicates that during ECMP, electrochemical reactions can be enhanced by the increase in mechanical energy (load or rotating speed). Fig. 4.1 shows that the load is more pronounced than the speed.

The Ta surface is passivated gradually with an increase of potential in the anodic region, forming the oxide layer. With abrasion, when the potential is positive, the current density is maintained constant. At a certain value of potential versus mechanical parameters (load and speed), the electrochemical reactions and the mechanical removal are kinetically balanced. During polishing, the surface material (oxides) is removed.

When the sweeping potential is higher than the corrosion one, the oxide layer begins to form, i.e. the surface is passivated. In the range between the corrosion potential and 0 V, the passivation is slower than mechanical abrasion thus the surface layer is removed partially. This is the case of Fig. 4.1. The passivation becomes dominant with the increased electrical potential. When its value reaches >0 V, the passivation dominates and forms a stable oxide layer.

In terms of CMP, the formation and removal of an oxide layer alternate. When applying a potential to a certain critical value, an oxide layer forms. This is again the balance between passivation and removal. Without abrasion, the current increases with the increasing potential. With abrasion, i.e. during polishing, the surface can be planarized and passivated uniformly. The uniformity of the passivating film is responsible for the behavior shown in Fig. 4.1.

4.1.2. Effects of Mechanical Forces on Tantalum Oxidation

The potentiostatic EIS introduced in section 5.3.3 can reveal the properties of the metal oxide layer. It was used to measure the impedance of the Ta sample in a saturated KCl solution after each potentiodynamic test.

Nyquist curves of impedance measurements were plotted in Fig. 4.3 after the polishing tests with 2 N load at three different speeds. Another Nyquist curve was shown in the same diagram when 2 N and 30 rpm were used without a sweeping potential. The plots obtained under 4 N are similar to those of 2 N tests. Semicircles are presented in Nyquist diagrams except for the polishing only test. Each solid line in the diagram is the

fitted curve with the Randles model. The fitted curves can be used to calculate the corresponding impedance. Fig. 4.4 shows the double layer capacitance C_{dl} and polarization resistance R_p of the Ta sample after each potentiodynamic polishing test for different conditions. The highest polarization resistance was obtained in the non-abrasion test (Fig. 4.4(a)), and the double layer capacitance is the second highest (Fig. 4.4(b)). The R_p for both 2 N and 4 N increases with an increase in the rotating speed. The value of the polarization resistance is similar for each polishing condition at the same rotating speed and different loads. An apparent increase of C_{dl} can be seen for 2 N tests, where the double layer capacitance obtained under 4 N does not change much. It is clear that the C_{dl} of 4 N polishing is greater than that of 2 N.

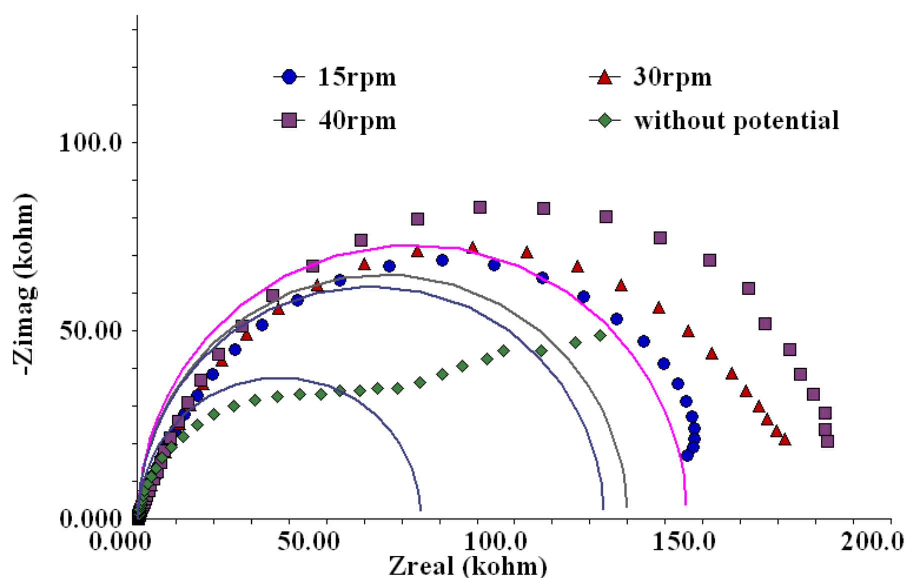

Figure 4. 3. Nyquist curves for non-potential polishing and 2 N polishing at different speeds.

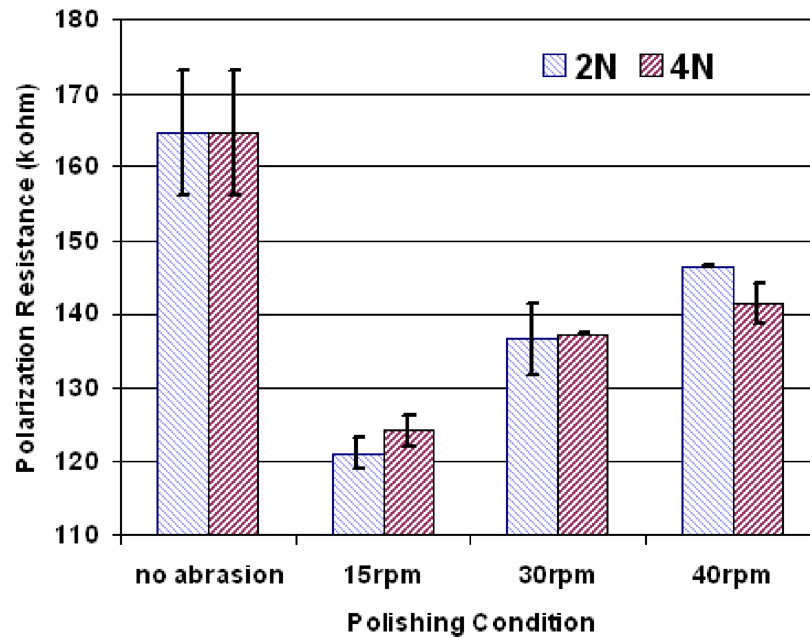

(a) Polarization resistance obtained under different polishing conditions.

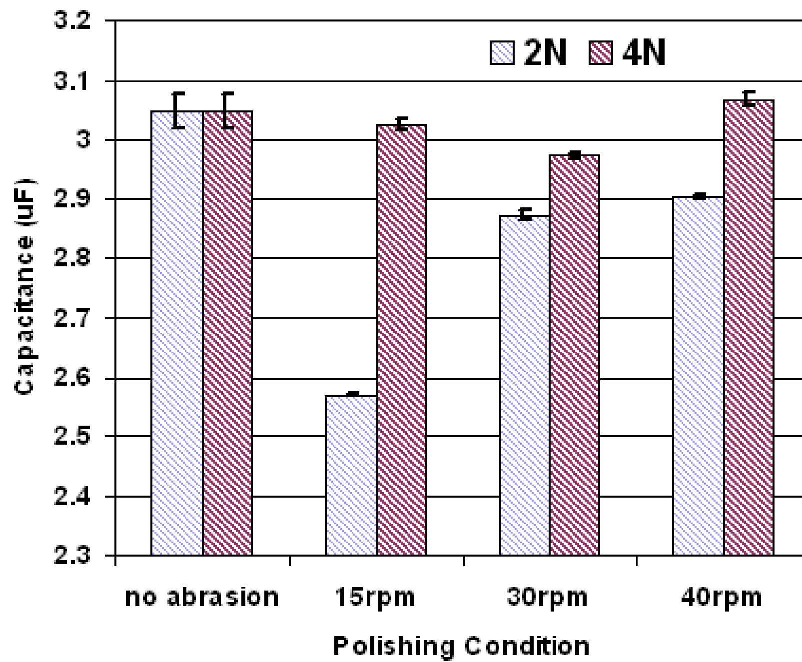

(b) Double layer capacitance obtained under different polishing conditions.

Figure 4. 4. Results of impedance measurements.

The semicircle Nyquist curves obtained after polishing with scanning potential can be simulated using the equivalent circuit known as Randles model as shown in Fig. 4.5(a).[82] In this circuit, C_{dl} and R_p are connected in parallel and then in series with the so-called solution resistance R_s representing the electrolyte resistance between the reference electrode and the sample. The semicircle curves mean that the surface is well passivated and covered by an oxide layer.[56] The Nyquist curve of the polished sample without potential is similar to the Nyquist diagram of a mixed control circuit including the Warburg impedance W in series with $R_{p.}$ The Warburg impedance equivalent circuit of this curve is shown in Fig. 4.5(b).[82] The Warburg impedance is resulted from the diffusion on the surface. Applying these diagrams to the current work, without potential and during polishing, the Ta surface was not protected by an oxide layer, similar to the case shown in Fig. 4.5(b). With an applied potential, as shown in Fig. 4.5(a), a protective oxide layer is formed.

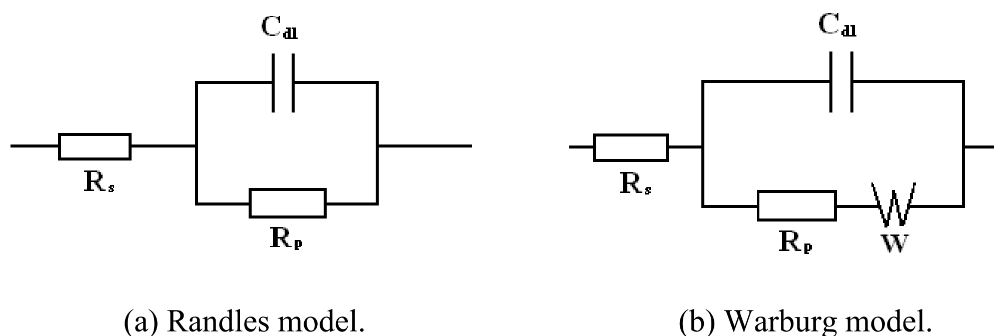

(a) Randles model. (b) Warburg model.

Figure 4. 5. Equivalent circuit for Randles model and Warburg impedance.

The resistance of the oxide film can be represented by the polarization resistance R_p measured using the EIS technique. Since friction can abrade the oxide layer through sliding, the polished samples have thinner oxide layers and further reduced R_p. Nevertheless, the unpolished (no abrasion) surface has the highest polarization resistance (Fig. 4.4(a)). It is known that the mechanical energy depends on the sliding speed (distance) and the friction force. A higher removal rate is expected with increased mechanical abrasion. If the nature of oxides is the same, the R_p of a surface should reduce with thinning the oxide layer. Our results show that the R_p is somehow independent of applied load and increases with the increase in rotating speed. The remaining possibility is the formation of different types of oxide films. As a matter of fact we have previously reported effects of mechanical energy on formation of Ta suboxides.[78] The resistance of a surface film is proportional to the resistivity and inversely proportional to the distance. This means that the thinner the oxide layer, the higher the resistivity.

It is well known that the double layer capacitance is affected by several variables including temperature, ionic concentration, types of ions, oxide films, surface roughness, among others.[83] All impedance measurements in the present work were carried out in a saturated KCl solution at room temperature and the surface roughness is similar. The nature of an oxide layer is the only possible variable thus the C_{dl} represents the capacitance of the layer. In terms of the calculation equation of capacitance, it can be expressed as:

$$C = \varepsilon_0 \varepsilon_r \frac{A}{d} \qquad [4.1]$$

where C is the capacitance; ε_0 is the permittivity of free space; ε_r is the material dielectric; A is the area of each plate; d is the separation between the plates. When the area and ε_0 are fixed, the capacitance is decided by ε_r and d. Although the oxide layer generated without abrasion is thicker than those with abrasion, the dielectric of such oxide may have more significant effects on the value of the permittivity than the separation distance. Nevertheless, the oxide layers are associated with the friction and the thickness when they are dominants. In such, their capacitance increases with the increase of the rotating speed and load.

4.1.3. Frictional Behaviors during ECMP

Friction coefficients were recorded during potentiodynamic experiments. The results are shown in Fig. 4.6. The X-axis is the test time and the Y-axis is the friction coefficient. It is seen that the friction coefficients obtained under 4 N are higher than those of 2 N. For the 2 N tests, the friction at different rotating speeds is relatively similar, while for 4 N curves, after about 600 seconds, the friction coefficients decrease with the increased rotating speeds. All curves show the same trend. There is a decrease in friction during the first 200 seconds, reaching a minimum at approximately the same time in all tests. The coefficients then increase reaching a maximum also at the same approximate time followed by a decrease to an extended period of time. In Fig. 4.7, in comparison with the friction coefficient curve (2 N, 30 rpm) with the sweeping potential, the curve with the absence of potential was obtained when applying the same load and speed. The latter decreases continuously with time during polishing, unlike the curve

gained with potential. Since the sample was polished with applying the sweeping potential simultaneously, the Tafel plot can be combined with the curve of friction coefficient in Fig. 4.8. The polishing condition of this diagram is under 4 N and at 30 rpm. There are two curves shown in the figure. The Y-axis on the left is the friction coefficient while the right is the corrosion current. The X-axis on the bottom is the test time while the top is the sweeping potential. The shape of the friction curves is similar to all other tests. The friction coefficient curve is observed having three stages as labeled in Fig. 4.8 as stages 1, 2 and 3 respectively. In the stage 1, comparing with the current curve, it is interesting to see that the corrosion potential takes place at about -0.45 V or 250 sec, right after the lowest friction is reached. After that with the increase of sweeping potential, the friction coefficient reaches the peak value (stage 2). Subsequently, the friction starts to decrease at the 0 V in the stage 3.

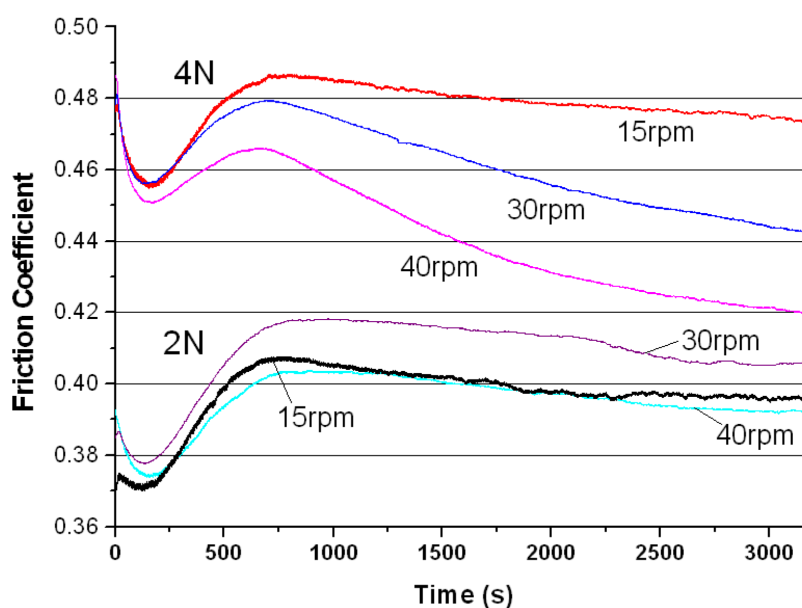

Figure 4. 6. Friction coefficients for different loads and rotating speeds.

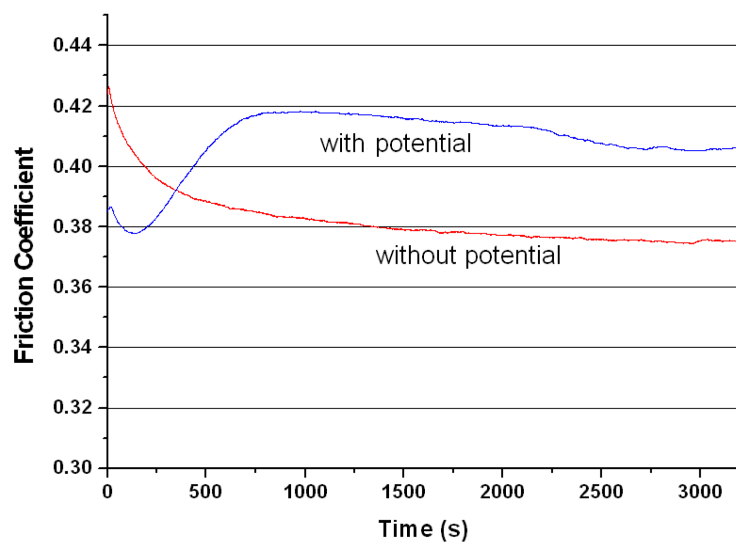

Figure 4. 7. Friction coefficients obtained with sweeping potential and without potential, 2 N, 30 rpm.

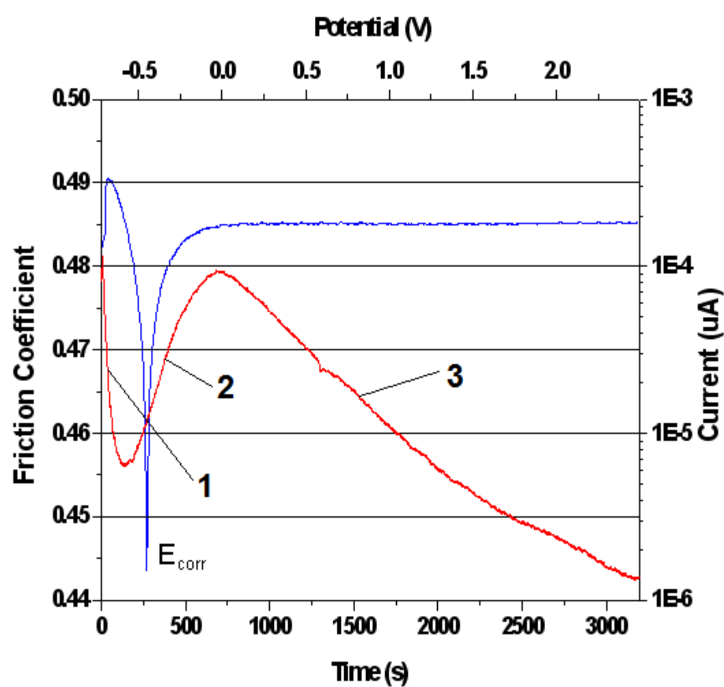

Figure 4. 8. Friction coefficient and corrosion current, 4 N, 30 rpm.

The friction coefficient is denoted by the ratio of the friction force generated at the interfaces and the normal force. In Fig. 4.6, the friction coefficient obtained when applying 4 N at each rotating speed is higher than that under 2 N at the corresponding speed. This phenomenon can be explained by the model proposed by Thakurta et al. for CMP on a soft and porous polishing pad.[84] In his mode, a larger area of contact between the sample and the pad is induced by a higher down force. The slurry film thickness decreases with the increase of load, thereby resulting in the increase of the fluid shear stress, corresponding to an increased friction. The higher the load, the higher the friction coefficient. This is particularly so for a soft pad. Additionally, comparing the friction coefficient curves with and without a potential (Fig. 4.7), it is verified that the sweeping potential causes the change of the friction coefficient.

In order to understand the mechanisms of electrochemical-mechanical polishing, the sweeping potential versus corrosion current was plotted, combining the friction curve as shown in Fig. 4.8. Two curves in the diagram were obtained under 4 N and the 30 rpm for comparison. In this curve, there are basically three stages shown as labeled. We will analyze each stage respectively later. The friction coefficient is mainly affected by the permutation of five factors listed in Table 4.1. In the table, we denote each factor with a capital letter for the convenience of explanation. The function and effects of each factor are also tabulated.

Table 4. 1. Factors affecting the friction coefficient.

Denotation	Factor	Function	Effect
A	Cathodic reactions	Dissolute oxides from the surface chemically	Reduce COF*
B	Mechanical abrasion	Remove oxides from the surface mechanically	Reduce COF
C	Oxidation by H_2O_2	Oxidize surface and generate oxides	Increase COF
D	Anodic reactions	Passivate surface and generate oxides	Increase COF
E	The local concentration of abrasive particles	Affect contact area	Affect COF

* COF is the coefficient of friction.

It has been reported that the friction coefficient follows a linear relationship with an applied (positive) potential.[76] This means that the passivation does indeed increase the friction. Under the mechanical abrasion (A) and the cathodic reactions (B), where the surface layer could be removed or formed in a slow manner, the friction is expected to be low. On the contrary, anodic reactions (D) can increase the friction coefficient by generating oxides on the surface, similar to the report in reference [76]. Additionally, the oxidation by H_2O_2 (C) would also contribute to the increase of friction. This is similar to the report by Kuiry et al.'s experiments of Ta at pH 2 in a H_2O_2 solution.[85] As mentioned earlier, the friction coefficient could be affected by the change of the contact area between the sample surface and the abrasive particles.[86] In such, the local concentration (E) at the interface is expected to affect friction. Among the factors listed in Table 4.1,

the cathodic reactions (A), the anodic reactions (D), and the local concentration of abrasive particles (E) are affected by the sweeping potential, as shown in Fig. 4.1, while the mechanical abrasion (B) and the oxidation (through H_2O_2) are not expected to show any effects since their value were fixed.

In the stage 1 of Fig. 4.8, the factors of A, B, C and E are discussed in terms of their effects on friction. The alumina particles are positively charged in an acidic KCl solution.[87-88] When the sweeping potential is negative, the positively charged particles are attracted to the sample surface, increasing the local concentration of such particles, i.e. the contact area. As a result, the A and B are beneficial for the decreased friction as well as the oxide removal. The C and E, on the other hand, increase the friction or enhance the oxide thickness. In the stage 1, A+B are the dominants, i.e. A+B>C+E. In such, friction decreases. The symbol ">" means importance.

With the increase of the sweeping potential, the cathodic reactions are not as active as at its earlier stages (Fig. 4.8) and the concentration of abrasive particles on the sample surface are relative low. At the beginning of the stage 2, the potential approaches to the corrosion potential. The cathodic reactions become so weak that the C+E begins to be dominant although the E decreases. As a result, the friction starts to increase from a minimum value. When the sweeping potential is higher than the corrosion potential E_{corr}, the anodic reactions (D) become more involved through passivation. The combined effects of C, D and E on friction are greater than B alone, i.e., C+D+E>B. Consequently, the friction coefficient continues to increase.

When the potential reaches 0 V, the friction coefficient curve enters the stage 3. The anodic reactions become stabilized that is proven by the constant corrosion current (Fig. 4.1). The positively charged surface repulses the same charged particles. The reduced real contact area of particle-sample decreases the friction. The higher the potential, the lower the concentration, and the lower the friction coefficient. In this stage, the factor E is the only variable, while others remain unchanged. The factors of B+E, which contribute to friction reduction, are the dominants, i.e. B+E>C+D. As seen, the ECMP is a synergetic process that involves five modes: cathodic reactions, mechanical abrasion, oxidation, anodic reactions, and the surface charge of sample and particles.

4.2. Material Removal Mechanisms in Tantalum ECMP*

In the last section, the results of the potentiodynamnic scan showed that the mechanical energy resulted from the load and rotating speed during polishing affects the electrochemical reactions of Ta, i.e. the formation of the Ta oxide layer. When the applied potential is higher than 0 V vs. SCE, the passivation and mechanical abrasion are balanced. However, the relationship between the formation of the oxide layer and the mechanical energy induced by the friction force has not been revealed. In this section, we discuss this relationship, i.e. the material removal mechanisms in Ta ECMP. The detailed testing conditions and procedures can be found in section 3.6.2.

*Reprinted with Electrochimica Acta, 54, F.Gao and H.Liang, Material Removal Mechanisms in Electrochemical–Mechanical Polishing of Tantalum, 6808-6815, Copyright (2009), with permission from Elsevier.

4.2.1. Material Removal Mechanism

The single frequency EIS was used to investigate the material removal mechanisms in Ta ECMP. The details of this technique can be found in section 3.5.4.

Briefly, in the single frequency EIS, the magnitude of the impedance of Ta oxide film can be expressed by Eq. 3.5, where *a* is loosely referred to the resistance of the oxide layer, and *c* is the nominal capacitance which can refer to the capacitance of the oxide film.[79] The resistance increases as the oxide layer becomes thicker.[89] The capacitance of an oxide layer can be defined by Eq. 4.1. As a result, the thicker the oxide film, the smaller the capacitance, and the greater the reciprocal of the capacitance, and vice versa. The influence of the thickness of an oxide layer on the capacitance has been accepted.[90] Based on previous report and above discussion, according to Eq. 3.5, the nominal resistance *a* and the reciprocal of the nominal capacitance *b* increase or decrease simultaneously when the oxide layer thickness increases or deceases correspondingly. Consequently, the change of the impedance magnitude reflects the variation of the thickness of the oxide layer.

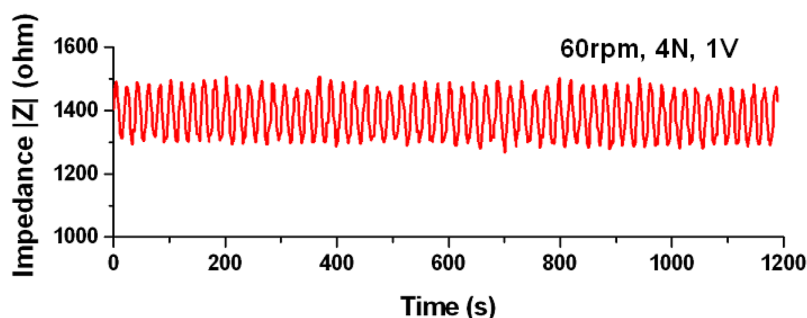

Figure 4. 9. Impedance curve obtained at 60 rpm, 4 N, and 1 V.

Fig. 4.9 shows a typical impedance plot when the Ta was polished with 60 rpm rotating speed, 4 N load, and 1 V potential for 20 min. The X-axis is the polishing time in second while the Y-axis the impedance in ohm. The impedance varied periodically. As shown in Fig. 4.9, the magnitude of the impedance |Z| of the Ta sample varies periodically in ECMP process under certain polishing conditions, indicating the periodical change of the thickness of the oxide layer. In ECMP, an anodic potential is applied to help the formation of the oxide layer through electrochemical reactions, making the oxide layer thicker. Meanwhile, the mechanical abrasion resulted from load, rotating speed, abrasives as well as polishing pad removes the formed oxides from the metal surface, reducing the thickness of the oxide layer. The electrochemical reactions and mechanical abrasion compete, i.e., the growth and removal of the oxide layer depend on the dominating factor. The mechanical abrasion during ECMP is relatively consistent under the fixed polishing parameters, like load and rotating speed. It has been accepted that the growth rate of Ta oxide layer was inversely proportional to the thickness.[91] At a constant potential, the growth rate of the oxide layer declines with the increase of its thickness, being shown by the exponentially decreasing current density.[89] Further electrochemical reactions are suppressed by the passive layer. On the contrary, once the oxide film is thinned, its growth rate increases. In the ECMP process, when the oxide is removed by the mechanical abrasion to a certain thickness, the electrochemical reactions are dominant to grow the oxide layer at a higher rate, resulting the increase of the impedance. The electrochemical reactions forming a thick oxide layer are weakened by the increase of the thickness. Then, the mechanical abrasion is more pronounced than the

electrochemical reactions to remove the oxide, causing the declination of the impedance. Additionally, the oxide layer cannot form or be removed instantaneously. In other words, it takes time to form and remove the oxide. As such, the increase and decrease of the oxide layer thickness are periodic, reflected by the periodic variation of the impedance. Furthermore, the periods are different due to the different thickness of the oxide layer and abrasion conditions when the polishing parameters are changed. In summary, the synergy of the electrochemical reactions and mechanical abrasion affecting the thickness of the oxide layer accomplishes the metal removal in ECMP process. This is the mechanism of the material removal in ECMP.

4.2.2. Quantification of Material Removal

As discussed preciously, the formation and mechanical abrasion of the Ta oxide film accomplish the material removal process. In order to convenience the discussion, the quantification of the impedance curves and the mechanical abrasion was done.

The impedance curves were quantified. Sine functions were used to calculate the period of each impedance curve. Firstly, the impedance data from 500 to 700 sec in ECMP process were extracted in order to observe in detail. The data shown was in the middle of the polishing. Secondly, a sine function (Eq. 4.2) was designed to simulate the curve shape. The period of the sine function is the period of the impedance variation by comparison.

$$|Z| = A + B\sin(\frac{2\pi}{T}t + \theta) \quad [4.2]$$

where $|Z|$ is the magnitude of the impedance, A is the average of the impedance during the whole ECMP process, B is the amplitude of the sine function which can be set arbitrarily, T is the period, t is the polishing time, and θ is the phase shift. The A and T are the average of repeated experiments.

The mechanical abrasion was calculated. During polishing, the material on the sample surface was removed mechanically by the friction force existing between the sample surface and polishing pad as well as abrasive particles. The mechanical abrasion through friction contributes to the material removal. The mechanical abrasion can be represented by the mechanical power introduced by the friction force.

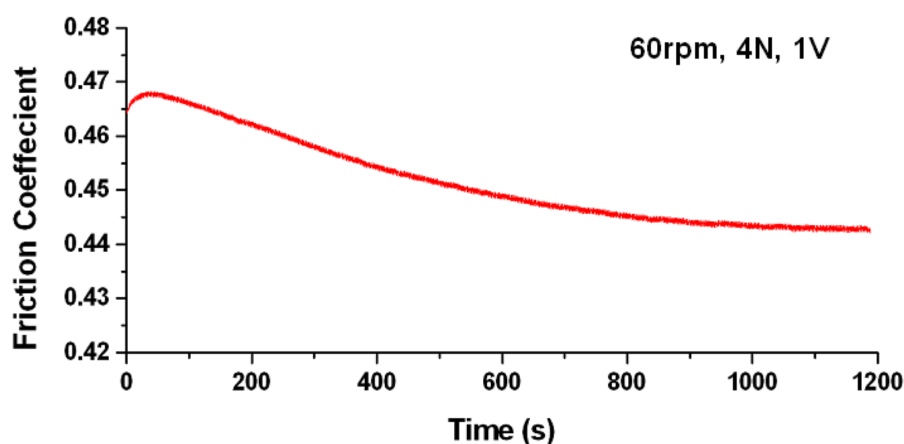

Figure 4. 10. A typical friction coefficient curve obtained under the polishing conditions of 60 rpm, 4 N, 1 V.

First, we calculate the friction force. The friction force is obtained by multiplying the friction coefficient and the vertical load. The friction coefficient was recorded during CMP or ECMP. Fig. 4.10 shows a typical friction coefficient curve when 60 rpm, 4 N,

and 1 V were applied during polishing. The friction coefficient deceases with time. This is consistent with the results shown in section 4.1.3. Since the friction coefficient was not constant during the polishing process, the average friction coefficient was obtained by using Eq. 4.3.

$$\overline{\mu} = \frac{\int_0^{\tau} \mu dt}{\tau} \quad [4.3]$$

where $\overline{\mu}$ is the average friction coefficient, μ is the friction coefficient, τ is the total polishing time in second. Secondly, calculate the average friction force with Eq. 4.4.

$$F = \overline{\mu} F_n \quad [4.4]$$

where F is the average friction force in Newton, F_n is the vertical load. Finally, the pure mechanical power resulted from the friction force can be calculated by Eq. 4.5.

$$P = VF = 2\pi\omega RF \quad [4.5]$$

where P is the mechanical power in watt, V is linear speed of the polished sample, ω is the rotating speed, R is the distance (20 mm) between the sample and the spinning center of the platen.

Table 4.2 lists the calculated mechanical power induced by the friction force. Also, the periods and average impedance obtained in different experiments are listed for comparison. In the first group, the mechanical power increased with the increased load. The power was the highest in all polishing tests when 6 N was applied. In Group 2, the lowest mechanical power appeared at 20 rpm. The mechanical power inclined when a higher rotating speed was used. Different potentials were applied in the third group of experiments. The higher the potential, the lower the mechanical power. However,

compared with data in Groups 1 and 2, the difference of the mechanical power obtained under different potentials was relatively small, i.e., less than 0.008 W. It is thus reasonable to believe that the power gained under different potentials was similar. In the fourth group, a higher concentration of the abrasives in the slurry resulted in high mechanical power. When the same load and rotating speed were applied, a similar mechanical power was obtained in CMP and ECMP processes.

Table 4. 2. The mechanical power and work introduced by the friction force.

Group	Fixed parameters	Variables	Period (s)	Average impedance (Ω)	Power (W)
1	60rpm / 1V	2N	24.79±2.75	1820.87±131.83	0.1336±0.0035
		4N	21.41±0.36	1316.65±47.75	0.2237±0.0048
		6N	15.91±0.28	1193.48±70.14	0.3297±0.0143
2	4N / 1V	20rpm		2033.53±79.23	0.0903±0.0056
		50rpm	18.57±1.59	1459.19±83.13	0.1962±0.0043
		60rpm	21.41±0.36	1316.65±47.75	0.2237±0.0048
3	60rpm / 4N	2V	21.17±1.91	1551.56±62.83	0.2173±0.0182
		1V	21.41±0.36	1316.65±47.75	0.2237±0.0048
		0V	21.08±1.70	1129.97±23.52	0.2315±0.0002
4	60rpm / 4N / 1V	0.3 wt.% abrasive	21.41±0.36	1316.65±47.75	0.2237±0.0048
		1 wt.% abrasive	18.13±0.96	1166.78±16.40	0.2490±0.0013
5	60rpm / 4N	CMP		965.30±55.08	0.2355±0.0137
		ECMP	21.41±0.36	1316.65±47.75	0.2237±0.0048

4.2.3. Factors Affecting the Material Removal

This section discusses the factors which affect the material removal process during Ta ECMP based the mechanical power, the periods and averages of the impedance curves.

The mechanical abrasion plays an important role in the ECMP process. It is a function of the rotating speed and the friction force existing at the interface between the metal surface and polishing pad. Hence, the mechanical power calculated previously with the friction force and rotating speed can characterize the mechanical abrasion. There are two questions regarding the mechanical abrasion need to be answered. One is the thickness and the other the oxidation/removal rate. The former corresponds to the average impedance which shows the thickness of the oxide layer, while the latter the period of the impedance curve. Let us take a bulldozer as an example to explain those two questions. In one single plough, a bulldozer with higher power can remove soil more and faster than one with lower power. Correspondingly, the mechanical abrasion with higher power can remove thicker oxide material.

Fig. 4.11 shows the impedance curves and their corresponding sine curves between 500 and 700 sec when different loads were employed with the same rotating speed (60 rpm) and potential (1 V). On the right, there are periods T of simulated sine functions, and the average numbers A of the impedance curves obtained during 20-minute ECMP. The standard deviations are also listed here. The amplitude of simulated curve was set slightly higher in order to highlight the original curve clearly. It can be seen both period and average impedance decrease with the increase of the applied load.

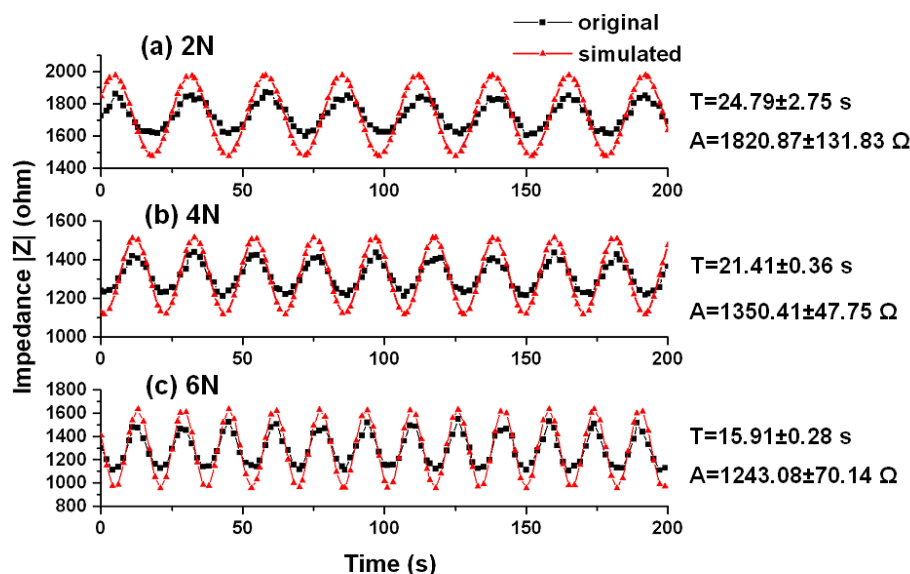

Figure 4. 11. The enlarged impedance curves and sinusoidal simulation curves with different loads at 60 rpm and 1 V.

In Fig. 4.11, all curves are periodic, showing the mechanism of the material removal. Comparing the data listed in Table 4.2, it is found that the higher the mechanical power, the lower the average impedance and the shorter the period. The mechanical abrasion with a high power removes more oxide layer resulting in a low impedance. As mentioned previously, the growth rate of the oxide layer is inversely proportional to its thickness at a constant potential. That means the thinner oxide film takes less time to grow to the thickness at which the electrochemical reactions are no longer dominant, resulting in a shorter period. Consequently, the Ta sample abraded with

a higher load has shorter period and thinner oxide layer shown by lower average impedance.

In Fig. 4.12, different rotating speeds were applied in polishing, as the load and potential were kept constant. When the sample was polished at 20 rpm, the data points of the impedance were random, unlike those in other curves and therefore no sine function was found. The average number of the impedance, when 50 rpm was applied, was higher than that at 60 rpm, while the period of the former was shorter than that of the latter.

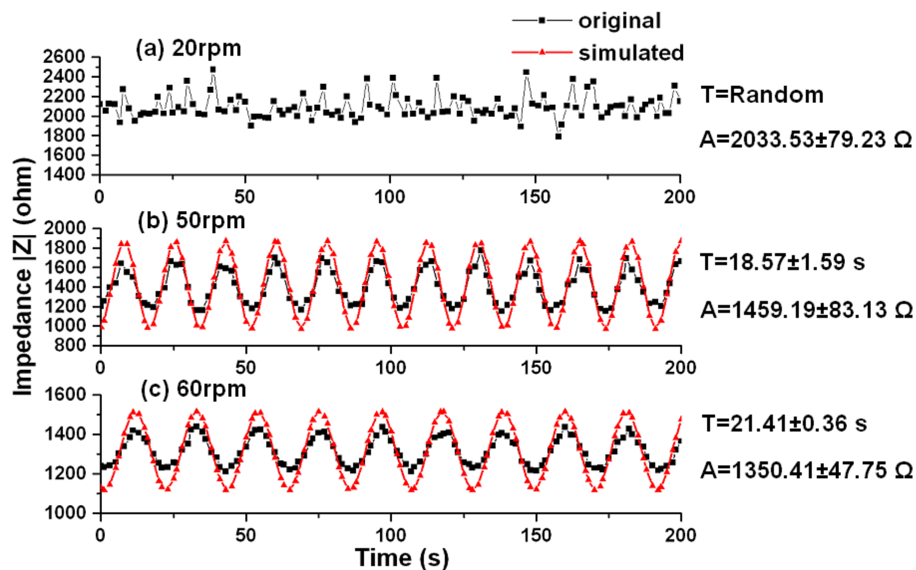

Figure 4. 12. The enlarged impedance curves and sinusoidal simulation curves with different rotating speed under 4 N and 1 V.

The impedance curves in Fig. 12 are periodic except the curve obtained at 20 rpm. The data in Table 4.2 shows that at 20 rpm the average impedance is the highest,

indicating the thickest oxide layer and the mechanical power is the lowest. Only little oxide material is removed from the surface with such low mechanical power and hence the oxide growth is relatively stable. As a result, the impedance curve does not show the thickness change nor is periodic. From the Table 4.2, a higher mechanical power appears when polished at 60 rpm, compared with that at 50 rpm, inducing more oxide removal at higher rotating speed. Thus, the oxide layer is thinner at 60 rpm, reflected by the lower average impedance. The results of periods of these two impedance curves are opposite to the corresponding results that the higher the mechanical power, the shorter the period. There should be some extra power to help remove the surface material. Under a constant load, the smaller distance between the sample surface and a polishing pad is attained at lower rotating speed. Subsequently, the abrasive particles collide the sample surface frequently due to the small space available. That may be the source of extra power. Although at 50 rpm the growth rate of the oxide layer is lower due to a thick film, the oxide thickness is less than that at 60 rpm because of the existence of the extra power. Accordingly, the period of the impedance curve obtained at 50 rpm is shorter than that at 60 rpm.

Fig. 4.13 shows the impedance results under different potentials when the load and rotating speed were fixed at 4 N and 60 rpm respectively. The periods obtained under different potentials are similar, compared with those shown in Fig. 4.11 and Fig. 4.12. The average impedance decreases gradually with the decreased potential.

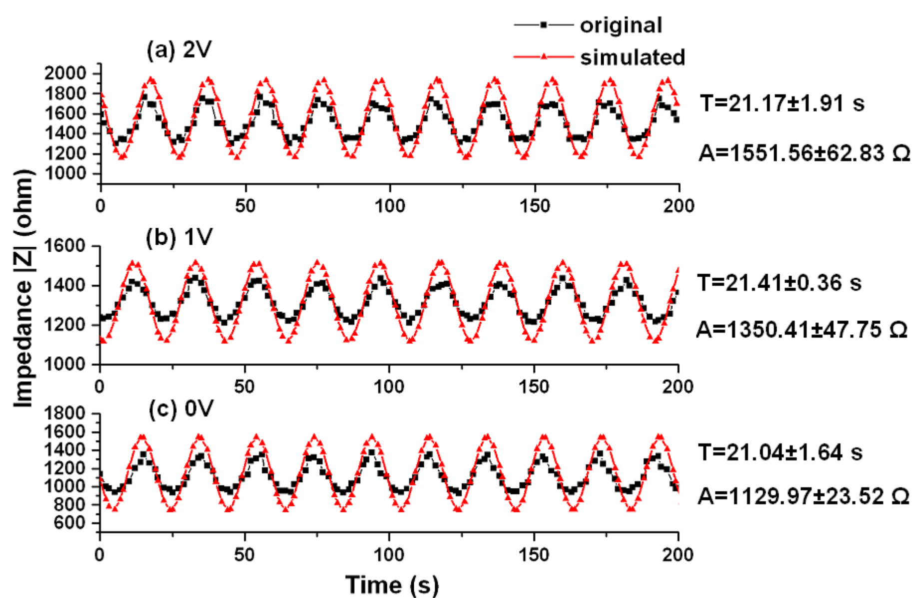

Figure 4. 13. The enlarged impedance curves and sinusoidal simulation curves with different potentials when 4 N and 60 rpm were applied.

In Fig. 4.13, different potentials were applied on the Ta sample during ECMP while the load and rotating speed were fixed at 4 N and 60 rpm. The average impedance increases with the elevated potential, showing the thickness growth of the oxide layer. Macagno and Schultze reported that the thickness of the Ta oxide film grew linearly with the electrode potential in acidic solution.[92] It can be seen that the mechanical power obtained under different potential in Table 4.3 is similar. That implies the mechanical removal is similar in those three cases. The growth rate of the oxide film is not only a function of its thickness, but also the applied potential. The higher the potential, the higher the growth rate due to extra energy. Although the oxide layer formed under 0 V is thinner than that under a higher potential, the growth rate of the former is lower than that

of the latter in terms of lower potential. Therefore, the growth rate under different potentials is close, resulting in similar periods.

Fig. 4.14 shows the influence of the abrasives in the slurry on the period of the impedance variation and the impedance average when the load, rotating speed, and potential were 4 N, 60 rpm, and 1 V respectively. When the concentration of the abrasive changed from 0.3 to 1 wt %, both period and average impedance decreased.

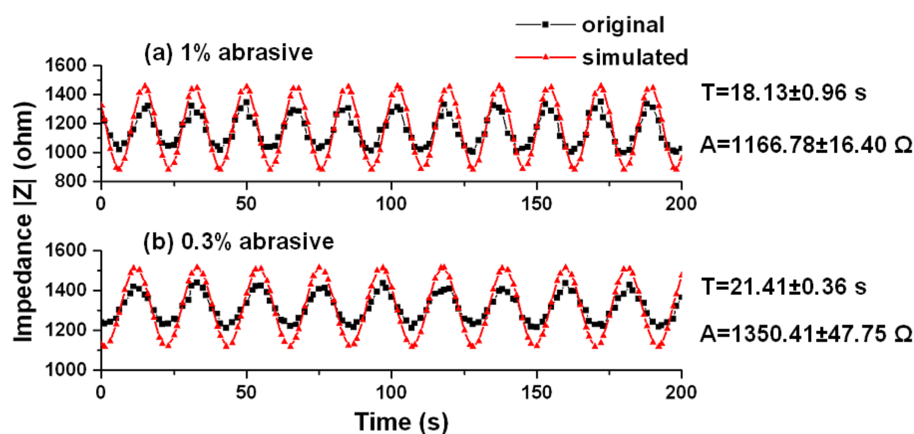

Figure 4. 14. The enlarged impedance curves and sinusoidal simulation curves with different concentrations of abrasive when 4 N, 60 rpm and 1 V were applied.

As shown in Fig. 4.13, when the concentration of abrasives increased from 0.3 wt % to 1 wt %, both average impedance and period decreased with rest polishing parameters fixed. A high concentration of the abrasive particles results in a large contact area between particles and the sample surface, causing a high friction force.[93] Hence, the mechanical power induced through friction is high. Subsequently, more oxide material is

removed by mechanical abrasion with a high power. As shown earlier, the average impedance and period decreases with the increase in the amount of the abrasives. Muthukumaran et al. also reported that the higher concentration of abrasive particles results in higher material removal rate in Ta ECMP.[62]

Fig. 4.15 presents the CMP and ECMP processes. The potential applied in Fig. 4.15(a) was 0 V vs. OCP, showing a CMP process. Fig. 4.15(b) reveals a typical ECMP process. The average impedance in CMP is lower than that in ECMP. Although the impedance curve of the CMP is not as apparently periodic as that of the ECMP, we still can think it periodic except the period of each circulation is not identical and much shorter than that of the ECMP.

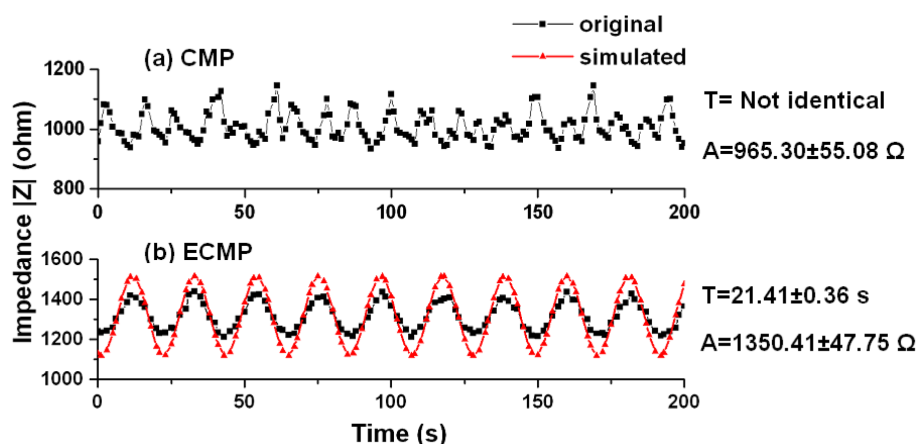

Figure 4. 15. The enlarged impedance curves and sinusoidal simulation curves of CMP and ECMP when 4 N and 60 rpm were applied.

In ECMP, both potential and H_2O_2 contribute to the formation of the oxide layer, while in CMP process Ta is oxidized only by H_2O_2. Thus, without the contribution of the potential, the thickness of the oxide layer in CMP is much smaller than that in ECMP, reflected by the low impedance for the former. In Fig. 4.15(a), it can be seen that the impedance oscillates with nonidentical period. The period obtained in the CMP process is much shorter than that in the ECMP, because the thin oxide layer of the former results in a high growth rate of the oxide layer corresponding to a stronger mechanical stimulation. The oscillation of the impedance curve in CMP reveals its material removal mechanism, the formation, removal, and reformation of the oxide material.

In order to examine how the mechanical abrasion induced by the load and rotating speed affected the oxide layer in ECMP process, Fig. 4.16 was plotted to show their relationships. The potential was 1 V and the concentration of abrasives was 0.3 wt %. The average impedance decreased with the increase of the calculated mechanical power.

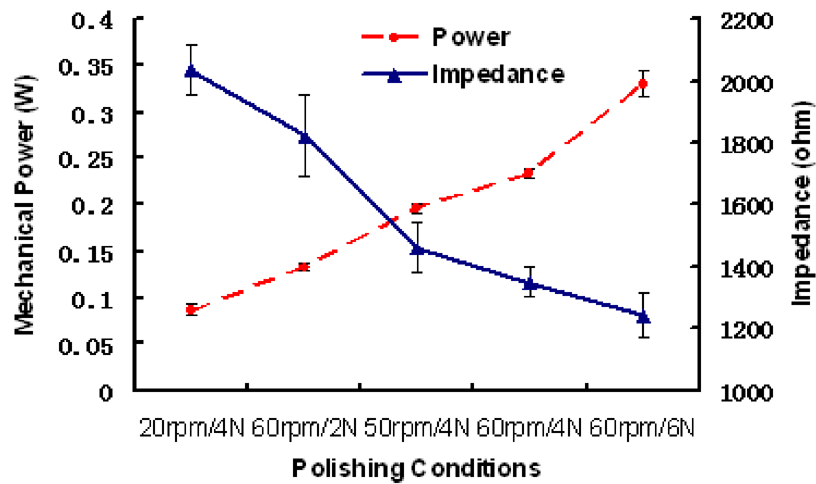

(a) The relationship between the mechanical power and average impedance. The load and rotating speed are the only variables. The potential is 1 V and the concentration of abrasives is 0.3 wt %.

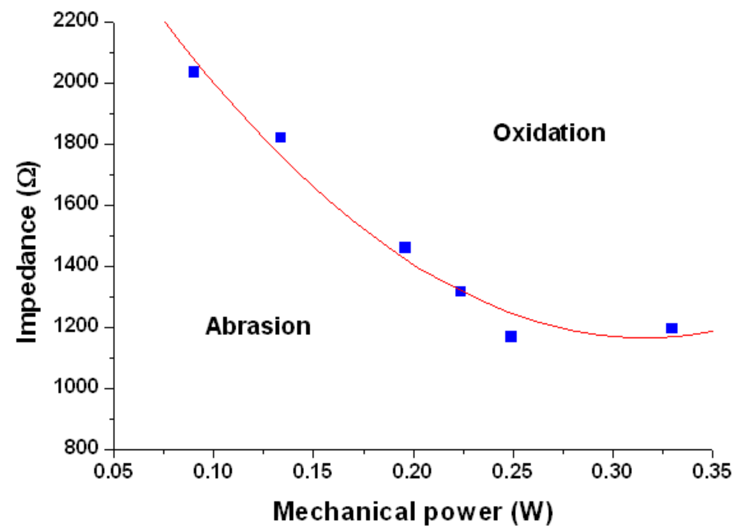

(b) Impedance as a function of mechanical power. The curve divides the removal mechanisms into two regions. The upper is dominated by oxidation and lower by mechanical abrasion.

Figure 4. 16. The relationship between the mechanical power and the impedance.

In Fig. 4.16, it is interesting to see the reverse relationship between power and impedance. The average impedance reflects the thickness of the oxide layer while the mechanical power is to remove it. Here, we only consider the scenarios in which the load and rotating speed are variables because they are readily adjusted in practice. The composition of the slurry and applied potential (1 V) remained unchanged. In order to highlight the relationship, the impedance is plotted against the input power, as shown in Fig. 4.16(b). The impedance reflects the thickness of the oxide layer and it is found to be a function of the mechanical power through load or rotating speed. This plot divides the synergetic process into two regions, oxidation and removal. The oxidation and mechanical removal compete with each other. The upper region is dominated by the oxidation and lower the mechanical removal.

4.3. Kinetics of the Material Removal

Based on the discussion in this chapter, it was found that the synergy of the oxide growth and mechanical abrasion accomplishes the material removal process. This verified the material removal mechanism proposed by Kaufman at al.[13] in CMP. In Ta ECMP, both the oxidation of Ta induced by the applied anodic potential and the mechanical removal rooted from the friction at the sample-pad interface play important roles.

Fig. 4.17 illustrates the Ta ECMP process, summarizing the relationship between the electrochemistry and the friction force occurring at the interface. The applied anodic potential enhances the anodic reaction (oxidation) of metallic Ta, thickening the oxide

layer which is reflected by the increase of its impedance. The friction force at the interface removes the oxide from the surface, making the oxide layer thinner. The friction is influence by several factors, such as the surface electrochemistry, mechanical parameters (load and rotating speed), and the surface charge of the sample and abrasive particles. The electrochemical energy, i.e., the oxide formation, and the mechanical energy, i.e., the mechanical removal compete. When the oxide layer is thick enough, the oxide growth rate slows down dramatically due to the retard from the oxide layer. The mechanical removal becomes dominant at this moment. The mechanical energy is higher than the electrochemical energy, leading to the oxide removal and therefore the decrease of the oxide layer. When the oxide layer is thin enough, the oxide growth rate increases significantly. The electrochemical energy dominates in the process. The electrochemical energy is higher than the mechanical one, resulting in the growth of the oxide layer. Therefore, the thickness of the oxide layer oscillates periodically around an equilibrium point kinetically. The electrochemical energy is a function of the thickness of the oxide layer. As a result, corresponding to different mechanical energy, the kinetic equilibrium points are different, inducing that the oxide thickness is different under various polishing conditions. This is the kinetics of the material removal in Ta ECMP.

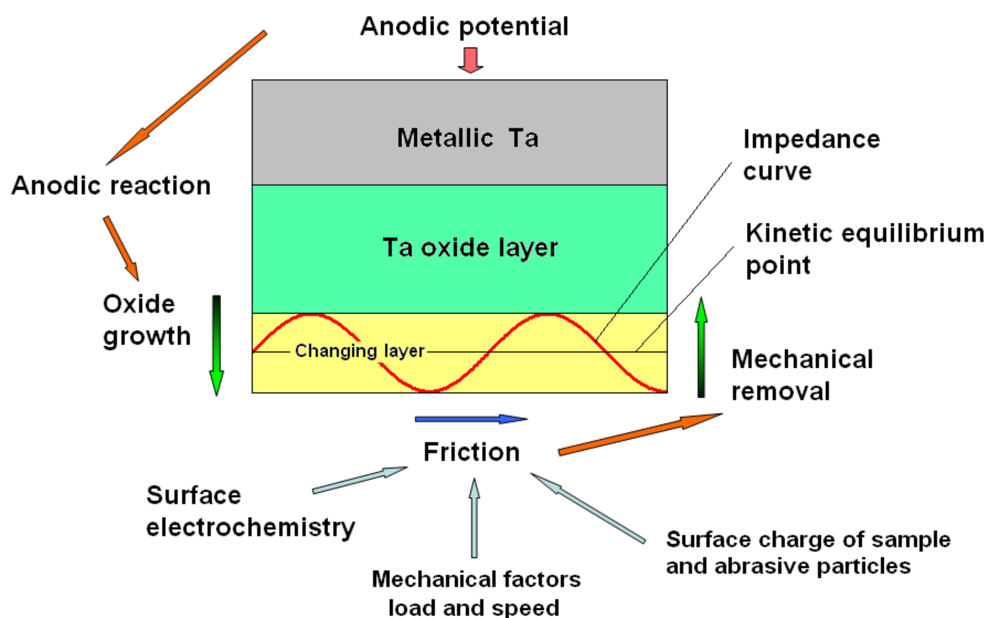

Figure 4. 17. The kinetics of the material removal in Ta ECMP.

4.4. Summary

In this chapter, using the experimental setup discussed in section 3.3.1, in situ observation of friction and corrosion was made possible with the applied electric potential. The tribological behaviors and material removal mechanisms in Ta ECMP were studied.

In section 4.1, electrochemical and tribological investigation of Ta ECMP was conducted. Potentiodynamic experiments showed that the corrosion current is a function of mechanical parameters such as the down force and the rotating speed while the load plays a more important role than the latter. In terms of passivation, the impedance measurements revealed that the polarization resistance R_p and the double layer

capacitance C_{dl} may refer to the formation of different Ta oxides on the surface generated under different polishing conditions. During ECMP, the friction coefficient is a function of five factors, cathodic reactions, mechanical abrasion, oxidation, anodic reactions, and the surface charge of sample and particles. These five competing factors dominate alternatively under different polishing conditions and electrical potentials. The final quality of ECMP depends on the kinetic balance of those factors.

In section 4.2, material removal mechanisms of Ta CMP and ECMP were investigated using the single frequency EIS. Single frequency EIS was found to be able to fulfill in situ observation in Ta CMP and ECMP by measuring the impedance of the sample. The impedance results revealed that there were two competing mechanisms in ECMP, the formation and removal of Ta oxide during polishing. The mechanical abrasion and electrochemical passivation dominate underwent synergetically reflecting the thickness/impendence change of the oxide. Our results indicated that the period of growing and removing the oxide film was a function of the mechanical power induced by the friction.

Although the material removal mechanism has been revealed using the single frequency EIS, it is within the macroscopic scale. It was proposed that the material removal occurs in a molecular scale.[19] As such, more work is needed to investigate the material removal mechanism of Ta ECMP in the nanometer length scale. It was found in the present chapter that the material removal rate is a function of the mechanical energy. To date, the in situ removal rate has not been able to be quantified. The potentiostatic EIS results showed that the compositions of the oxide layer generated under different

polishing conditions are different. Nevertheless, the details have not been reported. Therefore, in order to understand the Ta ECMP process more clearly, it is necessary to conduct detailed investigations.

CHAPTER V

IN SITU OXIDATION PROCESSES AND MECHANISMS

In Chapter IV, the tribological and material removal mechanisms were investigated. The competition of the Ta oxidation and the mechanical abrasion contributes to the material removal. The mechanical energy due to friction at the sample-pad interface is responsible for the removal of Ta oxide layer. Using the single frequency EIS, the periods of the impedance curves obtained under different polishing conditions reflected the material removal rate qualitatively. However, the single frequency EIS could not quantify the material removal during ECMP. The applied anodic potential is in charge of forming the Ta oxide layer. The results of the potentiostatic EIS tests showed that different Ta oxides existed in the oxide layer when polished various mechanical forces. Nevertheless, this technique could not reveal what types of Ta oxides were generated. In addition, although the kinetics of the Ta oxidation in oxygen has been observed[69], such has not been studied during ECMP. The oxidation process is important for understanding and optimizing the ECMP process.

In order to answer the questions raised above, experiments were conducted by using the experimental setup discussed in section 3.3.1 and AFM. This chapter discusses the quantification of the material removal and the oxidation kinetics in ECMP process based on the experimental results.

5.1. Preston Equation in Tantalum ECMP

As reviewed in Chapter I, the Preston equation has been accepted to describe the material removal in polishing. The Preston equation, however, has not been accepted in Ta ECMP. This section discusses the modified Preston equation of Ta ECMP. The testing conditions were described in section 3.6.3. AFM was used to measure the material removal rate, following this approach delineated in section 3.5.5. The material removal measured by using AFM showed the real quantities of the Ta oxides removed from the surface.

As shown in Eq. 1.2, the Preston equation depicts the correlation of the material removal rate and the mechanical abrasion. The product PV of the down force P and moving speed V of the sample represents the mechanical force which is responsible for the material removal. The higher the PV numbers, the more the mechanical removal. The PV numbers are used in this section to describe the mechanical reactions, following the conventions.

Fig. 5.1 shows the material removal rate (MRR) vs. PV numbers at the constant potential of 1 V vs. SCE. The X-axis is the PV number with the unit of Nm/s, which was calculated from Table 3.3 by multiplying the load and speed in each polishing condition. The Y-axis is the MRR measured using AFM in unit of nm/min. The line in Fig. 5.1 is the linear fit of all data points.

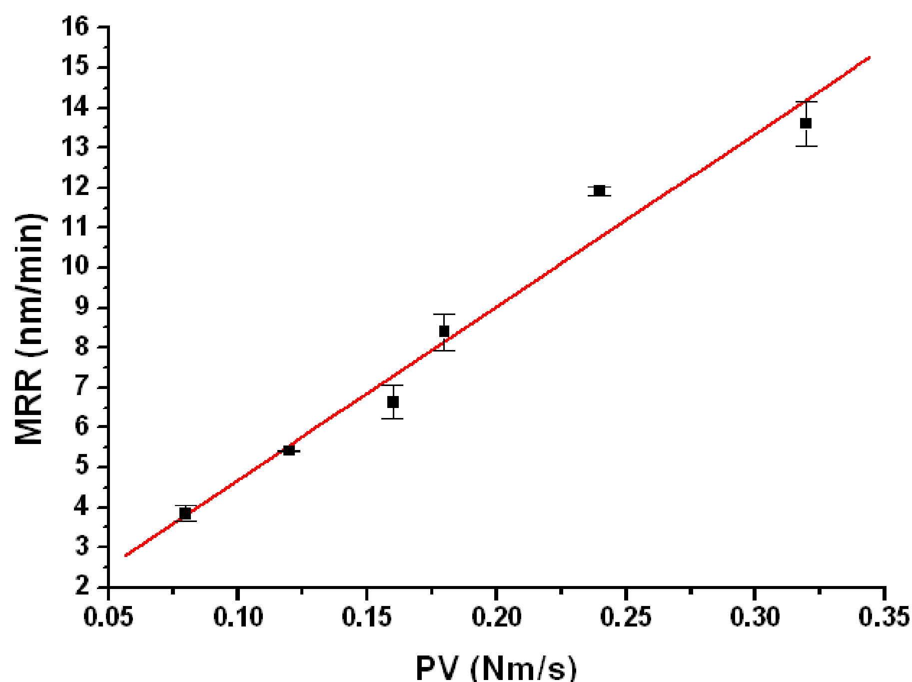

Figure 5. 1. The MRR measured by using AFM vs. PV numbers. The potential applied on the sample was 1 V vs. SCE. The line is the linear fit of data points.

Using the Preston equation (Eq. 1.2), the constant k can be calculated based on Fig. 5.1, which is 7.23×10^{-10} N^{-1}. The relationship between the MRR and PV under the current polishing conditions can be expressed as

$$MRR = 7.23\times10^{-10} PV \quad [5.1]$$

In copper ECMP, the copper removal rate is determined by the applied potential rather than the down pressure (<2.07 kPa).[35, 45] On the contrary, our results showed the dependence of the MRR on the mechanical force. The difference lies in the nature of the materials. Copper oxides generated by the applied potential can be dissolved by the chemicals in the electrolyte[45], while Ta oxides are inert to most commonly used

chemicals. In copper ECMP, the removal rate is independent of the down pressure.[35] That means that the copper ECMP is a chemical-dissolution-dominated process. On the contrary, the Ta ECMP is toward a mechanical-removal-dominated process.

In Eq. 5.1, the Preston constant k was determined under the current polishing conditions, i.e., the composition of the slurry and the constant potential of 1 V. The Preston constant is affected by the polishing system, including the slurry, polishing machine, polishing pad, and so on. Consequently, the Preston constant varies when different potentials and slurries are applied.

Differently from CMP, a potential is applied on the metal in ECMP. The applied potential is a driving force for the metal oxidation. As a result, the effects of the potential should be involved in the Preston equation to describe the removal process. The experiments were conducted with a varying potential at the constant load (2 N) and speed (0.08 m/s). Fig. 5.2 shows the MRR vs. potential at 2 N and 0.08 m/s. The X-axis is the potential vs. SCE, while the Y-axis the material removal rate. The MRR decreases with the increase of the applied potential when the potential is lower than 0.75 V, followed by an increase after 0.75 V. The curve of the MRR is similar to a second order polynomial fit with the minimum apex of 6 nm/min between 0 V and 1.5 V. After 1.5 V, the increase of the MRR follows a logarithmic function approximately.

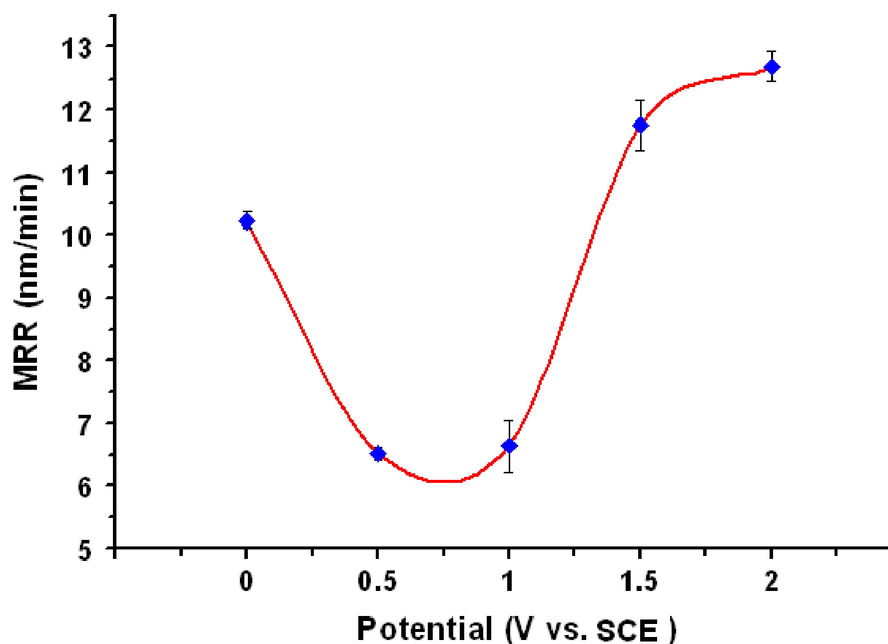

Figure 5. 2. The MRR vs. potential. The load and speed are 2 N and 0.08 m/min respectively.

It was reported that the MRR increases with an increased anodic potential in copper ECMP[47] and Ta ECMP[62]. However, our results do not agree with those published data. In Fig. 5.2, there is a transition at 0.75 V. After this point, the higher the potential, the higher the MRR. The inconsistency may be due to the range of the applied potential. According to the data shown in Fig. 5.2, at PV=0.16 Nm/s, the relation between the MRR and the applied anodic potential can be expressed by Eq. 5.2.

$$MRR = aE^2 + bE + c\,;\; 0 < E < 1.5$$

$$MRR = d\log E + e\,;\; 1.5 < E \qquad [5.2]$$

where E is the applied anodic potential; a, b, c, d, and e are constant. Eq. 5.2 was obtained at a specific PV number, while Eq. 5.1 was achieved at a constant potential.

From these two equations, it can be seen that both the mechanical abrasion and anodic potential significantly influence the MRR. Combining Eq. 5.1 and 5.2, Eq. 5.3 was developed as a modified Preston equation in Ta ECMP.

$$MRR = k \cdot MRR(E) \cdot PV \qquad [5.3]$$

where *k* is the Preston equation; *MRR(E)* is the function of the potential at a constant PV number. Fig. 5.3 was plotted based on Eq. 5.3. It can be seen that at a constant potential, the MRR shifts to a higher value with the increase of the PV number. When the PV number is fixed, the MRR follows the trend as shown in Fig. 5.2. The shapes of the curves of the MRR vs. potential at different PV numbers may vary. They can be determined by calculating the constants in Eq. 5.2 and the Preston constant in Eq. 5.3. Because the potential affects the formation of the oxide layer greatly due to the electrochemistry, the Preston constant *k* at a constant potential in Eq. 5.1 may change, i.e. the slope of the curve shown in Fig. 5.1. In order to determine the Preston equation, more experiments are needed to find out the MRRs at different potentials and PV numbers. The Eq. 5.1, 5.2, and 5.3 qualitatively describe the material removal process in the Ta ECMP.

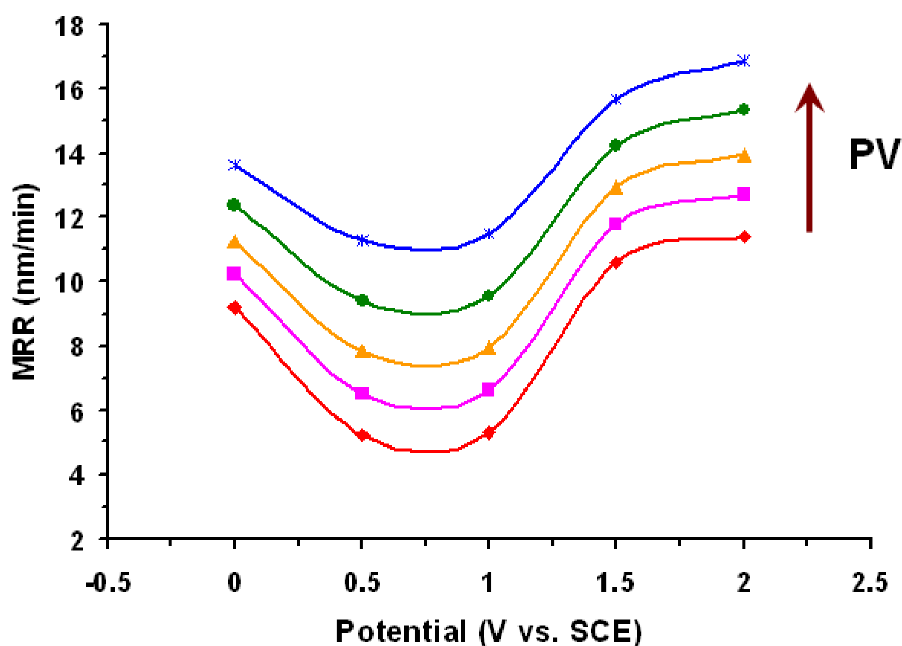

Figure 5. 3. The MRR under different potential and PV numbers. It qualitatively shows the Preston equation in Ta ECMP.

5.2. Oxidation Kinetics of Polycrystalline Tantalum during ECMP

The last section reveals the relationship between the MRR and the mechanical abrasion. In ECMP, the oxidation of the metal triggered by the applied anodic potential is as important as the mechanical abrasion, as pointed out in section 4.2. Understanding the oxidation kinetics during ECMP is crucial to optimize the process. This section discusses the oxidation kinetics of poly crystalline Ta during ECMP.

In the previous section, discussion was provided in using AFM to measure the actual MRR after each polishing experiment. Alternative approach to calculate the MRRs is to use Faraday's law which describes the relationship between the weight of

the oxidized metal and electrons released by the metal. In each test conducted in section 5.1, the electrochemical reaction current was measured using the potentiostat. This current is the net current of the anodic (oxidation) and cathodic (reduction) reactions (Eq. 5.4). In section 4.1, we found that the open circuit potential (OCP) of Ta is about -0.45 V under the similar polishing conditions. The current is stable when the potential is higher than 0 V, showing the anodic reactions are dominant. The cathodic current can be negligible compared with the anodic one. The net current is equal to the anodic current approximately.

$$I_{net} = |I_{anodic}| - |I_{cathodic}| \approx |I_{anodic}| \qquad [5.4]$$

where I_{net} is the net current; $|I_{anodic}|$ is the absolute value of the anodic current; $|I_{cathodic}|$ is the absolute value of the cathodic current. Eq. 5.5 shows the Faraday's law.

$$W = \frac{MQ}{nqN_0} \qquad [5.5]$$

where W is the weight of the oxidized metal (g); Q is the quantity of the corresponding released electrons due to oxidation (C); M is the molar mass of the metal (180.95 g/mol); n is the valence of the oxidized atoms; q is the elementary charge (1.602×10^{-19} C); N_0 is Avogadro's number (6.023×10^{23} mol^{-1}). In Ta ECMP, the Ta atoms are oxidized and subsequently removed by the mechanical force. The quantity of the oxidized tantalum equals the material removed during polishing. Hence, the Ta removal rate with polishing can be expressed by Eq. 5.6.

$$MRR = \frac{MQ}{n\rho qN_0 At} \qquad [5.6]$$

where *MRR* is the material removal rate (nm/min); ρ is the density of Ta (16.69 g/cm^3); A is the sample area (0.317 cm^2); t is the polishing time (min). The Ta removal rate can be calculated by inputting all known constants into Eq. 5.6 (Eq. 5.7).

$$MRR = \frac{3.55 \times 10^3 Q}{nt} \text{ (nm/min)} \quad [5.7]$$

The quantity of the electrons can be calculated by multiplying the average anodic current with the total polishing time T (s) through Eq. 5.8.

$$Q = TI_{anodic} \quad [5.8]$$

By inserting Eq. 5.8 into Eq. 5.7, Eq. 5.9 can be achieved.

$$MRR = \frac{59.17 \times I_{anodic}}{n} \quad [5.9]$$

In a certain period of polishing time, the MRR is determined by the anodic current I_{anodic} and the valence of metal atoms n. The current can be measured by the potentiostat, while the valence is unknown.

Ta is a transition metal and it usually has four positive valences during oxidation, from +2 to +5. If all Ta atoms are oxidized to Ta^{2+} during ECMP, the MRR can be calculated by Eq. 5.9 with n=2; if all tantalum atoms are oxidized to Ta^{5+}, the corresponding MRR should be 2/5 of the former one. This means that the MRR cannot be simply calculated from Eq. 5.9 when the oxidation state of tantalum is unknown.

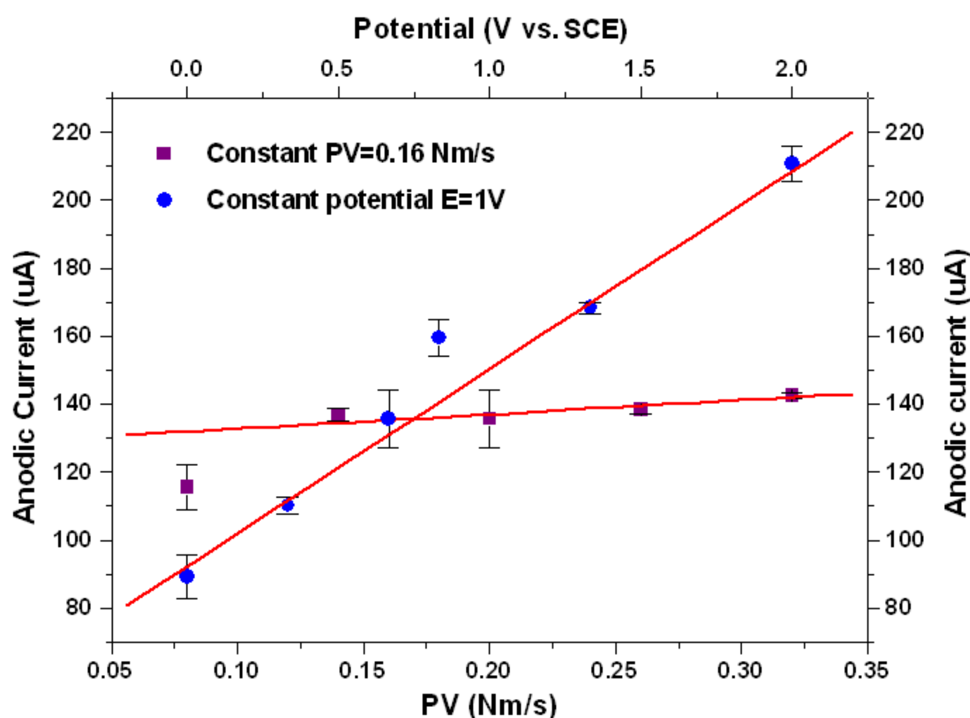

Figure 5. 4. The anodic current vs. PV and potential at a constant potential (1 V) and a constant PV=0.16 Nm/s.

Fig. 5.4 shows the anodic current vs. PV (right and bottom axes) and potential (left and top axes) at a constant potential of 1 V and at a constant PV=0.16 Nm/s respectively. The lines in Fig. 5.4 are linear fits of corresponding data points. The slope of the fit curve at the constant potential is much higher than that at the constant PV. In section 4.2.3, it was found using the single frequency EIS that the thickness of the tantalum oxide layer decreased as the mechanical force increased. The higher the PV numbers, the thinner the oxide layer. The anodic current decreased exponentially with the increase in thickness of the oxide layer at a fixed potential due to the resistance to the further oxidation of tantalum from the thick oxide layer.[89] In such, the anodic current

inclines at the constant potential as the PV number increases. As discussed in section 4.1.1, when the anodic potential was higher than 0 V, the anodic current was independent of the potential due to the passivation. In Fig. 5.4, the anodic current obtained at a constant PV and different potentials did not show visual change. This agrees with the previous results.

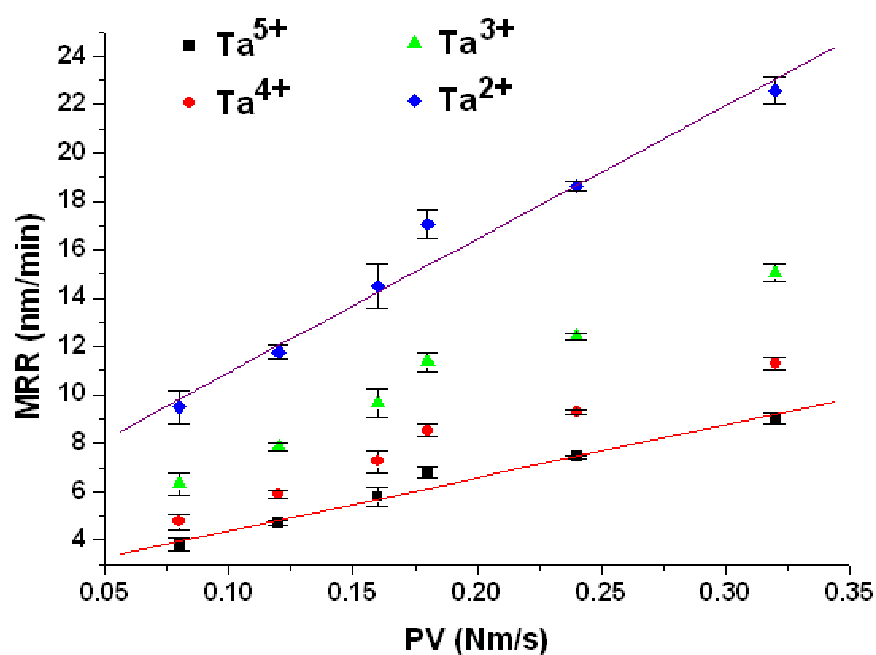

(a) The calculated MRRs at the constant potential (1 V) and different PV numbers.

Figure 5. 5. The calculated MRRs by inserting the anodic current and different valences into the Faraday's law.

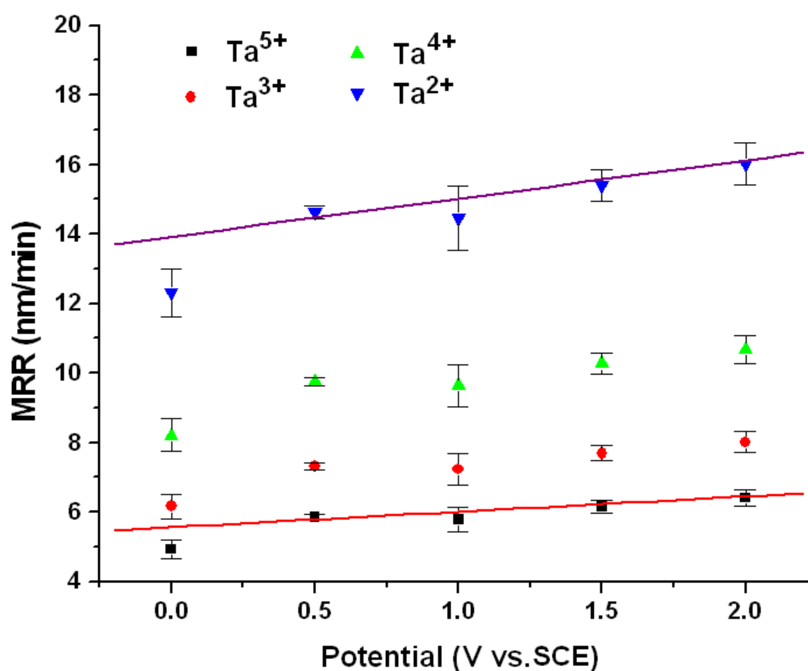

(b) The calculated MRRs at the constant PV (0.16 Nm/s) and different potentials.

Figure 5. 5. Continued.

The Ta removal rate can be calculated by inserting the anodic current and different valences into Eq. 5.9. Fig. 5.5(a) shows the calculated MRRs at the constant potential and different PV numbers, while Fig. 5.5(b) at the constant PV and different potentials. It can be seen in both diagrams that the highest MRR was obtained when Ta had the lowest valence. On the contrary, the lowest MRR occurred as Ta held the highest valence. Since the MRR is proportional to the anodic current (Eq. 5.9) and the current is linear to the PV numbers at the constant potential and the potentials at the constant PV (Fig. 5.4), the MRR is linear to the PV numbers and the potentials respectively. The slope of each linear fit increases with the decline of the Ta valence.

According to Faraday's law, the MRR is determined by the valence *n* when the anodic current is known. In copper ECMP, the MRR can be calculated from the current through Faraday's law due to the fact that all copper atoms can be dissolved to Cu^{2+}.[35, 45] Ta is different from copper because of its multiple valences. Fig. 5.5 shows this valence effect on the MRR calculated through Eq. 5.9. In Fig. 5.5(a), at each PV number, the lowest MRR was obtained by assuming that all the tantalum oxide removed the mechanical force during polishing were oxidized to Ta^{5+}, while the highest one corresponded to Ta^{2+}. The situation is the same in Fig. 5.5(b) except at different potentials. Different valences correspond to different MRRs. As discussed in the last section, AFM can be used to measure the actual MRRs.

In order to know the oxidation state of Ta during polishing, the measured MRRs and calculated ones were compared through combining Fig. 5.1 and Fig. 5.5(a), and Fig 5.3 and Fig 5.5(b) respectively. Fig 5.6 shows the comparison. Since the error bars of the calculated MRRs have been shown in Fig 5.5, they were not shown in Fig. 5.6 to make it clearer. At the constant potential (Fig. 5.6(a)), the actual MRR is also a linear function of the PV numbers, while its slope is higher than that of the linear fit of the calculated MRR. At the lowest PV number (0.08 Nm/s), the actual MRR is equal to the calculated one as the valence of tantalum is assumed 5. With the increase of the PV, the measured MRR approaches the calculated MRR with the valence of 4 gradually. When the *PV* number is higher than 0.18 Nm/s, the actual MRR is higher than the calculated MRR with valence of 4, but lower than that with valence of 3. At the constant PV (Fig. 5.6(b)), the actual MRR is at the middle of the calculated ones with the valences of 2 and 3 at 0

V. As the potential increases, the actual MRR is close to the calculated one with the valence of 5. When the potential is higher than 1.5 V, the actual MRR is higher than the calculated MRR with the valence of 3, but lower than that of 2.

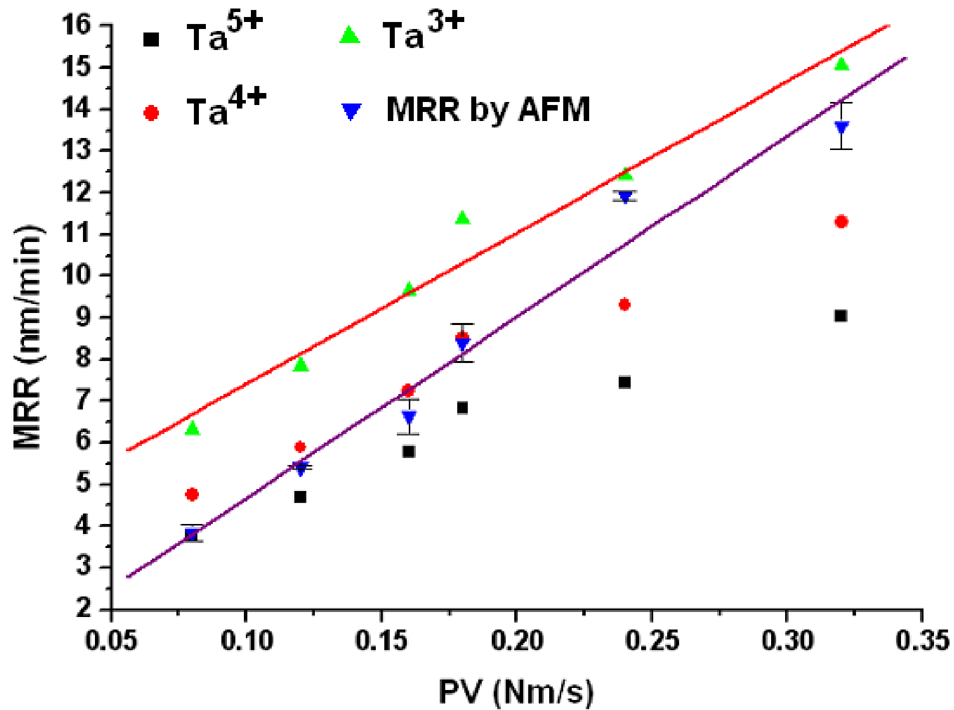

(a) At the constant potential of 1 V.

Figure 5. 6. The comparison of the calculated MRR and the measured MRR by using AFM. The error bars of the calculated MRR are not shown for a clearer view.

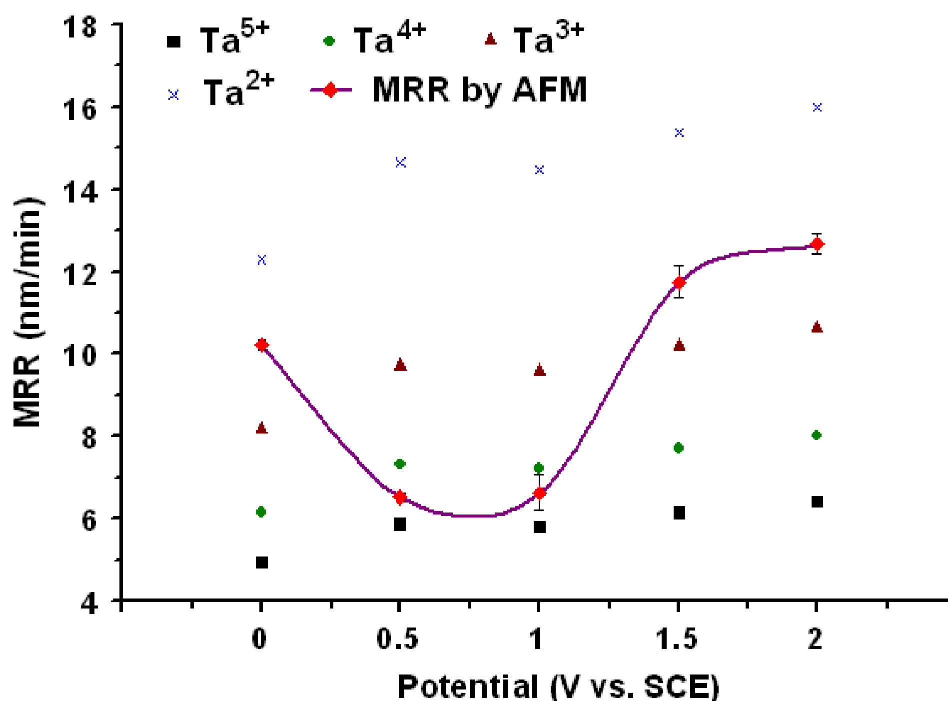

(b) At the constant PV=0.16 Nm/s.

Figure 5. 6. Continued.

Comparing the calculated MRRs through Faraday's law and the actual MRRs measured by AFM (Fig. 5.6), the oxidation state of Ta during ECMP can be identified. The calculated MRRs were achieved by assuming that all removed material was one specific tantalum oxide. In fact, the Ta oxide layer during ECMP is composed of different types of oxides, including pentoxide and suboxides.[78] The actual MRRs cannot be obtained via Faraday's law. The material removal measured by AFM is indeed the actual material loss of the polishing sample. At the lowest PV value (0.08 Nm/s) in Fig. 5.6(a), the actual MRR is equal to the calculated one when assuming that the valence of Ta is 5, demonstrating that the removal material is Ta pentoxide (Ta_2O_5). With the

increase of the PV number, the actual MRR moves toward the calculated one with lower valence from that with higher valence. The actual MRR does not equal to the calculated MRR with the valence of 5 any more, but between the ones with two adjacent valences. This indicates that the removal is no longer only Ta pentoxide, but the mixture of tantalum oxides. The similar analysis can be done for the case at the constant PV (Fig. 5.6(b)).

In order to quantify the oxidation state of Ta conveniently, we introduce the concept of "average valence" of Ta. The calculation of the average valence is shown in Eq. 5.10.

$$n_{avg} = n_{high} - \frac{MRR_{actual} - MRR_{n=high}}{MRR_{n=low} - MRR_{n=high}} \quad [5.10]$$

where n_{avg} is the average valence of Ta; n_{high} is the valence just higher than the average valence; MRR_{actual} is the actual MRR; $MRR_{n=high}$ is the calculated MRR with valence of n_{high}; $MRR_{n=low}$ is the calculated MRR with the valence just lower than the average valence. For example, in Fig. 5.6(a), at PV=0.12 Nm/s, the actual MRR is between the calculated MRRs with the valences of 4 and 5 respectively. The average valence at this PV number can be calculated in Eq. 5.11, which is 4.40:

$$n_{avg} = n_{high} - \frac{MRR_{actual} - MRR_{n=high}}{MRR_{n=low} - MRR_{n=high}} = 5 - \frac{5.42 - 4.71}{5.85 - 4.71} = 4.40 \quad [5.11]$$

Through this method, all average valences at different PV numbers were calculated and shown in Fig. 5.7. The average valence decreases as the PV number increases. The average valence cannot tell the exact composition of the Ta oxides, while it can tell the

ratios of different oxides qualitatively. The oxide layer is a mixture of different oxides.[78] When the average valence is high, the oxides in which Ta has high valences appear. On the contrary, when the average valence is low, more types of suboxides coexist.

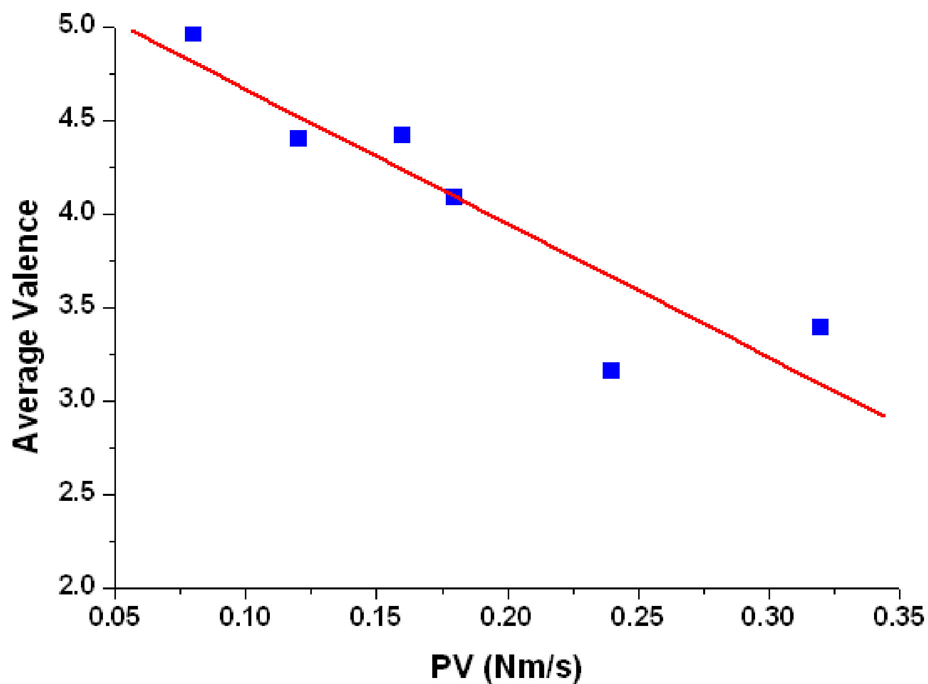

(a) At the constant potential of 1 V.

Figure 5. 7. The average valences at the constant potential and constant PV.

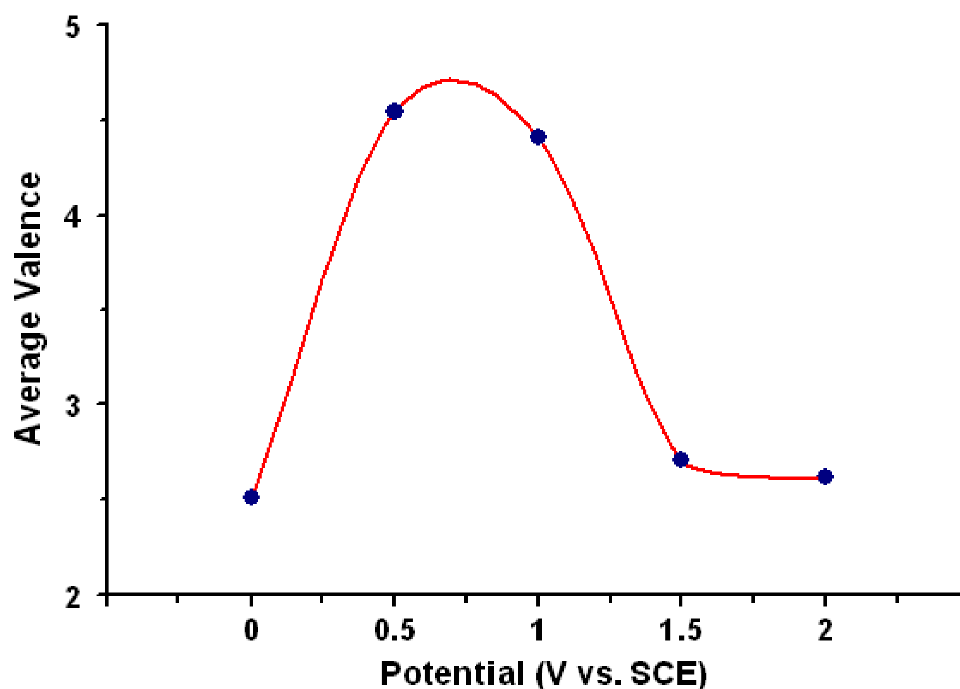

(b) At the constant PV=0.16 Nm/s.

Figure 5. 7. Continued.

As discussed in section 4.2, the impedance which represents the Ta oxide thickness is constant during ECMP, except a small periodic variation which shows the material removal mechanism. That means that the oxidation process of Ta is at an equilibrium state, i.e. the properties of the oxide layer do not change. Otherwise, the impedance will change. The ECMP is a kinetic process. Therefore, the oxidation process during ECMP is kinetically balanced. In Fig. 5.7, the trends of the average valence are quite different in these two scenarios, at the constant potential and constant PV respectively. The oxidation processes in these two cases may be different. We will discuss them individually.

At the constant potential, the average valence declines as the PV number increases (Fig. 5.7(a)). The PV number represents the mechanical removal. The relationship between the mechanical force and the thickness of the oxide layer has been proven in section 4.2 by using the impedance measurement. At a low PV value, the oxide layer is expected to be thick. Only little Ta oxides are removed from the surface, resulting in that the time is sufficient to oxidize Ta atoms to become pentoxide by the potential. In other words, the Ta atoms have been oxidized to pentoxide before the oxide is removed by the mechanical sweeping. At a higher PV value, the oxide layer is thinner and more Ta oxides are removed. The Ta oxides have already been removed before the Ta atoms are oxidized to a higher valence. Fig. 5.8 shows the structure of the Ta oxide layer and removal process of Ta at the constant potential during polishing. In the Ta oxide layer, there are more suboxides existing in the region closer to the metallic Ta, while more pentoxide forms near the surface of the oxide layer. With lower mechanical removal, only a little material is removed, resulting in higher average valences. The appearance of lower average valences is due to the higher mechanical removal. Furthermore, from this model and experimental results, the natural oxidation process (no mechanical abrasion) of Ta can be deduced. There are two steps in the Ta oxidation. First, the Ta atoms are oxidized to suboxides. Then the suboxides are further oxidized to the pentoxide. The valence of Ta becomes higher and higher in the oxidation process. This is a transition process.

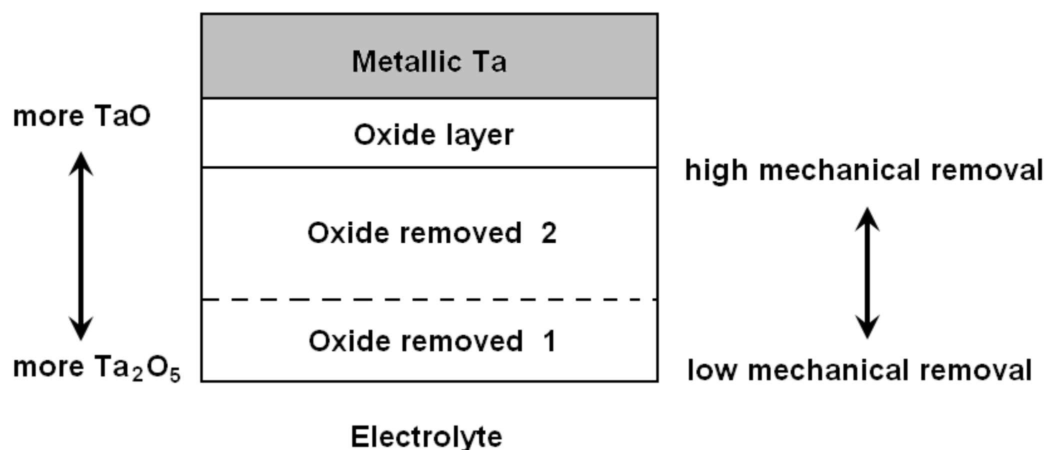

Figure 5. 8. The oxidation and removal processes at the constant potential during Ta ECMP.

From Fig. 5.7(b), at the constant PV, the average valence increases with the increased potential until the potential reaches about 0.75 V, followed by a decrease. This demonstrates that more suboxides exist on the surface when the potential is either very low or very high, while more pentoxide appears as the potential is mediate. The formation of the Ta oxides is resulted from the reactions between the Ta atoms and oxygen which diffuses into the metal interstitially. The anodic potential is the driving force to impose the oxygen into the substrate. The higher the potential, the higher the driving force. It has been verified in section 4.2 that a higher potential results in a thicker oxide film. The oxide layer as a barrier retards the diffusion of the oxygen. Therefore, the potential and the oxide layer influence the oxidation process simultaneously. Fig. 5.9 illustrates this oxidation and removal process. The numbers in the figure are the average valences of the removed oxide. The bottom rectangle of each individual figure shows the

removal rate in each case, agreeing with the results shown in Fig. 5.2. As shown in Fig. 5.8, the Ta atoms have lower valences at the metal-oxide interface than on the top surface. At the lowest potential, the oxide layer is the thinnest. It is easier for the oxygen to penetrate the oxide layer and then react with the metallic Ta atoms or those with lower valences, even though the driving force (potential) is relatively low. At this moment, the potential dominates the oxidation process. When the potential is higher (0.5 V), the oxide layer is thicker. The oxygen cannot reach the metallic Ta atoms due to the retard of the thick oxide film, although the driving force is higher. The oxygen prefers to react with the Ta atoms on the top surface, generating more pentoxide. The oxidation process is dominated by the oxide film. When the potential keeps increasing (> 1 V), the thickness of the oxide layer becomes higher as well as the driving force. The contribution of the increasing driving force to the oxygen penetration is larger than the retard from the oxide layer. The potential is more and more dominant in the oxidation process and thus more suboxides appears on the surface. In such, the oxidation process at a constant PV is a function of the potential and the thickness of the oxide layer. Eq. 5.12 shows this function.

$$\Gamma = k \cdot \Gamma(E, \delta, PV) \qquad [5.12]$$

where Γ is the oxidation process and it could be the ratio of the pentoxide in the oxide layer; *k* is the constant related to the polishing system; E is the applied potential; δ is the thickness of the oxide layer; *PV* represents the mechanical abrasion. In order to obtain the specific equation for the oxidation process, the thickness must be known. Additionally, more experiments are needed at different PV numbers.

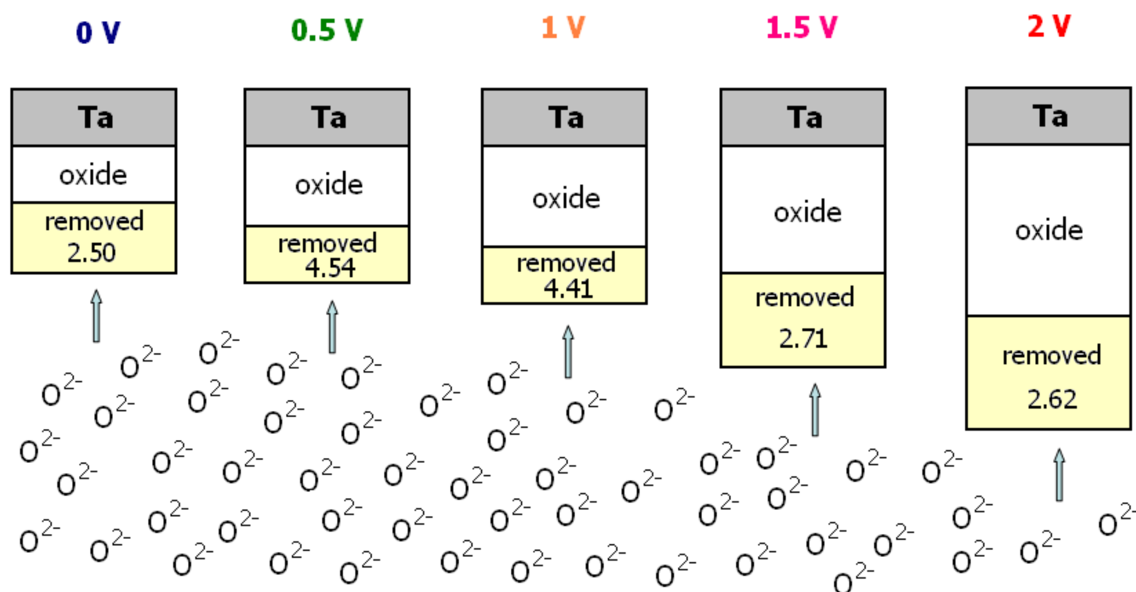

Figure 5. 9. The oxidation and removal processes at the constant PV during Ta ECMP.

According to this model, it seems that the transition from the metallic Ta to suboxides is preferred than that from the suboxides to the pentoxide. In other words, lower activation energy is required to oxidize metallic Ta atoms to the suboxides than the suboxides to the pentoxide. Based on XPS results of the Ta oxides, the pentoxide has higher binding energy than the suboxides.[76, 94] This probably can explain the phenomena occurring in the oxidation process.

In Fig. 5.2, higher MRRs occur at the extreme potentials (low and high) rather than at the mediate. Comparing with Fig. 5.9, it seems that the oxide in which the Ta atoms have lower valences is easier to be removed than that in which more pentoxide exists. This can also be explained by the binding energy of the suboxides and pentoxide.

The binding energy represents the interaction between the Ta atoms and oxygen atoms. Higher binding energy means tighter interaction. Ta and oxygen in the pentoxide interact more tightly than in the suboxides. As a result, the suboxides are easier to be removed. In order to obtain a high material removal rate, a high potential is preferred. Additionally, the mechanical properties of the Ta suboxides, like yield strength, have not been found because the suboxides cannot exist in the nature stably and permanently. This technique used in the current study provides an approach to estimate the mechanical properties of the Ta suboxides.

As shown in Fig. 4.13 (section 4.2.3), the impedance curves obtained at different potential, 0 V, 1 V, and 2 V respectively, have the similar periods. That means that the growth rates of the oxide layer during the polishing are quite close. During ECMP, the oxide growth and the mechanical removal are the kinetic equilibrium state. Therefore, the removal rates at these potentials should be similar. However, from Fig. 5.2, the MRRs at these three potentials are very different. It seems that the two groups of results are contradictory, in fact the opposite. Let us take the bulldozer as the example again. The impedance can reflect how fast one plough is. But, it cannot show how deep one plough is. Assume that the thickness of the oxide layer removed in one plough at 0 V, 1 V, and 2 V is R_0, R_1, and R_2 respectively. According to Fig. 5.2, $R_2 > R_0 > R_1$. The oxide growth rate is a function of the potential and thickness of the oxide layer. At these potentials, assume the oxide growth rates are V_0, V_1, and V_2. The growth rate at 0 V should be lower than that at 1 V due to the lower driving force. However, the thicker oxide film obtained at 1 V counteracts the effect of the potential, resulting in even lower

growth rate. At 2 V, the potential is higher enough to suppress the effect of the oxide thickness, leading to a higher growth rate. As discussed previously, the effect of the potential on the oxidation process is dominant at the low and higher potential range, while the oxide thickness is dominant at the mediate potential range. To sum up, the periods of the oxide growth (Fig. 4.13) in different potentials, R_0/V_0, R_1/V_1, and R_2/V_2, may be identical.

In this section, the technique of comparing the actual MRR and the calculated MRR provides an approach to investigate the oxidation state and process of Ta during ECMP.

5.3. Oxidation Kinetics of Single Crystalline Tantalum during ECMP

The last section discusses the oxidation kinetics of the polycrystalline Ta during ECMP. A single crystalline metal has higher electrical conductivity than the poly crystalline one due to fewer grain boundaries. The single crystalline Ta may be used in future to improve the performance of ICs. In addition, in IC fabrication, Ta is deposited using physical vapor deposition (PVD). The deposited film is polycrystalline. Different grains have different surface orientations. In an ideal case, all grains should have the same material removal rate to avoid the selective polishing. It is necessary to investigate the performance of the single crystalline Ta during ECMP. This section discusses the material removal and oxidation kinetics of the single crystalline Ta. The experimental details can be found in section 4.2.3. The same analytical technique, i.e., comparision the actual and calculated MRRs, is used.

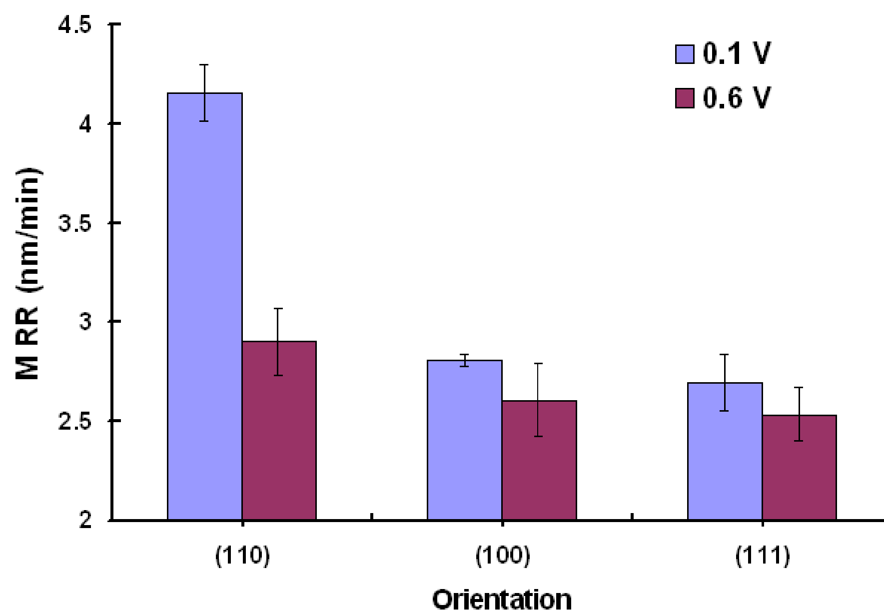

Figure 5. 10. The actual MRRs measured by using AFM vs. orientations. The load and speed are 1 N and 0.06 m/s respectively.

Fig. 5.10 shows the MRRs measured using the AFM at the same load and speed and different potentials. The MRRs for all orientations decreased as the potential increased. The results are consistent with those of the polycrystalline Ta (Fig. 5.2). This potential effect can be interpreted using the model shown in Fig. 5.9. At each potential, the highest MRR was obtained on the sample with the (110) orientation on the surface, while those on the other two samples with the (100) and (111) orientations were similar. The dissimilarity of the MRRs of (110) and (100) oriented samples is smaller at 0.6 V than at 0.1 V. As a result, a higher potential is preferred to ECMP a poly crystalline Ta film due to the better selectivity.

As introduced in the previous section, the average valences of the removed oxides on differently oriented samples were calculated through comparing the actual and calculated MRRs. Fig. 5.11 shows the results. For all orientations, the average valences at a higher potential are higher than those at a lower potential. This agrees the results illustrated in Fig. 5.7(b). At 0.1 V, the (110) sample has the lowest average valence, while the (100) the highest. At 0.6 V, the (100) sample still has the higher average valence, while the other two samples have the similar ones.

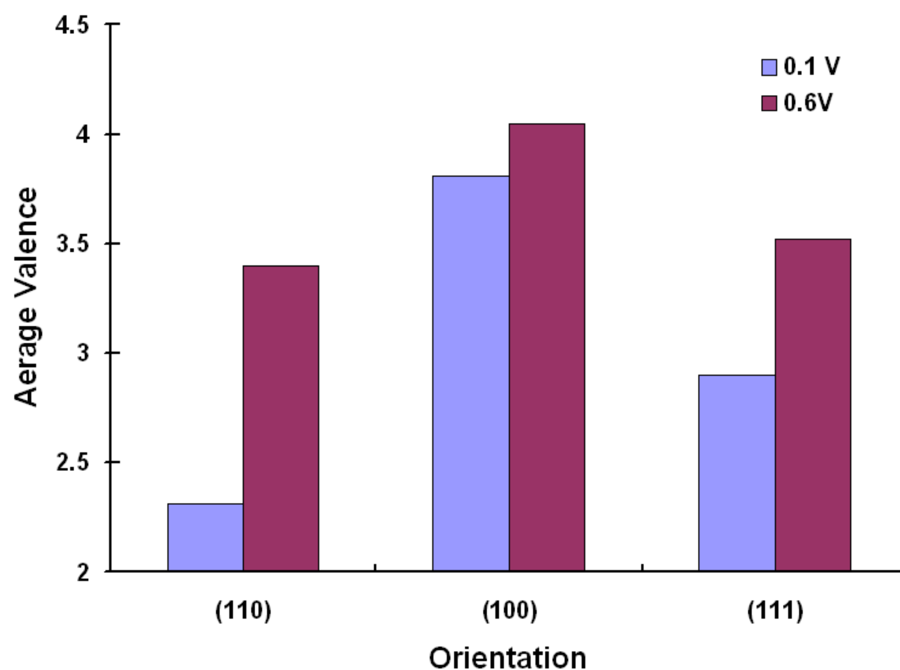

Figure 5. 11. The average valences of the removed oxides on different samples.

Stringer investigated the oxidation rates of Ta on different orientations in oxygen at a high temperature.[70] It was found that the oxidation rate on (110) plane is much

higher than that on (100) plane. Young et al. found that the growth rate of the copper oxide film is dependent on the surface orientation in oxygen at various temperatures.[94] In those studies, the thermal energy is the driving force of the oxidation. In ECMP, the potential is the driving force instead. These two cases are comparable. It can be said that the orientation affects the oxidation process of Ta in ECMP. In order to interpret the phenomenon shown in Fig. 5.11, a model was established (Fig. 5.12).

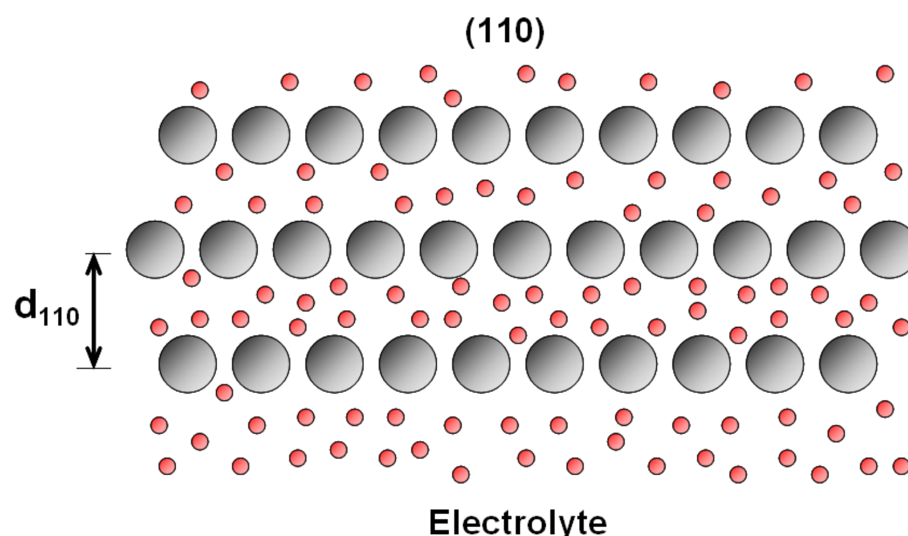

(a) (110) plane. The average valence is 3.40.

Figure 5. 12. The model of the oxidation process of the single crystalline Ta at 0.6 V. In each figure, the plane is normal to the paper. The bigger balls are Ta atoms, while the small ones are oxygen atoms. d_{110}, d_{100}, and d_{111} are the monolayer heights in each figure.

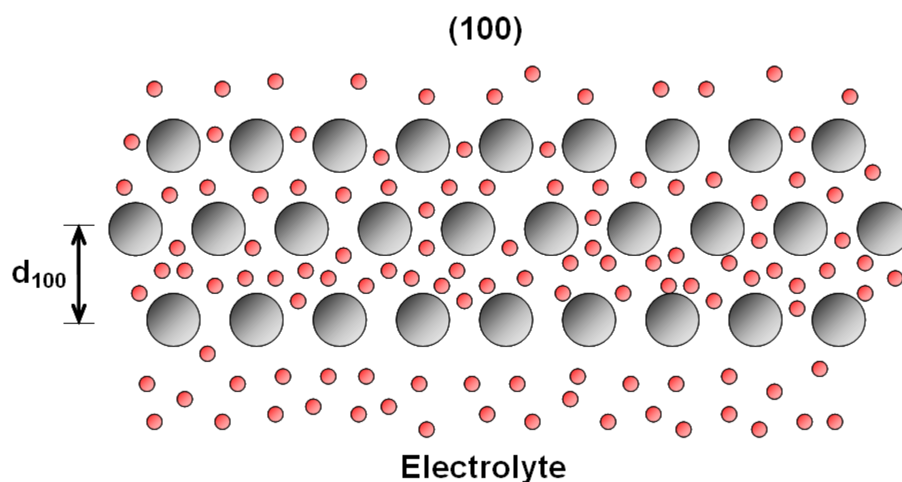

(b) (100) plane. The average valence is 4.05.

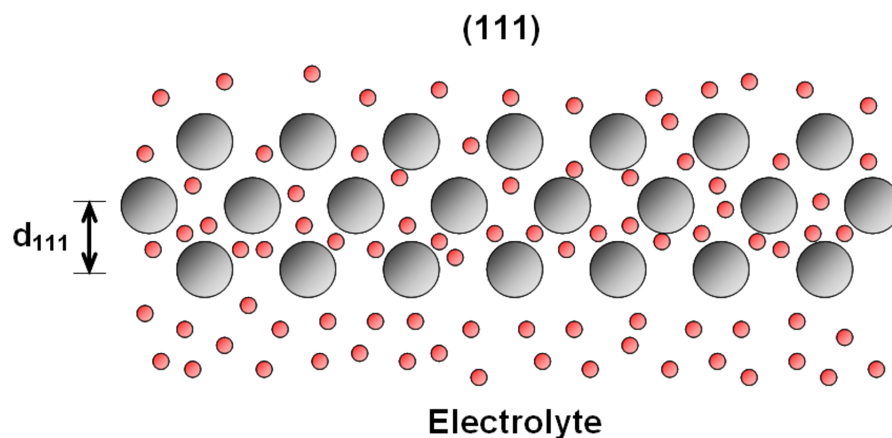

(c) (111) plane. The average valence is 3.51.

Figure 5. 12. Continued.

Fig. 5.12 shows the Ta atom arrangements of different planes, (110), (100), and (111) respectively. The planes are normal to the paper. The big balls represent Ta atoms, while the small ones oxygen. The Ta oxide film generated by the anodic potential is amorphous.[96] The oxygen atoms distribute in the Ta matrix randomly. Additionally, the deeper inside the metal, the fewer oxygen atoms. This model shows the case at 0.6 V.

The corresponding average valences of the removed oxides are listed. The packing fraction can reflect the density of atoms on an atomic plane. The packing fractions are 83.3 % for (110), 58.9 % for (100), and 34.0 % (111). The (110) is the most densely packed plane, while the (111) the least. In Fig. 5.12(a), the distance between two atoms in one row is smallest, while it is the biggest in Fig. 5.12(c). The monolayer height—the distance between two adjacent planes, was compared. Since the bulk density of Ta is the same for different samples, the sample having the highest packing fraction has the biggest monolayer height, i.e. $d_{110} > d_{100} > d_{111}$.

The oxygen atoms are driven into the Ta matrix by the applied potential to react with the Ta atoms, forming the oxides. The oxygen reacts with the Ta atoms on the surface first and then goes inside to react with more Ta atoms. The movement of the oxygen is retarded by the already formed oxide film. Comparing Fig. 5.12(a) and (b), the oxide film formed on the (110) oriented sample is denser than that on the (100) oriented due to the higher planar density (more atoms). More spacing is found in the (110) oriented sample because of the bigger monolayer height. The oxygen can diffuse further into the (110) oriented than in the (100) with the same driving force. As pointed out earlier, the formation of the pentoxide is preferable as the oxygen cannot penetrate the oxide layer. More suboxides form on the surface of the (110) sample, while more pentoxide on the (100). As a result, the average valence of the (110) is lower than that of the (100). In this case, the monolayer height dominates the oxidation process. Let us compare the (100) and (111) samples. The (111) oriented sample has smaller monolayer height. Nevertheless, its plane is more open than that of the (100). It is easier for the

oxygen to penetrate the looser oxide layer into the matrix. As a result, the (111) has more suboxides on the surface, resulting in a lower average valence. This process is dominated by the packing fraction.

It was found in the previous section that the suboxides were easier to be removed than the pentoxide. As shown in Fig. 5.10, the higher MRR could be seen on the (110) sample than that on the (100) due to more suboxides on the surface (lower average valence). Although the (100) has more pentoxide on the surface than the (111) does, the MRR of the former is close to the latter. This may be due to the smaller monolayer height of the (111). The interaction between two adjacent atomic planes in the (111) sample is higher than that in the (100) sample owing to the smaller distance between these two plane. The Ta oxides are sheared off by the friction force at the pad-sample interface, accomplishing the material removal. A stronger interaction between two atomic plane can cancel part of the shear force. This factor results in a lower MRR of the (111) than that of the (100), even if the former has a lower average valence.

It can be concluded from above analysis that the oxidation process of the single crystalline Ta is a function of the packing fraction and monolayer height. The orientation does influence the oxidation process during Ta ECMP.

5.4. Material Removal Mechanisms in Nano Meter Length Scale

Section 4.2 discussed the material removal mechanisms in Ta ECMP. The oxide growth and mechanical abrasion accomplish the material removal. The oxidation process of polycrytalline and single crystalline Ta during ECMP was discussed in section 5.2

and 5.3. Those studies are in the centimeter and millimeter length scale, relatively large. Chang proposed that the material removal occurs in the molecular scale in CMP.[19] This section discusses the oxidation process and material removal in nanometer length scale. The environmental cell and AFM were used. The experimental details can be found in section 3.6.5.

The environmental cell provided a wet condition. The AFM probe with a radius of 10 to 30 nm at the tip can be considered an abrasive particle. In the contact mode, the tip slides on the sample surface to measure the topography. These conditions could be used to simulate the polishing process. The AFM probe moves back and forth within one line. The length of the line depends on the scan sare. The moving speed of the probe was calculated based on the scan parameters. In the dynamic experiments, the scan area was 5×5 μm and the scan frequency was 0.7 Hz, resulting in the moving speed of 1.88×10^{-6} m/s. Using the same method, the moving speed of the probe in the kinetic experiments was 3.00×10^{-5} m/s. The latter was 16 times faster than the former. In section 5.1, it was proven that the material removal increased with the increase of the sample moving speed during polishing. The former did not contribute to the material removal as much as the latter due to the low speed. The sample scan in the dynamic experiments reflected the surface topography only.

Fig. 5.13 shows the AFM height images obtained in the dynamic experiments for the samples obtained under different orientations. It can be seen from the images that there are some small triangle features on the (110) and (111) oriented surfaces, while random-shaped islands distribute on the (100) surface. The triangle features were also

found on the (110) oriented surface of Ta after high temperature oxidation in an oxygen environment, while no such feature on the (100) surface.[70] The features on the surface are related to the surface orientations. In Fig. 5.13(a), the triangle islands were sharper after 2 min anodic oxidation, and even sharper after 4 min, showing the increase of the features in height. In Fig. 5.13(b), it seams that the more small clusters appeared after the anodic oxidation. The triangle features in Fig. 5.13(c) did not change a lot.

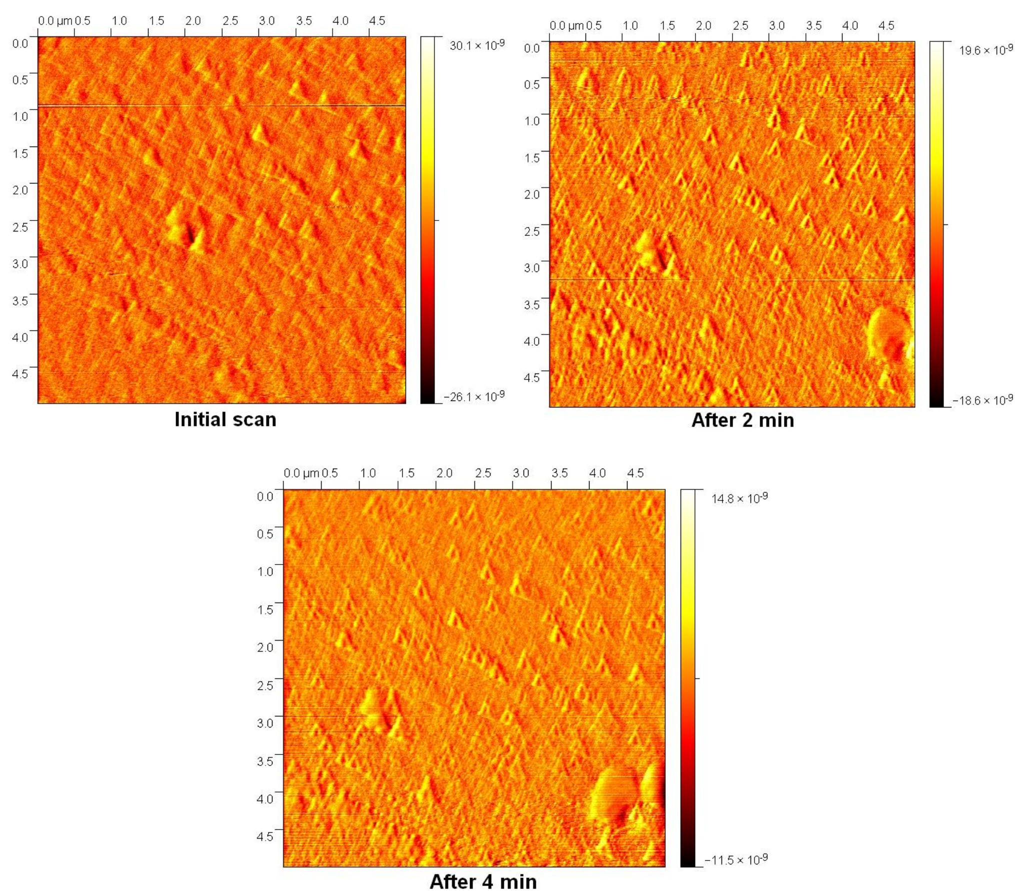

(a) (110).

Figure 5. 13. AFM height images obtained in the dynamic experiments on different oriented Ta surfaces.

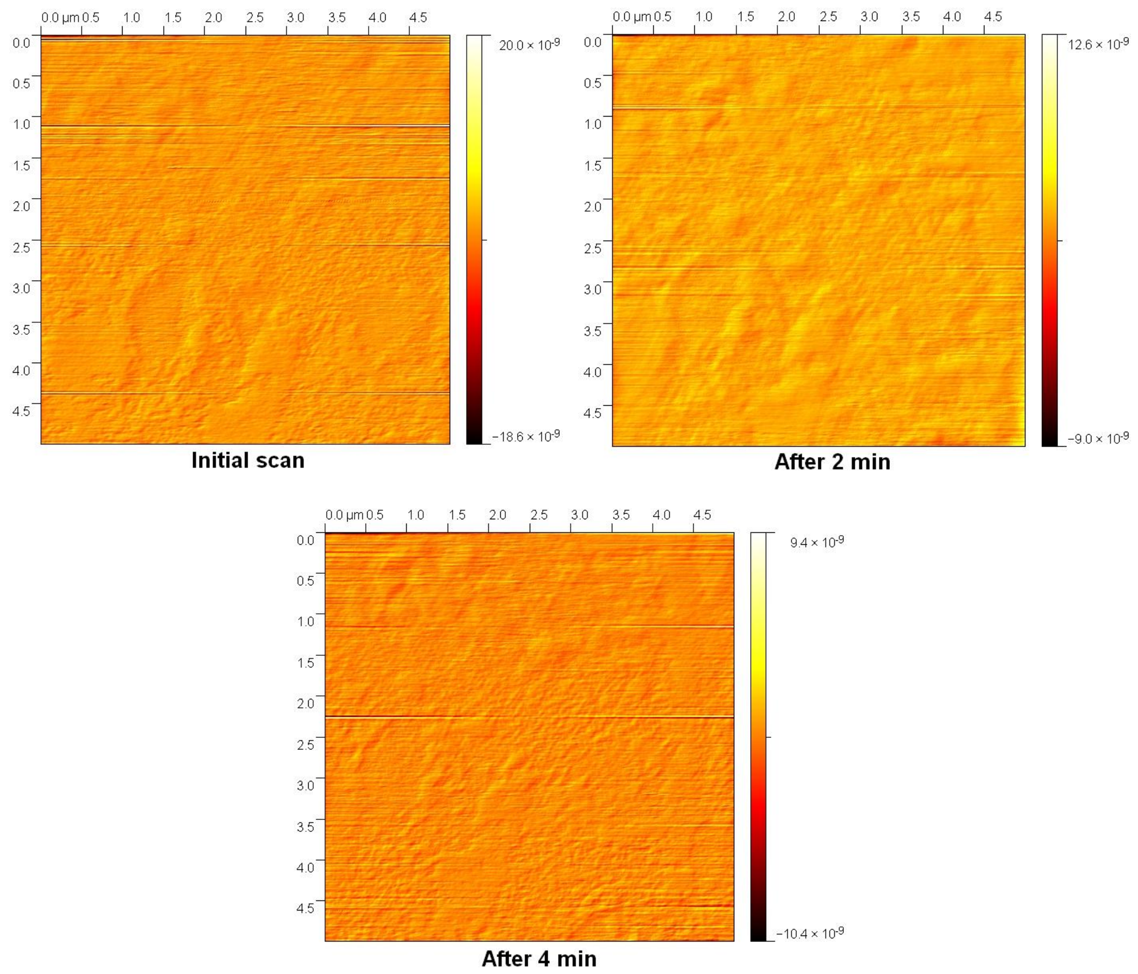

(b) (100).

Figure 5. 13. Continued.

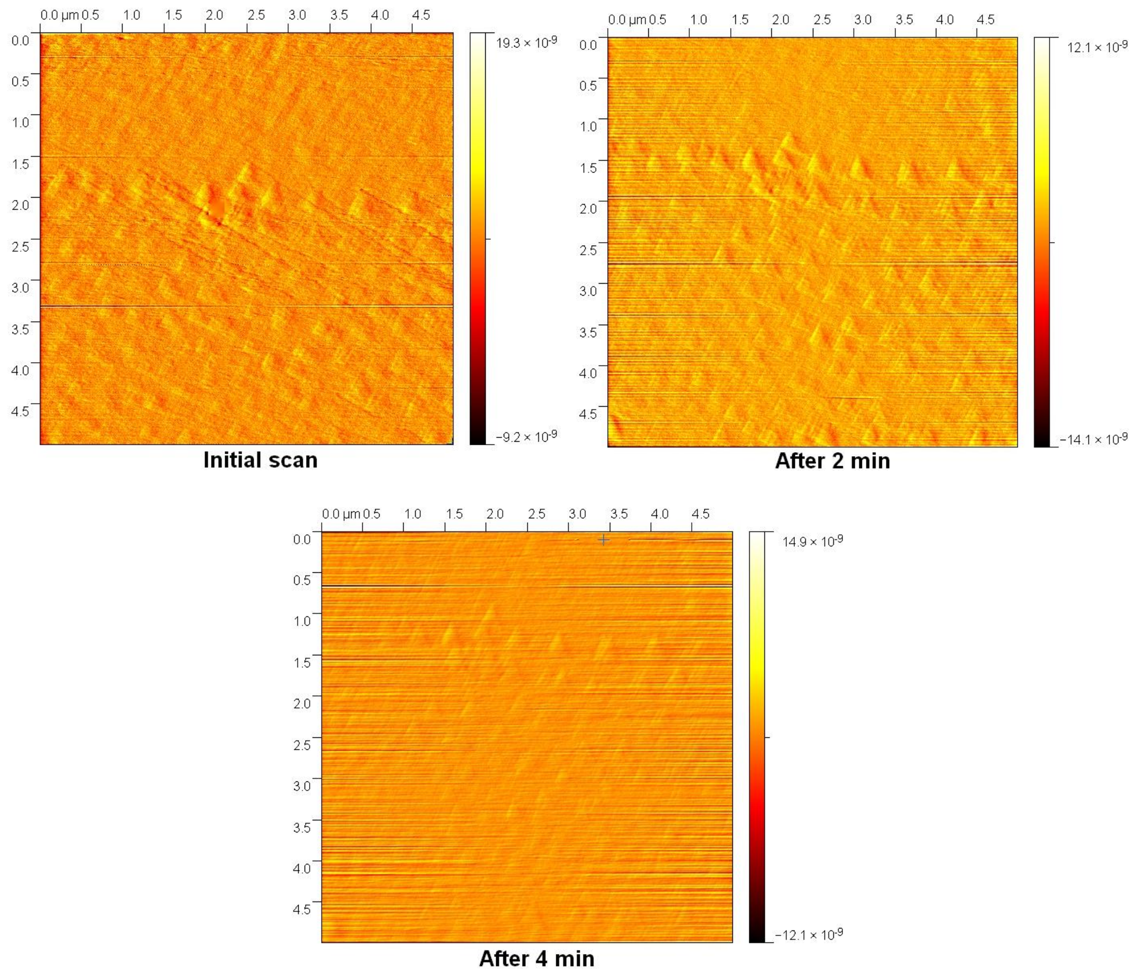

(c) (111).

Figure 5.13. Continued.

In order to quantify the surface variation, the roughness was calculated using the image processing software for each image. The roughness is the average deviation of all points from the mean line in the image (Eq. 5.13).

$$R_a = \frac{1}{N}\sum_{i=1}^{N} | r_i | \qquad [5.13]$$

where R_a is the surface roughness; r_i is the deviation from the mean line. It can be seen that the roughness reflects the distance between the peaks and valleys on a surface. The bigger the difference between the peaks and valleys, the higher the roughness. To avoid the margin effect in the imaging process, a 4×4 μm area cut from the center of the original images was used to calculate the surface roughness. Fig. 5.14 shows the results of the surface roughness of different samples. The surface roughness of the (110) and (111) samples increased with the increase of the oxidation time, while that of the (100) decreased. We focus on the change of the surface roughness rather than the absolute values, because the roughness of the initial surface was affected by the surface polishing process. The initial surface roughness of these three samples were different.

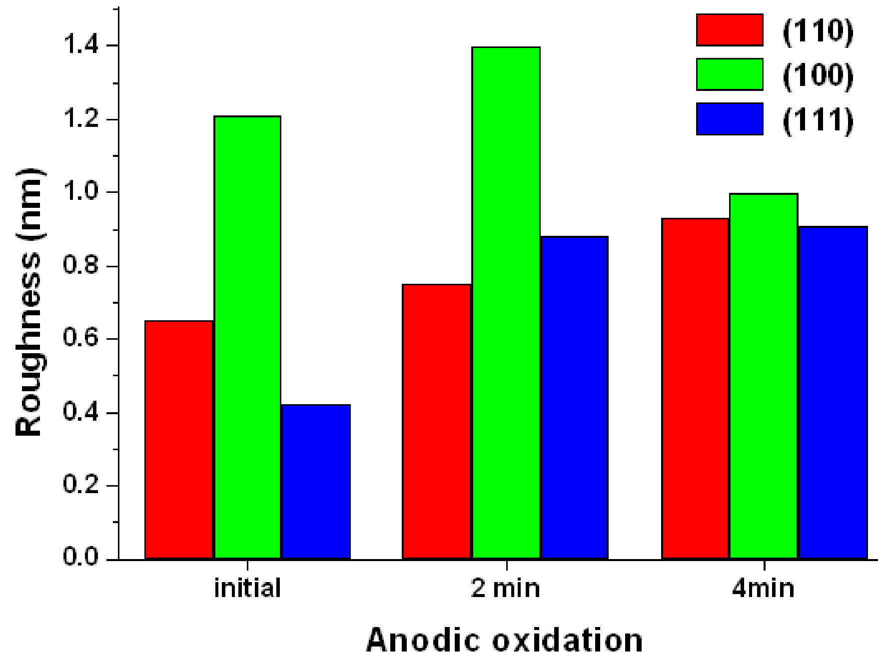

Figure 5. 14. The surface roughness of different oriented samples obtained in the dynamic experiments.

The roughness value reflects the distance between the peaks and valleys. The increase of the former indicates the increase of the latter. The roughness inclined on both (110) and (111) samples. That implies that the oxide growth of the peaks was faster than that of the valleys. This is probably due to the sharp triangle features on the surface. It is known that the electrons are readily to accumulate on a sharp tip rather than a flat surface. This may be comparable to the anodic oxidation process. In the anodic process, the electrons prefer to leave the sharp peaks rather than the relatively flat surroundings. Consequently, the oxide growth rate of the peaks is higher than that of the valleys. When the whole surface has been oxidized to the become pentoxide, the surface roughness will not change any longer. The situation on the (100) sample is different from the other two. In Fig. 5.13(b), the features are different sized islands whose top surfaces are flat. With the increase of the anodic oxidation time, the islands expanded and will finally cover the whole surface, making the surface smoother. It is clear that the surface oxidation of Ta is a function of the orientations. To this stage, the oxidation mechanism is still unknown.

In the kinetic experiments, the moving speed of the probe is much higher than that in the dynamic ones due to the larger scan area and higher scan frequency. The material removal is a function of the polishing speed. The movement of the probe in the kinetic experiments may remove oxides from the sample surface during the scan. In this experimental group, the probe scanned the same area on the sample surface for 6 times ceaselessly when an anodic potential was applied on the sample. According to the size of the scan area, frequency, and resolution, scanning one image took about 4.27 min (256 s). Since the probe moves back and forth to finish one line in an image, each point in this

scan area was totally swept for 12 (2×6) times. The anodic current was recorded during the oxidation process. Fig. 5.15 shows the current vs. time of the (111) oriented sample. Because the current was constant after 400 s, only the data points in the first 400 s are shown here. It can be seen that the current dropped dramatically in the first 50 s. After 200 s, the current became constant. As discussed in section 5.2, when the oxide layer is thick enough, the pentoxide forms on the surface preferably. In the present situation, the surface material was oxidized to the pentoxide after 200 s. The surface topography will not change if there is no perturbation. When the first imaging was completed, the surface had only the pentoxide.

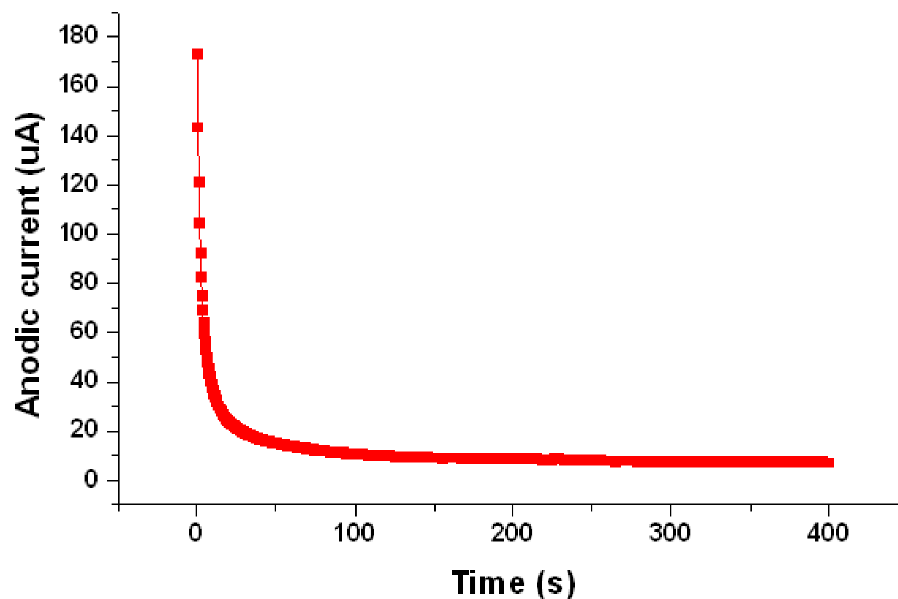

Figure 5. 15. The anodic current vs. time of the (111) oriented sample. Only the data points in the first 400 s are shown.

In order to investigate the mechanical abrasion due to the moving probe, the surface roughness analysis was conducted. The original scan area was 15×15 μm. The analyzed area at the center of the original one was 10×10 μm to avoid the margin effect. Fig. 5.16 shows the surface roughness change of the samples with different orientations during the anodic oxidation. The roughness of the (110) sample increased gradually with the oxidation time. A dramatic deterioration of the surface roughness on the (100) sample can be seen here. Dissimilar to the other two samples, the surface roughness of the (111) sample increased first, followed by a decrease. In the dynamic experiments, the roughness of the (111) surface increased with the increase of the oxidation time, while it decreased in the kinetic experiments. The opposite situation occurred on the (100) sample. That means that the mechanical abrasion induced by the moving probe did affect the surface topography during the anodic oxidation process.

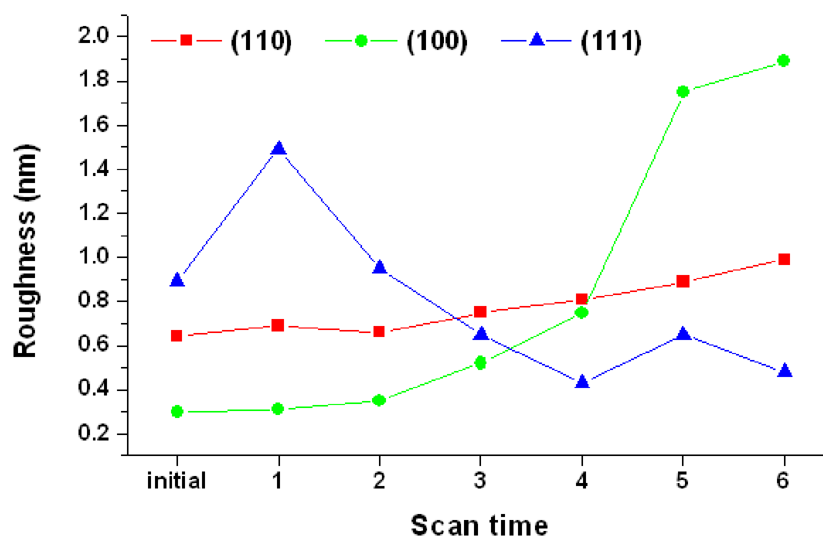

Figure 5. 16. The surface roughness change of the samples with different orientations during the anodic oxidation.

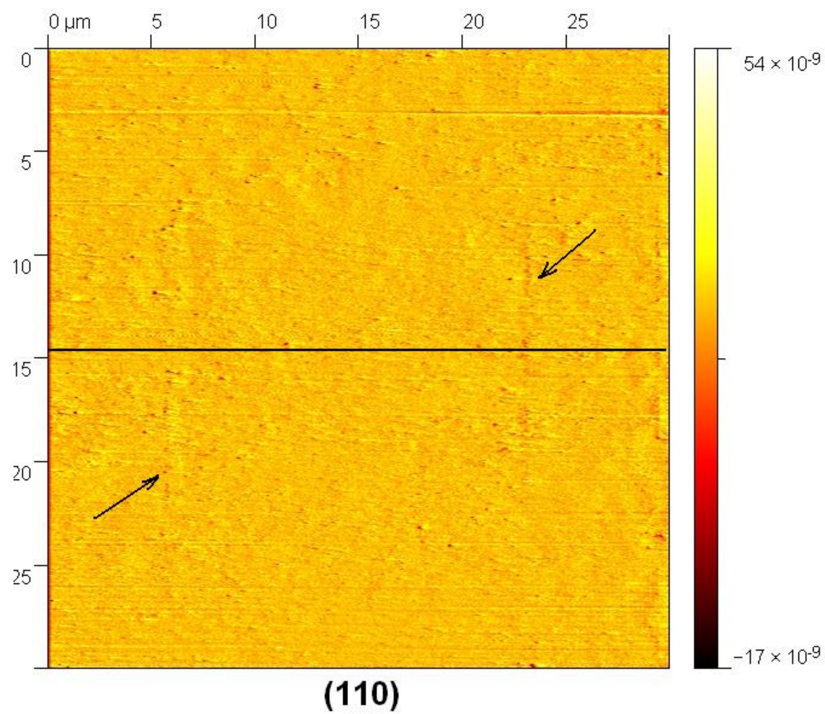

(a) The AFM image after the oxidation-scanning process. The arrows show the scan area during the oxidation.

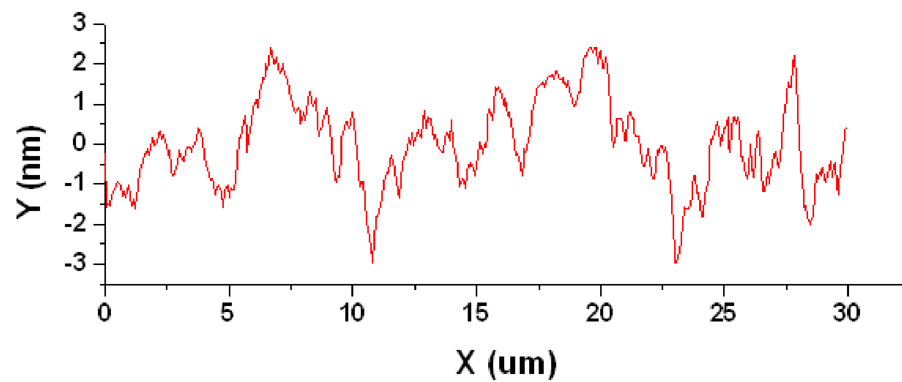

(b) The profile of the line in (a).

Figure 5. 17. The AFM scan on the (110) sample after the oxidation.

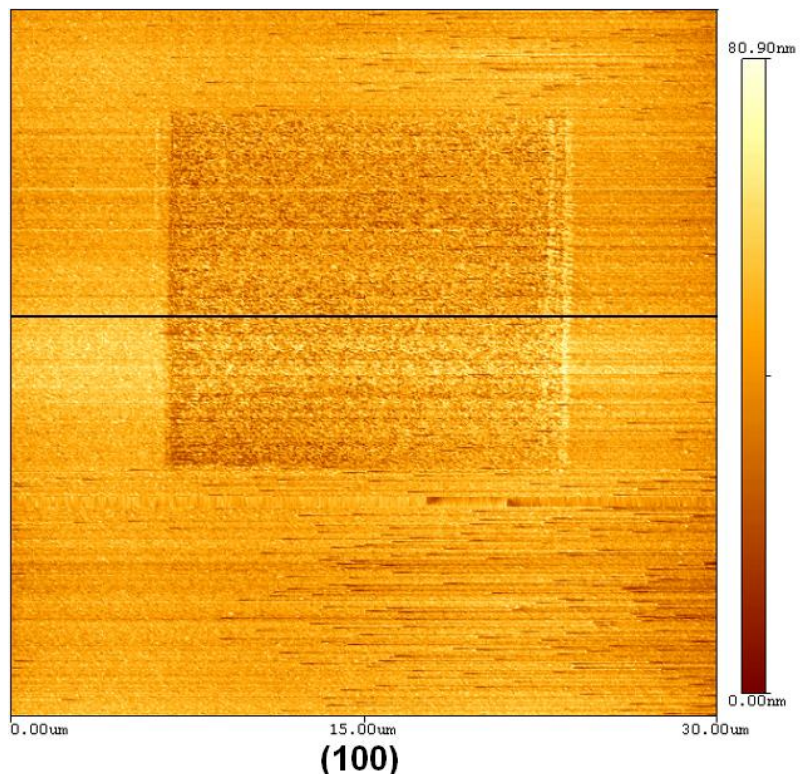

(a) The AFM image after the oxidation-scanning process.

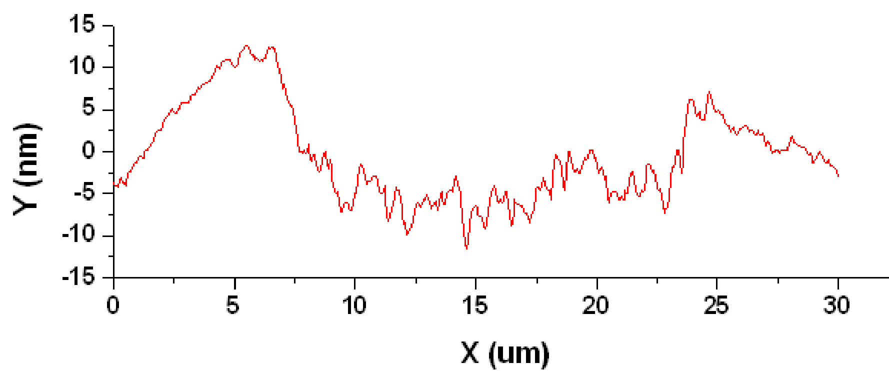

(b) The profile of the line in (a).

Figure 5. 18. The AFM scan on the (100) sample after the oxidation.

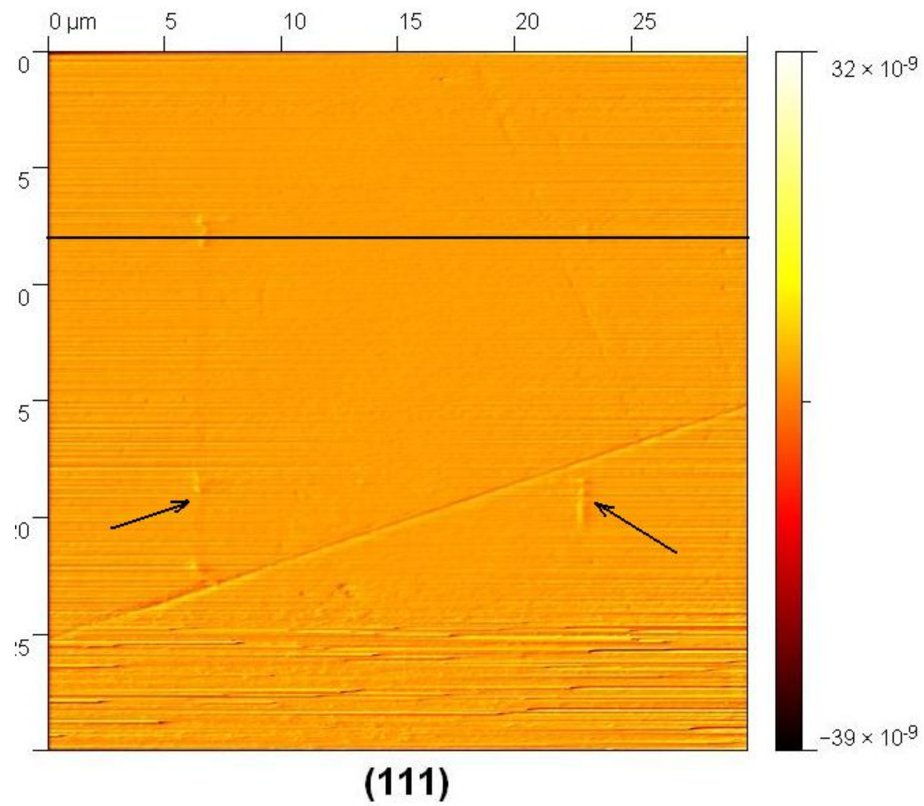

(a) The AFM image after the oxidation-scanning process. The arrows show the scan area during the oxidation.

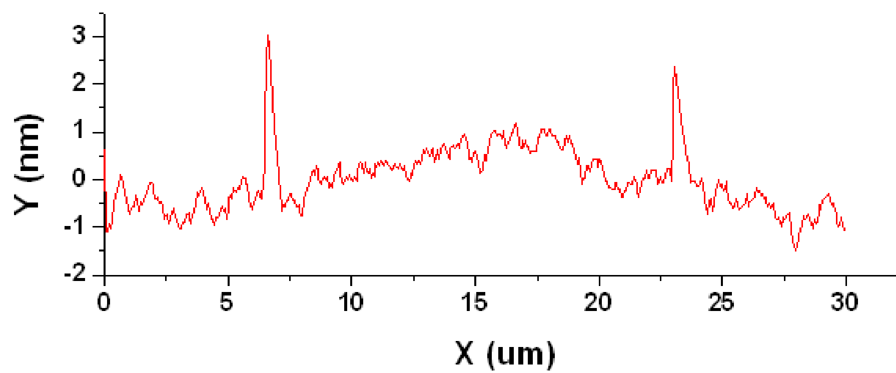

(b) The profile of the line in (a).

Figure 5. 19. The AFM scan on the (111) sample after the oxidation.

To visualize the effect of mechanical abrasion, a larger scan area was used after oxidation. Figs. 5.17, 5.18, and 5.19 show the images with the scan size of 30×30 μm which were obtained after the oxidation-scanning process on the (110), (100), and (111) samples respectively. The previous scans are included in the larger images. The profile of the black line in each image was drawn. In Fig. 5.18, a square representing the scan-induced oxidation process can be seen clearly. In Figs. 5.17 and 5.18, the squares which are labeled using arrows are not such pronounced.

Fig. 5.17(b) illustrates the profile across the scan scar and its surrounding on the (110) surface. The discrepancy between the scan scar and the surrounds is not apparent, implying that no obvious material removal occurred. However, in both dynamic and kinetic experiments, the surface roughness increased in both scanning areas. This indicates the oxidation dominance on the (110) sample. In Fig. 5.18(b) (100), the profile in the scan scar is lower and rougher than that of its surrounding. In the dynamic experiments, the roughness of the (100) surface decreased in the oxidation process. It is apparent that the substantial material removal took place in the oxidation-scanning process. This shows the domination of the mechanical abrasion. The profile of the black line in Fig. 5.19, which was obtained on the (111) surface, is illustrated in Fig. 5.19(b). It seems that the part in the scan scar is smoother than that out of it, which also can be seen in Fig. 5.19(a). The decrease of the surface roughness tells that the scanned area was smoothened by the sweeping silicon probe. There are some bumps at the left and right edges of the scan scar. They were probably due to the accumulation of the material which was swept from the scanning area to the edges by the probe. From those AFM

images and the profile analyses, it can be concluded that the role of the mechanical abrasion induced by the AFM probe is different based on different orientations. Models shown in Fig. 5.20 were established to interpret these phenomena.

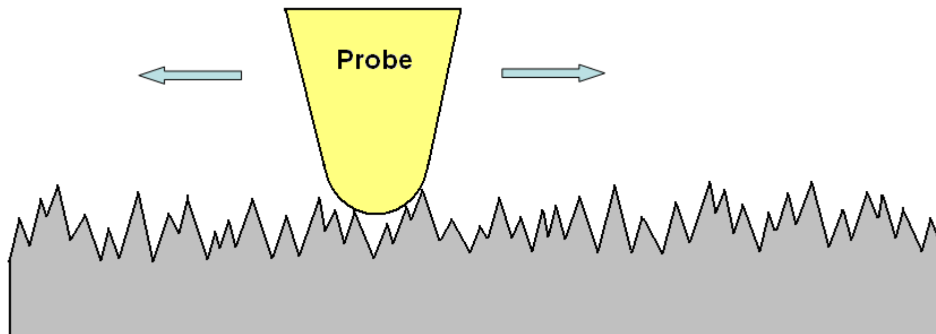

(a) (110) oriented surface. The oxidation dominates the surface variation.

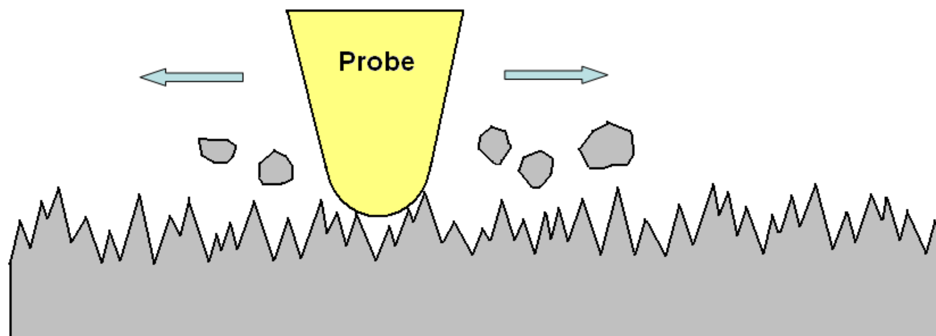

(b) (100). The mechanical removal is dominant.

Figure 5. 20. The models of the material removal in nanometer scale.

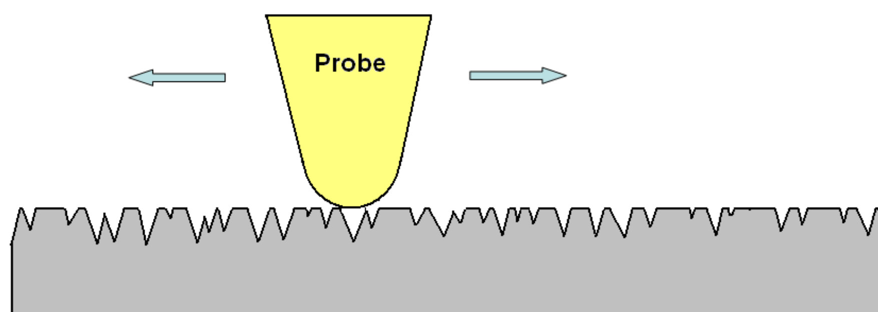

(c) (111). The mechanical removal dominates.

Figure 5.20. Continued.

As discussed in the last section, the oxidation process of the single crystalline Ta was affected by the orientations. It is possible that the oxides formed on different crystal surfaces possess different mechanical properties. For example, in Fig. 5.12, more oxygen accumulates between atomic planes in the (110) oriented sample due to its larger monolayer height, while more oxygen stays in atomic planes in the (111) oriented sample due to its lower planar density. The material removal is influenced by the properties of the surface material. On the (110) surface (Fig. 5.20(a)), the moving probe cannot remove the surface oxide mechanically. The surface variation is dominated by the oxidation process. On the (100) surface, the oxide layer may be the softest among these three samples. The oxide clusters were removal by the probe mechanically, resulting in a substantial material removal (Fig. 5.18(b)) with a rougher surface. The properties of the oxide layer on the (111) surface may be different from those of the other two samples. Only the peaks can be removal by the probe, leading to a smoother surface (Fig. 5.20(c)). The removed debris was pushed to the edges, forming bumps. In order to understand the

material removal in the nanometer scale, it is necessary to investigate the mechanical properties of the oxides formed on different oriented surfaces.

5.5. Summary

In this chapter, a modified Preston equation suitable for Ta ECMP was established. The oxidation process of the polycrystalline and single crystalline Ta during ECMP was investigated. Using the specially designed environmental cell assembled on the AFM (section 3.3.2) probe, the oxidation and material removal of the single crystalline Ta were investigated.

In section 5.1, the AFM was used to measure the material removal rate of Ta in ECMP by comparing the geometries of the micro indents before and after polishing. At a constant potential, the material removal rate (MRR) was proportional to the PV numbers which represent the mechanical abrasion. At a constant PV, the material removal rate was a second order polynomial function of the applied potential, followed by a logarithmic function. The modified Preston equation was established. The MRR was a function of the PV and applied potential. More work is needed to confirm the constants in the Preston equation.

In section 5.2, the oxidation process of the polycrystalline Ta during ECMP was studied comparing the actual removal rate measured by using AFM and the calculated one through the Faraday's law. The discrepancy of the measured removal rate and the calculated one demonstrated that the Faraday's law could be used to predict the removal rate due to the multi valences of Ta. Suboxides existed in the oxide film formed during

Ta ECMP. The new concept named average valence was used to identify the oxides in the film. It was found that more suboxides existed close to the metallic-oxide interface, while more pentoxide appeared near the surface of the oxide layer. At a constant potential, the average valence was inversely proportional to the PV number. At a constant PV, lower average valences occurred at both low and high potentials, while higher ones were found at the mediate potentials. In the former case, the oxygen diffusion into the oxide layer was dominated by the potentials. In the latter scenario, the thickness of the oxide layer was dominant. The oxidation process of TA during ECMP was a function of the potential, the thickness of the oxide layer, and the mechanical abrasion. Additionally, it was found that the suboxides were easier to be removed that the pentoxide probably because of the lower binding energy of the former.

In section 5.3, the oxidation process of the single crystalline Ta during ECMP was investigated using the same approach in section 5.2. The highest material removal rate was obtained on the (110) Ta sample, while the lowest on the (111). The (100) sample had a higher average valence than the other two samples. The surface orientation did influence the oxidation process which was a function of the packing fraction and monolayer height. The oxidation was dominated by the monolayer height on the (110) sample, while the packing fraction was dominant on the (111) sample.

In section 5.4, the environmental cell and AFM were used to study the material removal mechanisms in the nanometer length scale on the single crystalline Ta. The AFM probe was considered as an abrasive particle to rub the Ta surface. Without the perturbation of the probe, the surface roughness of the (110) and (111) samples

increased during an anodic oxidation process, while it increased on the (100) sample. In the kinetic experiments, the AFM probe swept the surfaces with different orientations ceaselessly when an anodic potential was applied. The surface roughness of the (110) and (100) samples deteriorated continuously, while that of the (111) decreased. The AFM images showed that a substantial material removal occurred on the (100) sample surface. The surface variation of the (110) sample was dominated by the oxidation process, while that of the other two was dominated by the mechanical abrasion induced by the AFM probe. These phenomena may be due to the dissimilarity of the mechanical properties of the oxide layers formed on different oriented Ta samples.

CHAPTER VI

CONCLUSIONS AND FUTURE WORK

6.1. Conclusions

This research studied the tribological and electrochemical behaviors in Ta ECMP. In situ observation of tribology and electrochemistry was enabled using unique experimental setups. New measurement techniques and analytical approaches were developed to reveal the material removal mechanisms and oxidation process in Ta ECMP. The following highlights the major findings and impacts.

We developed an in situ tribo-electrochemical setup to investigate the frictional behaviors and electrochemical reactions in Ta ECMP simultaneously. It was found that the properties of the oxide layer formed through the electrochemical reactions are affected by the mechanical forces. During ECMP, the friction coefficient is a function of five factors, cathodic reactions, mechanical abrasion, oxidation, anodic reactions, and the surface charge of sample and particles. These five competing factors dominate alternatively under different polishing conditions and electrical potentials. The approach can be used in other ECMP processes, such as copper, to investigate the tribology and electrochemistry simultaneously.

A new application of the single frequency EIS enables the in situ observation on the oxide layer change during Ta ECMP through measuring the impedance of the sample. This technique was used to study the material removal mechanisms. It was found that there are two competing mechanisms in ECMP, the formation and removal of Ta oxide. The growing and removing the oxide film are a function of the mechanical power

induced by the friction. The single frequency EIS is a new technique in the research of CMP and ECMP. Besides Ta ECMP, it can be used to study other CMP and ECMP processes, such as copper and tungsten.

The AFM was used to measure the material removal rate during Ta ECMP. The Preston equation for Ta ECMP was established. Unlike copper ECMP, the material removal rate is proportional to the PV number which represents the mechanical forces, while it is not linear to the applied potential. This result points out that the mechanical abrasion is important in Ta ECMP.

A new method was developed to reveal the oxidation state of Ta and its oxidation process through comparing the material removal rate measured by using AFM and the calculated one through the Faraday's law. The Faraday's law cannot be used to predict the material removal rate in Ta ECMP due to the multi valences of Ta. This approach revealed the distribution of the Ta suboxides and pentoxide in the oxide layer qualitatively. For the polycrystalline Ta, the oxidation process is a function of the applied anodic potential, the thickness of the oxide film, and the mechanical forces. For the single crystalline Ta, besides the previous factors, the surface orientations also impact the oxidation process greatly. This technique can be used to investigate the oxidation process of other metals.

A specially designed environmental cell assembled on the AFM was used to study the oxidation and material removal in nanometer scale. The surface change due to the anodic reactions is strongly dependent of the orientations. The AFM probe can be considered as an abrasive particle to rub the sample surface. The probe did remove the

material from the sample surface during the continuous anodic oxidation. The material removal in the nanometer scale is a function of the surface orientations. This may be due to the mechanical properties of the oxides on different oriented surfaces. This approach enables the in situ observation on the surface variation during the oxidation for other metals.

This research has important impacts not only on Ta ECMP, but also on the methodology. The results and discussion will benefit the understanding and optimization of Ta ECMP. The new experimental setups, new measurement techniques, and new analytical approaches used in this research can be applied in other metals.

6.2. Future Work

More experiments are needed to confirm the constants in the current Preston equation for Ta ECMP. In order to further understand the material removal mechanisms in the nanometer scale, the mechanical properties of the oxide layers formed on different oriented surfaces need to be investigated.

REFERENCES

1. P.L. Pai and C.H. Ting, *Electron Devic. Lett., IEEE*, **10**, 423-425 (1989).
2. J.S. Pan, A.T.S. Wee, C.H.A. Huan and J.W. Chai, *in Proceedings of SPIE - The International Society for Optical Engineering*, 4227, p. 133-137, SPIE, Singapore (2000).
3. S.P. Murarka, *Mater. Sci. Eng. R: Reports*, **R19**, 87-151 (1997).
4. M.A. Nicolet, *Thin Solid Films*, **52**, 415-443 (1978).
5. S.Y. Jang, S.M. Lee and H.K. Baik, *J. Mater. Sci.-Mater. El.*, **7**, 271-278 (1996).
6. K. Holloway, P.M. Fryer, C. Cabral, Jr., J.M.E. Harper, P.J. Bailey and K.H. Kelleher, *J. Appl. Phys.*, **71**, 5433-5444 (1992).
7. T.B. Massalski, *Binary Alloy Phase Diagrams*, ASM International, Materials Park, OH (1990).
8. M. Stavrev, C. Wenzel, A. Moller and K. Drescher, *Appl. Surf. Sci.*, **91**, 257-262 (1995).
9. H. Ono, T. Nakano and T. Ohta, *Appl. Phys. Lett.*, **64**, 1511-1513 (1994).
10. G.E. Moore, *P. IEEE*, **86**, 83-85 (1998).
11. Semiconductor Industry Association, *The International Technology Roadmap for Semiconductors*, Semiconductor Industry Association, San Jose, CA (1999).
12. J.F. Luo and D.A. Dornfeld, *Integrated Modeling of Chemical Mechanical Planarization for Sub-Micron IC Fabrication*, Springer, New York, NY (2004).

13. F.B. Kaufman, D.B. Thompson, R.E. Broadie, M.A. Jaso, W.L. Guthrie, D.J. Pearson and M.B. Small, *J. Electrochem. Soc.*, **138**, 3460-3465 (1991).

14. L.M. Cook, *J. Non-Cryst. Solids*, **120**, 152-171 (1990).

15. J. Larsen-Basse and H. Liang, *in International Conference on Erosive and Abrasive Wear (ICEAW), incorporating the 9th International Conference on Erosion by Liquid and Solid Impact (ELSIX),* 233-235, p. 647-654, Wear, Cambridge, UK (1999).

16. J.M. Steigerwald, S.P. Murarka, R.J. Gutmann and D.J. Duquette, *Mater. Chem. Phys.*, **41**, 217-228 (1995).

17. D.J. Stein, D.L. Hetherington and J.L. Cecchi, *J. Electrochem. Soc.*, **146**, 1934-1938 (1999).

18. M. Bielmann, U. Mahajan and R.K. Singh, *Electrochem. Solid. St.*, **2**, 401-403 (1999).

19. L. Chang, *J. Tribol.*, **129**, 436-437 (2007).

20. J. Luo and D.A. Dornfeld, *IEEE Transtraction Semiconduct. Manufacturing*, **16**, 45-56 (2003).

21. D.R. Evans and M.R. Oliver, *in Materials Research Society Symposium Proceedings*, *Chemical-Mechanical Planarization - Integration, Technology and Reliability*, 867, p. 189-196, Materials Research Society, San Francisco (2005).

22. Z. Li, K. Ina, P. Lefevre, I. Koshiyama and A. Philipossian, *J. Electrochem. Soc.*, **152**, G299-G304 (2005).

23. A.K. Sikder and A. Kumar, *J. Electron. Mater.*, **31**, 1016-1021 (2002).

24. H. Liang, J.-M. Martin and R. Lee, *J. Electron. Mater.*, **30**, 391-395 (2001).

25. H. Liang, T.L. Mogne and J.-M. Martin, *J. Electron. Mater.*, **31**, 872-878 (2002).

26. H. Liang, F. Kaufman, R. Sevilla and S. Anjur, *Wear*, **211**, 271279 (1997).

27. H. Liang and G.H. Xu, *Scripta Mater.*, **46**, 343-347 (2002).

28. A. Philipossian, M. Sugiyama, D. King, L. Charns, J. Degraffenreid and H. Nguyen-Ngoc, *in Proceedings - Electrochemical Society*, *Chemical Mechanical Planarization VI - Proceddings of the International Symposium*, 21, p. 261-269, Electrochemical Society Inc, Orlando, FL (2003).

29. H. Liang, *Tribol. Int.*, **38**, 235-242 (2005).

30. F.W. Preston, *J. Soc. Glass Tech.*, **11**, 214-256 (1927).

31. Q. Luo, S. Ramarajan and S.V. Babu, *Thin Solid Films*, **335**, 160-167 (1998).

32. P. Wrschka, J. Hernandez, Y. Hsu, T.S. Kuan, G.S. Oehrlein, H.J. Sun, D.A. Hanseu, J. King and M.A. Fury, *J. Electrochem. Soc.*, **146**, 2689-2696 (1999).

33. D. Castillo-Mejia and S. Beaudoin, *J. Electrochem. Soc.*, **150**, G96-G102 (2003).

34. C. Zhou, L. Shan, J.R. Hight, S. Danyluk, S.H. Ng and A.J. Paszkowski, *Tribol. Transaction*, **45**, 232-238 (2002).

35. L. Economikos, X. Wang, X. Sakamoto, P. Ong, M. Naujok, R. Knarr, L. Chen, Y. Moon, S. Neo, J. Salfelder, A. Duboust, A. Manens, W. Lu, S. Shrauti, F. Liu, S. Tsai and W. Swart, *in Proceedings of the IEEE 2004 International Interconnect Technology Conference*, p. 233-235, IEEE, Piscataway, NJ (2004).

36. M. Armacost and J.T.C. Lee, *Solid State Technol.*, **48**, 28-32 (2005).

37. N. Chandrasekaran, S. Ramarajan, W. Lee, G.M. Sabde and S. Meikle, *J. Electrochem. Soc.*, **151**, G882-G889 (2004).

38. F. Liu and M.P.F. Sutcliffe, *Tribol. Lett.*, **25**, 225-236 (2007).

39. P. Singer, *Semiconduct. Int.*, **27**, 38-42 (2004).

40. W. Ruan, L. Chen, Z. Li and T. Ye, *J. Semiconduct.*, **30**, 046001046005 (2009).

41. M. Fayolle and F. Romagna, *Microelectron. Eng.*, **37-38**, 135-141 (1997).

42. S. Mudhivarthi, N. Gitis, S. Kuiry, M. Vinogradov and A. Kumar, *J. Electrochem. Soc.*, **153**, G372-G378 (2006).

43. V. Nguyen, H. Vankranenburg and P. Woerlee, *Microelectron. Eng.*, **50**, 403-410 (2000).

44. N. Elbel, B. Neureither, B. Ebersberger and P. Lahnor, *J. Electrochem. Soc.*, **145**, 1659-1664 (1998).

45. K. Smekalin, *in Proceedings of the 4th International Conference on Semiconductor Technology*, PV 2005-12, p. 666-670, Electrochemical Society Inc, Shanghai, China (2005).

46. F.Q. Liu, L. Chen, A. Duboust, S. Tsai, A. Manens, Y. Wang and W.-Y. Hsu, *in Materials Research Society Symposium Proceedings*, *Chemical-Mechanical Planarization - Integration, Technology and Reliability*, 867, p. 87-96, Materials Research Society, San Francisco (2005).

47. F.Q. Liu, T. Du, A. Duboust, S. Tsai and W.-Y. Hsu, *J. Electrochem. Soc.*, **153**, C377-C381 (2006).

48. R. Jia, Y. Wang, Z. Wang, S. Tsai, J. Diao, D. Mao, L. Karuppiah and L. Chen, *in Copper Interconnects, New Contact and Barriers Metallurgies/Structures, and Low-k Interlevel Dielectrics III*, 1, p. 125-133, Electrochemical Society Inc, Santa Clara (2006).

49. P.C. Goonetilleke, S.V. Babu and D. Roy, *Electrochem. Solid St.*, **8**, G190-G193 (2005).

50. Y. Hong, D. Roy and S.V. Babu, *Electrochem. Solid St.*, **8**, 297-300 (2005).

51. Y.J. Oh, G.S. Park and C.H. Chung, *J. Electrochem. Soc.*, **153**, 617-621 (2006).

52. P.C. Goonetilleke and D. Roy, *Mater. Lett.*, **61**, 380-383 (2007).

53. M. Kulkarni, D. Greisen, D. Ng and H. Liang, *J. ASTM Int.*, **3**, 24-31 (2006).

54. M. Kulkarni, N. Dedy, M. Baker, L. Hong and R. Her, *Wear*, **263**, 1470-1476 (2007).

55. D. Ng, T. Sen, F. Gao and H. Liang, *J. Electrochem. Soc.*, **155**, H520-H524 (2008).

56. A. Robin, *J. Appl. Electrochem.*, **33**, 37-42 (2003).

57. I. Badawy and W. El-Gammal, *in ESARDA 15th Annual Symposium on Safeguards and Nuclear Material Management*, p. 691-694, IEEE, Ispra, Italy (1995).

58. M. Hariharaputhiran, Y. Li, S. Ramarajan and S.V. Babu, *Electrochem. Solid St.*, **3**, 95-98 (2000).

59. Z. Jian, S. Li and P.W. Carter, *J. Electrochem. Soc.*, **154**, 109-114 (2007).

60. J.P. Zheng, B.K. Klug and D. Roy, *J. Electrochem. Soc.*, **155**, 341-350 (2008).

61. D. Roy and C.M. Pettit, *Mater. Lett.*, **59**, 3885-3889 (2005).

62. A. Muthukumaran, N. Venkataraman and S. Raghavan, *J. Electrochem. Soc.*, **155**, 184-187 (2008).

63. R.M.A. Bombin and W.E.J. Neal, *Thin Solid Films*, **42**, 91-96 (1977).

64. D.A. Vermilyea, *Acta Metall.*, **6**, 166-171 (1958).

65. M.G. Cowgill and J. Stringer, *J. Less-Common Met.*, **2**, 233-240 (1960).

66. P. Kofstad, *J. Institute Met.*, **91**, 209-216 (1963).

67. P. Kofstad, *J. Less-Common Met.*, **5**, 158-170 (1963).

68. K.R. Lawless, *Rep. Prog. Phys.*, **37**, 231-316 (1974).

69. K. Wang, Z. Liu, T.H. Cruz, M. Salmeron and H. Liang, *J. Phys. Chem. A*, **114**, 2489-2497 (2010).

70. J. Stringer, *J. Less-Common Met.*, **12**, 301-317 (1967).

71. R.E. Pawel, J.V. Cathcart and J.J. Campbell, *Acta Metall.*, **10**, 149-160 (1962).

72. L. Young, *Anodic Oxide Film*, Acadimic Press, New York (1961).

73. D.A. Vermilyea, *Acta Metall.*, **1**, 282-291, 293-294 (1953).

74. D.A. Vermilyea, *J. Electrochem. Soc.*, **102**, 655-659 (1955).

75. W.D. Cornish and L. Young, *P. Roy. Soc. London A Mat.*, **335**, 39-50 (1973).

76. P. Kar, K. Wang and H. Liang, *Electrochimica Acta*, **53**, 5084-5091 (2008).

77. F. Gao, P. Kar, K. Wang, H. Liang, K. Wang, P. Kar and F. Gao, *in Proceedings of the STLE/ASME International Joint Tribology Conference*, p. 727-729, ASME, Miami (2008).

78. P. Kar, K. W and H. Liang, *Electrochem. Solid St.*, **11**, C13-C17 (2008).

79. G.W. Walter, *Corros. Sci.*, **30**, 617-629 (1990).

80. A. Foyet, T.H. Wu, L. van der Ven, A. Kodentsov, G. de With and R. van Benthem, *Prog. Org. Coat.*, **64**, 138-141 (2009).

81. O. Kerrec, D. Devilliers, H. Groult and M. Chemla, *Electrochim. Acta*, **40**, 719-724 (1995).

82. J.E.B. Randles, *Discuss. Faraday Soc.*, **1**, 11-50 (1947).

83. Gamry Instrument, Inc, *Electrochemical Measurement Systems: Getting Started Guide/Primers*, Gamry Instrument, Inc, Warminster, PA (2005).

84. D.G. Thakurta, C.L. Borst, D.W. Schwendeman, R.J. Gutmann and W.N. Gill, *Thin Solid Films*, **366**, 181-190 (2000).

85. S.C. Kuiry, S. Seal, W. Fei, J. Ramsdell, V.H. Desai, Y. Li, S.V. Babu and B. Wood, *J. Electrochem. Soc.*, **150**, C36-C43 (2003).

86. W. Choi, S.-M. Lee, J. Abiade and R.K. Singh, *J. Electrochem. Soc.*, **151**, G368-G372 (2004).

87. M. Kosmulski, P. Dahlsten, P. Prochniak and J.B. Rosenholm, *Colloid. Surface. A*, **301**, 425-431 (2007).

88. A. Bund and D. Thiemig, *J. Appl. Electrochem.*, **37**, 345-351 (2007).

89. S.N. Wosu, *J. Mater. Sci.*, **42**, 4087-4097 (2007).

90. Y.M. Li and L. Young, *Electrochim. Acta*, **44**, 605-611 (1998).

91. K. Lehovec and J. D'Amico, *J. Electrochem. Soc.*, **114**, 363-367 (1967).

92. V. Macagno and J.W. Schultze, *J. Electroanal. Chem.*, **180**, 157-170 (1984).

93. W. Choi, J. Abiade, S.-M. Lee and R.K. Singh, *J. Electrochem. Soc.y*, **151**, G512-G522 (2004).

94. F.W. Young Jr, J.V. Cathcart and A.T. Gwathmey, *Acta Metall.*, **4**, 145-152 (1956).

95. J. Yahalom and J. Zahavi, *Electrochim. Acta*, **15**, 1429-1435 (1970).

VITA

Name: Feng Gao

Address: Room 4-6, 2nd Floor, Building 3, Nanpingdongli, Capital Airport, Beijing, China 100621

Email Address: Fenggao526@gmail.com

Education: B.A., Machine Design, Tsinghua University, China, 1999

M.S., Mechanical Engineering, Tsinghua University, China, 2002